3D SIMULTANEOUS QUANTIFICATION OF SPIO AND GADOLINIUM CONTRAST AGENTS *IN VIVO* USING MR FINGERPRINTING

by

Anna Marriott

Submitted in partial fulfillment of the requirements
for the degree of Doctor of Philosophy

at

Dalhousie University
Halifax, Nova Scotia
April 2024

This work is dedicated to my children, Mar and Evie. Watching you grow has inspired me to continue to do the same. I love you both more than words can describe.

Table of Contents

List of Tables

List of Figures

Abstract

Molecular Imaging is a powerful asset to a range of disciplines, allowing for precise, noninvasive, longitudinal imaging of a myriad of biological processes. Magnetic resonance (MR) molecular imaging offers the ability to perform longitudinal studies of molecular interactions with excellent contrast, high resolution deep within tissue, without the use of radionuclides.

With the emergence of molecular imaging, the number of contrast agents targeting specific molecular or cellular processes has dramatically expanded. However, molecular imaging studies are still limited to qualitative analysis of a single agent, either requiring multiple imaging sessions, or expensive multi-modal equipment to image more than one agent. Simultaneous quantification of multiple contrast agents on a single modality would dramatically improve the research potential of molecular imaging studies.

Magnetic resonance fingerprinting (MRF) offers a novel MR imaging methodology that can generate multiple parameter maps simultaneously while allowing for greatly accelerated acquisition times. While previous studies have shown that information gathered using MRF can separate two contrast agents administered simultaneously *in vitro*, it has not yet been demonstrated that MRF can quantify the two agents most commonly used in molecular imaging studies: Gadolinium and superparamagnetic iron oxide (SPIO), the latter of which imposes the additional requirement of T_2^* mapping.

The objective of this project is to develop and apply an implementation of MRF which includes sufficient T_2^* mapping to quantify SPIO labelled cells and a Gadolinium contrast agent preclinically *in vivo*, in 3D, within an acceptable scan time of approximately 20 mins. Dual quantification of these two agents *in vivo* would allow for studies mapping complex molecular interactions, such as immunotherapy drug location and cell death maps, simultaneously.

List of Abbreviations Used

bSSFP balanced steady state free precession

C-SNAM caspace 3 sensitive nanoaggregation MRI

CT computed tomography

CTL cytotoxic T lymphocyte

EPG extended phase graphing

FID free induction decay

Gd gadolinium

GESFIDE gradient echo sampling of FID and echo

GRE gradient recalled echo

MHC-1 major histocompatibility complex 1

MION monocrystalline iron oxide nanoparticles

MPIO microparticles of iron oxide

MRF magnetic resonance fingerprinting

MRI magnetic resonance imaging

PET positron emission tomography

QRAPTEST quantification of relaxation times and proton density by twin-echo saturation-recovery turbo-field echo

RIPE regularly incremented phase encoding

SNR signal-to-noise ratio

SPECT single-photon emission computerized tomography

SPIO super paramagnetic iron oxide

SSFP steady state free precession

TESS triple echo in the steady state

USPIO ultra-small super paramagnetic iron oxide

Acknowledgements

They say it takes a village to raise a child. Whether the child in this metaphor is meant to be the thesis, or perhaps myself, I will leave to the reader's discretion.

First and foremost, I would like to thank Kim and James, whom I wholeheartedly believe to be the best co-supervisor duo the world has to offer. I remember when I first heard that my co-supervisors were married, I was slightly nervous as to how that could play out. Contrary to this worry, the support that you two have offered throughout the last 7 years has been second-to-none. Kim, you stand as a bastion against many issues prevalent in academia, and I will be forever grateful for the accepting and healthy lab environment you have cultivated. You are always working so hard (probably too hard!), but seeing you do so has inspired me to continue forward throughout this project. The lab is fortunate to have a PI dedicated to equity, and I am thankful to have a such a fantastic supervisor and friend. James, whether offering coding knowledge, advice on mindfulness during a difficult time, or some eye-rolling puns, you always know just how to help. This project would have gotten stuck several times if not for your expert help and willingness to roll up your sleeves with me, to which I am extremely thankful. I am hopeful that one day I will eventually beat you at Smash Bros, truly the highest honour, even beyond attaining a Ph.D.

I would also like to thank my committee, for their insightful guidance throughout this project. Tim, thank you for providing the opportunity to guest lecture, and your guidance toward pursuing teaching. Your passion for teaching shines through in all interactions we have had, and your rigour with regards to the scientific method has shaped this work for the better. Chris, I remember being terrified of the sheer depth of your MR knowledge when we met several years ago. Thank you for offering such fantastic insights into the anachronistic legacy code in which the reconstruction of spiral MRF is based on, as well as delivery of some of the funniest one liner's I've ever heard.

To my many science friends I have made along this journey: Matt, Brianna, Vlora, Hannah, Sarah, Mary, and Cassidy. I can't decide if we made the best decision of our

lives to pursue a doctorate during a global pandemic, or perhaps the worst decision. Nonetheless, we all now stand on the tail ends of a hard journey (except Matt, who beat me to graduating!!). I will forever cherish experiencing this with all of you, the memory of this Ph.D. made all the more special by the times spent together, whether laughing or crying.

To Lura, I owe so much of the person that I am today to the time that we have spent together. I am grateful to be connected to someone so full of brightness, warmth, and passion. I am so excited for what the next few years hold for both of us as we move forward into new and exciting things. I would never have started this Ph.D. if not for your support, and while circumstances have changed over the last 7 years, you continued that support until completion. Thank you for everything.

To Jason, thank you for the kindness that you have shown me through my ups and downs, I have always been able to rely on you for a warm meal once a day even when my work hours got so messed up that I hadn't seen the sun for weeks. Thank you for your friendship; you have shown me the meaning of found-family, and I look forward to watching Theo grow into a capable adult under your care. Theo, thank you for all the hugs and free oxytocin which you provided throughout the writing process. I could always count on you for a cute 15 minute break with lots of adorable baby sounds.

To my eldest, Maria Elizabeth Grace. It is unfortunate that both of our lives have become so busy that our time together is sparse, but that just makes the deep and meaningful conversations we have even more special. I am always moved by your unwavering authenticity. Always on hand with the funniest jokes and great TV recommendations, you have made the drab existence of thesis writing contain far more laughter. I cannot wait to see where your art and music take you.

To my baby, Evedene Avalon. It has been a great pleasure to watch you grow from an apple loving, cuddly 5 year old into a driven, focused, young lady. It is not at all average for a child to be put through the paces that you willingly subject yourself to in the name of athletic excellence, yet every day I see you moving towards your goal of being the best you can be. I can always count on you to pop your head around the door when I am writing to show off your new baked goods, or remind me that

it's time to drive you to practice.

Finally, to June. It would be remiss of me to not mention you after the impact which you have had on my life in the last couple of years. There existed a moment during this process where I wasn't sure I had the strength to continue. It becomes very easy to get lost within such a long body of work, doing the same thing for years upon years. I have had the fortune of a partner which understands this feeling all too well, someone to draw strength from in difficult times. Always there for me, whether to mercilessly proofread my scientific writing, to discuss the best layout for a figure, or just to keep me company during long nights of collecting data, I have found in you much more than just a partner, but a formidable scientific co-worker, and a best friend. I hope that I can provide the same support for you as you begin to write your Ph.D. thesis soon.

Chapter 1

Introduction

Since its inception, magnetic resonance imaging (MRI) has become an invaluable tool used broadly throughout the medical field. Its non-invasive nature, coupled with superior soft-tissue visualization and lack of ionizing radiation, positions it as a powerful technique with a wide array of applications. Despite being iterated on for over 40 years, MRI continues to find new uses as other fields of science develop. Molecular imaging is one such field, in which MRI enables longitudinal studies of molecular interactions with excellent contrast, high resolution deep within tissue, and without interfering with the biological processes of interest. Continued development of MRI is critical to further enhance applications such as cell tracking in immunology studies.

In this work, we present a set of improvements to the novel MRI sequence, magnetic resonance fingerprinting (MRF), with direct application to cellular quantification and imaging. Beginning with an introduction to molecular imaging, cell tracking, and the background theory behind MRI, we will then demonstrate that MRF is a technique which can be modified to include T_2^* sensitivity, and can be utilized to quantify two separate MR contrast agents in a single scan. We will conclude with an *in vivo* demonstration of MRF's value to immunological studies, showing quantification of two separate contrast agent labelled cellular processes imaged simultaneously.

1.1 Molecular Imaging

The human body is an immensely complex system; an intricate arrangement of cells, proteins, and a myriad of processes and molecular interactions. If one is to understand these structures and processes, the proper tools are required to gain insight. While *in vitro* studies can provide valuable information as to the mechanics of cells and proteins, *in vivo* studies provide context such as recruitment and migration patterns [1], allowing us to truly understand behaviour on a cellular level. It is therefore critical

for researchers to have access to quantitative, non-invasive methods of molecular imaging, that can be utilized repeatedly over extended periods of time [2].

Molecular imaging can be performed using several different imaging modalities, each with its strengths and weaknesses. Optical imaging methods, such as fluorescence or bioluminescence, are broadly defined as an imaging discipline which measures light released by administered agents. These techniques offer inexpensive high sensitivity and specificity [3] but are limited to small depth imaging, due to the low tissue penetration of light restricting the types of studies that can be performed without invasive surgery [4].

Computed tomography (CT) relies on x-rays attenuating through a material proportional to its atomic number, providing anatomical information. This modality has high sensitivity and resolution, strong penetration depth, and low cost; however, it involves the use of ionizing radiation and offers poor soft-tissue contrast. Molecular imaging, though infrequent, can be performed with CT via the introduction of a high atomic weight contrast agent [5], for example, the introduction of gold nanoparticles designed to bind to prostate-specific membrane antigen [6].

Positron emission tomography (PET) or single-photon emission computerized tomography (SPECT) introduces radionuclides and produces images through detection of the ionizing radiation. This methodology provides extraordinarily high sensitivity and specificity and, due to the small amount of radionuclide required, cellular imaging is achievable without altering the biological function of the cells [7]. PET and SPECT are powerful tools for molecular imaging when compared to conventional anatomical modalities [5], but provide limited resolution with no anatomical context, necessitating multimodal imaging, while also producing ionizing radiation. One example of molecular imaging with PET is the metabolization of the glucose analog 2-^{18}F-fluoro-2-deoxyglucose (^{18}F-FDG), enabling visualization of glucose-hungry physiology such as tumours.

MRI is a modality that can image at high resolution deep within tissue, offers excellent soft-tissue contrast, and allows the measurement of a myriad of physiological, biochemical, and metabolic processes without the use of ionizing radiation. While MRI does not boast the molar sensitivity of PET it is still a valuable tool for cellular imaging, as it is noninvasive, non-radioactive, and capable of imaging and tracking a

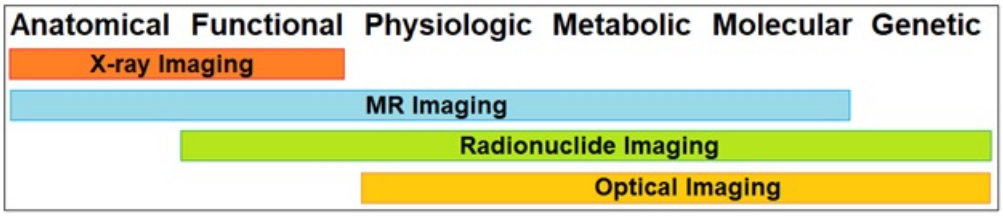

Figure 1.1: Imaging extent of commonly used modalities based on popular use [8]. Each provides a different scope of information, popularising the use of multiple modalities in molecular imaging studies.

number of cellular ranges and behaviours of interest to researchers.

The various weaknesses of these techniques may be eliminated via a combination of multiple instruments. Referred to as multimodality molecular imaging, these attempts to combine two or more of these methods have allowed for both high resolution and high sensitivity hybrid images to obtain more comprehensive accurate information, and now play a critical role in both preclinical and clinical research.

With the emergence of multimodality molecular imaging, the number of available contrast agents has dramatically increased, leading to agents able to produce a strong signal in two modalities simultaneously. One such agent is ^{64}Cu-super paramagnetic iron oxide (SPIO), which can be detected with both PET and MRI. [9], as well as a wealth of agents for singular modalities targeting many different mechanisms, such as proteins [10], cell receptors [11], and other molecular species in MRI [12].

However, multimodality imaging has its drawbacks, including specialized hardware, the introduction of radioactivity, and potentially no inherent co-registration. A technique that could provide quantitative molecular imaging for multiple agents in a single modality would improve the speed, lower complexity, and reduce the cost of future studies while providing information critical to answer the more elusive molecular questions. It would also add significant value to multimodality imaging if a single technique alone could detect multiple agents at once. With its varied methods of generating contrast and quantifying signal, MRI is a prime candidate for multiple agent quantification.

1.2 MR Imaging

MRI involves the manipulation of an object's natural magnetic properties to produce signals, providing exquisite detail about anatomy and function. When a sample is placed in a strong magnet, the ubiquitous hydrogen atoms within the sample align, creating a net magnetic vector that lines up with the field. By introducing additional energy, in the form of radio waves, this net magnetization will be perturbed. As it returns to equilibrium (relaxes), the signal is emitted, which provides information about the surrounding tissue.

The relaxation is measured in two ways: the time required to restore the equilibrium magnetization signal, and the time until the excited signal is lost. Equilibrium restoration is referred to as T_1, and decay of excited signal is known as T_2 or T_2^*. Each of these has an associated relaxation rate, which are referred to as $R_1/R_2/R_2^*$, and are the reciprocal of each respective relaxation time.

MRI is a tremendously flexible imaging modality; by altering the types, number, and order of the RF and field gradient pulses introduced to the tissue, MRI can emphasize or suppress the signal emitted, creating images that highlight anatomy or function of interest.

Unfortunately, MRI has low sensitivity compared to other techniques. This is due to signal not being produced by all targeted atoms in the body, but the population difference between spins parallel and antiparallel to the field, which is small at room temperature. Contrast agents can allow for the targeting of biological mechanisms of interest, with studies showing that contrast agent enhanced MRI can detect a single cell [13].

There are several MRI contrast agents commercially available for molecular imaging studies, all of which have their benefits and drawbacks. An ideal contrast agent would be biocompatible, be non-toxic, provide stable contrast with high sensitivity, provide a clear enhancement from the background signal, and allow for long term studies, by not diluting with cell proliferation or transferring to other cells. A contrast agent with all of these features does not currently exist [14], as a lack of cell proliferation dilution would require a self-replicating contrast agent. One potential solution is reporter gene imaging, which uses genetic manipulation to specifically combine with molecular probes containing imaging biomarkers. However, currently,

the same dilution problem occurs, as an exogenous contrast agent is still required for sufficient sensitivity. Gene reporter imaging's primary downside is the complexity of the genetic manipulation required to enable it. [15].

Of the many contrast agents available, three of the most common for molecular studies are iron oxide, gadolinium (Gd), and fluorine. Iron oxide nanoparticles are one of the most common for preclinical studies, due to being readily consumed by professional phagocytic cells with no conjugation to additional compounds, and iron oxide's relaxation effect far exceeding most other agents, boosting sensitivity. The preferred iron oxide nanoparticle for *in vivo* studies is SPIO.

1.2.1 Molecular MR Imaging

While contrast agents are responsible for producing signal *in vivo*, they must be targeted to molecular processes of interest. By attaching the signal agent to a targeting moiety, a 'smart' contrast agent can be produced, which only expresses signal at the biological mechanism of interest. This was first demonstrated in 1997, where water molecule exchange with an inner Gd^{+3} molecule was activated via cleaving by the β-galactosidase enzyme [16]. Since then, countless novel chelates have been designed which can target and track a number of different molecular processes which lack the specificity for MRI detection but are abundant enough to be targeted by MRI contrast agents. One example is the use of Gd agents to target collagen, which is highly regulated under healthy circumstances, but in the presence of disease states such as cancer and fibrosis become deregulated. Collagen-binding Gd agents have been used to detect a myriad of issues in animal models, including fibrosis of the liver [17], lung [18], and pancreatic cancer [19].

Many probes have demonstrated effective mapping of chemotherapy and radiation therapy-induced cell death. For instance, the caspace 3 sensitive nanoaggregation MRI (C-SNAM) contrast agent probes for caspases 3 and 7, executioner proteins responsible for the coordination of apoptosis events [20]. To facilitate molecular MR imaging, this probe cyclizes and self assembles into nanoparticles in the presence of these enzymes, amplifying the signal and overcoming the low sensitivity issues associated with MRI.

Similarly, other Gd probes have attempted to image the early onset of apoptosis via sensitivity to the expression of the plasma membrane phospholipid phosphatidylserine, expressed on the surface of apoptotic cells [21]. The abundance of apoptosis-targeted contrast agents is due to a lack of good prognostic indicator of treatment outcome.

Gd's effective transverse relaxation is an order of magnitude smaller than iron-based agents, requiring higher concentrations for imaging. However, studies have demonstrated successful MR Gd imaging with concentrations as low as 50 ug/mL [22]. One of the benefits of Gd is that the ligand structures to which it is bound can also be tagged with fluorescent compounds, providing additional cellular information, or verification data. Unfortunately, Gd is not biocompatible, and little is known about potential toxicity after dechelation, particularly inside cells [23]. Internalized Gd also exhibits a lower R_1 relaxivity, due to water not easily passing through the endosome membrane where the Gd resides, requiring even greater cell loading for detectability [24].

Other contrast agents such as Mn have been shown to have comparable imaging capabilities to Gd [25, 26], and SPIO molecular targeting probes have been utilized in a range of targeting probes, including cardiovascular diseases [27], and apoptosis [28].

1.2.2 Cell Labelling for MR Imaging

As well as targeting and imaging molecular processes, contrast agents can image the biodistribution of cells, via internalization or attachment to the cells of interest.

Two of the most popular contrast agents for use in cellular MRI are ^{19}F and SPIO. ^{19}F cell labelling provides background-free imaging and does not alter cell viability, division, or phenotype when cell labelling, and fluorine-rich perfluorocarbon emulsions have been specifically designed to be endocytosed by non-phagocytic cells [29]. Similarly, SPIO's dextran coating allows straightforward attachment of ligands and relevant functional groups, enabling imaging of small numbers of cells for up to several weeks, depending on the size of the contrast agent [30].

Both these contrast agents have their own drawbacks. ^{19}F is not endogenous to the body, and so produces much less signal than traditional ^{1}H imaging, while also

requiring bespoke RF coils to achieve similar NMR sensitivity. SPIO's high magnetic susceptibility can lead to MR artefacts, provides a negative contrast, and deposition has been shown to last for up to 11 months, limiting repeated studies [31]. Despite this, iron-based contrast agents are currently the best candidate for cellular imaging, as their transverse relaxivity far exceeds any other element.

In situ injections of these contrast agent are an option, but this limits the types of studies available, as they will only be easily internalized by macrophages. For non-phagocytic or slowly dividing cells, potentially toxic concentrations would be required for efficient cell labelling. As such, a cohort of different techniques providing a more delicate and precise labelling methods have been developed.

Non-specific direct labelling is the most straight forward approach, whereby the label is added to a culture dish containing the cells. The efficacy of this technique is highly dependent on cells of interest; antigen-presenting cells such as dendritic cells and phagocytic cells like macrophages have no trouble internalizing the contrast agent in this manner. However, other cell types may not perform as well [32]. In mixed cell populations, the contrast agent will be taken up by a variety of endocytic cells. The benefits of nonspecific direct labelling are in its simplicity, with no additional compounds or manipulations required, enabling even *in vivo* labelling in specific situations.

Non-specific indirect labelling seeks to improve uptake of contrast agents via the introduction of a transfection agent. This method takes more time and effort than direct cell labelling but improves the efficacy of indirect labelling for all cell types. Care must be taken to limit the toxicity of the transfection agent. Many different transfection agents exist, each with its pros and cons. Non-specific indirect labelling also includes some more novel and creative mechanisms, such as electroporation, where utilizing electric pulses to create a potential difference across cells leads to the opening of pores [33].

Specific labelling allows for the targeting of specific cells in a mixed population. This is performed using a targeting vector, which is attached to the contrast agent. The vector serves to seek out the cell of interest, binding only to the target cell. Relative to relying on the endocytic mechanisms of cells used in non-specific labelling, specific labelling increases efficiency and allows the targeting of specific cells. This

requires knowledge of not only the chemical linkages that will target the cells of interest but also the exclusion of bonds which may attach to more than just the cells of interest. Care must also be taken as targeting and attaching to a cell may change its biological behaviour. It is also beneficial for the targeting vectors to include mechanisms to improve contrast agent internalization after the attachment has occurred to decrease the risk of later detachment.

The primary drawback of all cellular labelling is the loss of the agent due to cell differentiation, transfer to macrophages engulfing dead cells, or specifically for SPIO, a hypointense signal at the injury site due to ferritin deposition caused by microbleeds. These all lead to false-positive MRI data. Most experiments are verified by performing histological studies, such as Prussian blue straining for SPIO-based studies, to correlate with MRI data and eliminate false positives [34].

The majority of labelling applications are in cellular therapies, where donor cells are introduced in an attempt to repair tissue, attack tumours, or enhance the immune response. One example is stem cell therapy studies, where undifferentiated cells allow for valuable studies into disease, drug testing, and other therapies. A popular emerging use for stem cells is for use in regenerative medicine, where complex biological injuries are treated via transplant of the appropriate type of stem cells for their healing potential. The cells must be honed to an injury site after implantation in large quantities to ensure successful treatment, making *in vivo* cell tracking of stem cells essential for the development of these therapeutic regimes. Using MRI, neural stem cells labelled with Gd have been shown to allow visualization of cell migration [35], stem cells labelled with a ferritin agent have been quantified post injection [36], and the use of both Gd and SPIO agents in the same study has allowed for a distinction between alive and dead stem cells *in vivo* [37].

Cellular imaging has also enhanced the field of cancer research. While cancer detection has traditionally been performed using imaging, the ability to image specific cells can provide valuable information on the longitudinal molecular mechanisms, as well as providing information on the effectiveness of treatment[38].

1.3 Cancer, Immunotherapies, and Cancer Imaging

1.3.1 Immunotherapies

Immunotherapies aim to manipulate the body's innate and adaptive immune system to invoke a therapeutic effect. Our immune systems are very intricate and powerful systems adapted over the course of millions of years to protect human bodies; the combined actions of both the innate system, providing rapid response, and the adaptive system, with its tremendous specificity and memory, defend us from the many invaders entering our body every day.

It has been theorized since the early 1900s that the immune system has a part to play in fighting cancer [39], and since that time much evidence has confirmed this. This includes the ability for cancer to spontaneously enter remission without treatment, tumour-specific cytotoxic T cells at the tumour site of the draining lymph node, and the increased occurrence of certain cancers in immunocompromised patients [40]. Immunotherapy is now viewed as one of the more precise cancer treatments and is considered a cornerstone for recovery, alongside surgery, chemotherapy, and radiation therapy.

However, for the immune system to mount an effective attack against cancer, many complicated and intricate parts must follow a chain reaction. The local innate system must activate dendritic cells, which process tumour-specific antigen material and migrate to the lymph nodes. The dendritic cells present the antigen, activating specific cytotoxic T cells, which travel to the tumour site. These killer T cells must seek out matching major histocompatibility complex 1 (MHC-1) presentation on the surface of cells, puncture the cancer cell and deliver their cytotoxins.

Unfortunately, disruption at any stage will result in an ineffective response with the tumour remaining intact, and tumours typically have additional mechanisms to suppress the immune response of patients, allowing evasion of an effective immune response. These include induction of regulatory T cells, which act to suppress the tumour-specific T cells [41], impairing the function of dendritic cells via inactivation [42], and MHC-1 loss, either by structural defects of presentation loss, or immunosuppressive cytokine production [43].

Immunotherapies can offer many ways to increase the likelihood of a successful

defence. These can include the mass introduction of a tumour specific antigen to a system, aiming to improve the chances of antigen-presenting cell activation [44]; or surgical removal of T cells, followed by *in vitro* activation, and reimplantation [45]. Both of these techniques can serve to bolster a specific step of the process, and consequently the strength of an immune response.

1.3.2 Cancer and Cellular Imaging

Cellular imaging has allowed exploration of the deposition of these immunotherapies, while also determining the fate and metastatic potential of tumour cells [46], further improving efficacy. This is important, as adoptive cell immunotherapies have been shown to deliver a relatively low amount (1-10%) of the antigen-presenting cells to the relevant lymph node [47], so by studying the injection sites, delivery timings, and concentrations, delivery methods designed to maximize deposition to the draining lymph node can be found.

Despite the abundance of immunotherapy research being conducted, the clinical translation of immunotherapies has not been as effective as hoped for [48]. Traditional indicators of therapeutic success such as tumour size neglect metastases, and take several weeks to react to an effective treatment [49], leading to volume measurements providing a poor prognostic indicator of treatment outcome. It is critical that better tools be developed for reliable and early assessment of treatment efficacy for immunotherapies.

Cellular imaging using MRI offers a chance to noninvasively measure the size, location, metabolism and viability of cells in tumours due to its high sensitivity, and has proven to be capable of tracking cancer cells from arrest to metastasis [50]. Cellular MRI also offers the ability to verify other cell tracking modalities; one study reported that iron-loaded cellular MRI could be used to visualize growth differences between naïve and luciferase-expressing breast cancer cells, demonstrating that the engineered cells formed tumours at a reduced rate, and highlighting the need for extra care when considering gene reporter imaging for metastatic cancer studies [51].

Cellular imaging can also facilitate the tracking of the immune cells involved in the immune response, such as regulatory T cells, or myeloid-derived suppressor cells, which are recruited by cancer cells during cancer therapies, and negate the effects

of treatment [52]. Monitoring these suppressor cells during tumour growth provides information critical to successful immunotherapy, and migration and location patterns during active therapy can provide valuable insight into optimal treatment regimes [38]. A recent study labelled CD8+ cytotoxic T cells, regulatory T cells, and myeloid-derived suppressor cells with SPIO to monitor and measure migration during delivery of an immunotherapy in tumour-bearing mice [38]. Cellular MRI demonstrated that treatment caused a decrease in the recruitment of suppressive cells and an increased cytotoxic T lymphocyte (CTL) recruitment to the inguinal lymph nodes.

Even though cellular MRI is a valuable tool for better understanding the biological mechanisms of immunologic response via tracking of individual populations of immune cells, two limitations still hinder the complexity of immunotherapy studies: the qualitative nature of cell tracking, and the restriction to the visualization of a single process per modality.

1.4 Cell Tracking and Quantification

1.4.1 MR quantification

Despite MR cellular detection being available for over 20 years, improving methods to include quantification of cells has proven challenging. While cell detection can be modified to provide semi-quantification, often this relies on assumptions that compromise the accuracy of the results.

A common method of approximating quantification is assuming that signal increase/decrease when a contrast agent is introduced is proportional to the number of cells in a given location, allowing for a technically simple implementation. This requires segmentation of the area of interest, which can be performed either manually or automatically. Each method has its benefits, with manual segmentation being more appropriate for large bulk regions containing contrast agents, and automatic segmentation providing more accurate data for more labour-intensive small clusters of contrast agents which may not be immediately obvious during manual segmentation. A mixture of the two methods can often provide the best results [53].

As one of the most popular cellular contrast agents, many studies have investigated the signal-based techniques for SPIO labelled cells. Semi-quantification of SPIO

labelled dendritic cells has been demonstrated by measuring the mean signal void volume and mean fractional loss [54], but more recent studies have shown that dendritic cells migration paths to target lymph nodes may be affected by SPIO loading.

The choices of sequence for this are wide, as most gradient recalled echo (GRE) sequences offer sensitivity to T_2^* due to the lack of a 180° radiofrequency pulse, and therefore no dephasing compensation for magnetic field inhomogeneity. GRE sequences exist in two rough categories: incoherent, where magnetization is spoiled after acquiring the signal, and coherent, where the signal is instead allowed to persist into the next excitation, leading to a steady-state buildup [55]. Most sequences used for T_2^* weighted images are either incoherent GRE or modifications of GRE, where sequence parameters are tailored to provide T_2^* contrast.

Similarly, with Gd, semi-quantification can be performed by measuring the difference of signal in areas with and without Gd. Signal based semi-quantification has been used to investigate the effect of contrast agents on mitochondrial respiratory function and cell viability in human neurons [56], and it has been demonstrated that a gadolinium contrast agent can be quantified between $5 \times 10^3 - 1 \times 10^6$ μg/mL by using signal-based techniques [22].

Gd uptake is typically faster than that of SPIO, so it is often appropriate for the 'without Gd' signal to be an image from before the Gd was administered [57]. This is not to suggest that longitudinal studies are not possible with Gd, as it has been shown that some Gd contrast agents can be detected *in vivo* up to 10 days after injection [24].

These signal-based techniques have drawbacks; for example, there must be enough signal present to determine concentrations. Both Gd and SPIO have the potential to spoil a signal within a few milliseconds in high enough quantities, so signal based techniques are limited by the minimum TE achievable. This is particularly true of SPIO, as the negative contrast leads to low specificity.

To combat this, positive contrast methods for SPIO have been proposed, which aim to suppress the background signal, producing signal enhancement at the location of the cells of interest. These can be implemented in several ways, including exploiting the signal enhancement next to the off-resonant singularity point to map $\vec{B}_0$ offset for low angle balanced steady-state free precession (bSSFP) [58], imaging gradients for

field compensation [59], and off-resonant associated echo-shift in k-space [60]. However, these are typically even more of an indirect measurement, as these techniques are not imaging the actual regions containing SPIO. Positive contrast SPIO also doesn't provide information on anatomy like conventional GRE or spin-echo sequences do.

^{19}F semi-quantitative cellular imaging has also been used in a variety of studies, including T cell and macrophage infiltration timelines [61], dendritic cell migration patterns [62], and subcutaneous transplanting optimization [63]. While many ^{19}F studies claim to be quantitative, due to the specificity of the ^{19}F signal and the inclusion of a calibration phantom, the sensitivity of ^{19}F studies doesn't enable imaging of a smaller number of cells. To provide a more realistic range of cell numbers, a more sophisticated method is required.

1.4.2 Relaxometry

The second type of quantification technique relies on spatially resolving relaxation parameters. As the relaxation rate of a given voxel scales linearly with contrast agent concentration, this allows for more accurate mapping of contrast agents, provided that the loading rate of the cells is known. This has been demonstrated many times for both Gd [64, 65] and SPIO [66, 67].

Relaxation mapping is traditionally performed by repeated measurements with varying inversion times for T_1 or echo times for T_2. This allows for the sampling of signal decay at different time points, allowing for fitting to a parameterized model. For T_1, this relaxation is the return to longitudinal equilibrium, and for T_2 and T_2^*, this is a transverse dephasing of the spins. All of these behaviours can be fit to an exponential relationship if enough time points of the signal are collected.

Gadolinium agents primarily induce T_1 enhancement, and so the most appropriate sequences are T_1-weighted spin-echo imaging. T_1 relaxometry using inversion recovery or saturation recovery spin-echo sequences has been demonstrated to provide maps appropriate for Gd concentration quantification [64], however, it has also been shown that Gd^{+3} ions inside large molecules behave more similarly to T_2 weighted agents, where a T_2 weighted spin-echo sequence would provide a more accurate measurement [35]. Therefore, under circumstances such as Gd^{+3} cell uptake, T_1 mapping alone does not always provide a complete description of the contrast agent concentration [68], but

quantitative heatmaps of T_1 relaxation times strongly correlate to Gd concentration [69].

For SPIO mapping, either T_2 or T_2^* can be used. Most GRE sequences will be sensitive to T_2^*, as the lack of a 180° radiofrequency pulse does not provide dephasing compensation.

For measuring T_2, single echo sequences can be used, but are not as efficient as employing multiple spin-echo techniques, such as a Carr-Purcell-Meiboom-Gill (CPMG) sequence, which vastly reduce scan times. Unfortunately, rudimentary spin-echo sequences have problems associated with RF field inhomogeneities, and so are not suitable for SPIO mapping without considerable artifacts. This can be addressed by sequences like Gradient Echo Sampling of the Free Induction Decay and Spin Echo (GESFIDE), which incorporates a train of gradient echoes into a spin-echo sequence, sampling both dephasing and rephasing signals, allowing for simultaneous T_2 and T_2^* mapping, despite this not being the initial reason for its design [70]. MR phase gradients have also demonstrated the ability to quantify SPIO nanoparticles [71].

SPIO has additional complications when quantifying using relaxometry. These include susceptibilities that arise at air-tissue boundaries contributing to T_2^*, cell proliferation leading to an unmeasurable dilution in the loading rates, and indistinguishable T_2^* between free and loaded cells, as well as living or dead cells loaded with iron oxide particles. Similarly to Gd, some of these issues can be surmounted with access to further relaxometry maps, with T_2 mapping providing additional separation between loaded and free SPIO [72].

These techniques require sampling of many time points to accurately quantify contrast agents. The theoretical maximum amount of contrast agent that can be measured is limited by the minimum TE that can be obtained, which is ultimately a hardware limitation.

Relaxometry methods of quantifying contrast agents are inherently more accurate than signal-based methods, as they don't require estimation of contrast agent volumes. They are however still mostly limited to a single relaxation rate parameter, and therefore restricted to the quantification of a single contrast agent at once. Even then, local tissue composition and behaviour can introduce errors, which could be corrected with access to simultaneous relaxometry maps for different parameters.

1.5 The Need for Dual Contrast Agent Quantification

Given the complexity of the systems studied using cellular quantification, it is often beneficial to combine two cell tracking methods simultaneously, either to use one technique as a validation to the other or to provide additional information about a related secondary cellular mechanism. While performing cellular quantification with MRI, secondary tracking methods such as PET can be used alongside the tracking of SPIO loaded cells, but this requires a multi-modal hardware setup. In cases where these are not available, repeat experiments are necessary to gain additional information, targeting separate mechanisms each time. This added step reduces the effectiveness of studies, as immune behaviour has been shown to vary even between clonogenic mice of the same strain [17].

If instead, two MR contrast agents could be utilized simultaneously, not only would the efficacy of studies be improved, but overall scan times could be decreased, as well as the number of subjects required for studies. However, to separate two contrast agents, more than one parameter map must be obtained simultaneously, and in a time-frame which captures the labelled molecular dynamics.

Multiparameter mapping of relaxivities has been attempted for over a decade, but none have seen widespread adoption due to the resulting complications that arise. bSSFP has been utilized to provide T_1 and T_2 mapping simultaneously, via fitting parameters to an analytical expression modelling monoexponential decay [73], but these models do not account for slice profile deviations, off-resonance effects, B1 inhomogeneity, or finite RF excitation, and so several corrections are required which can up to triple the scan time to longer than imaging individual maps [74].

Another method for multiparameter mapping is quantification of relaxation times and proton density by twin-echo saturation-recovery turbo-field echo (QRAPTEST), which allows for simultaneous quantification of T_1, T_2, and proton density in a single sequence [75]. QRAPTEST was designed to be for clinical use, but as a gradient-echo sequence, it was found to be too sensitive to susceptibility effects, leading to blurring at the edge of tissue with longer echo times. QRAPTEST's maximum excitation angle is also limited to less than 8°, limiting the maximum range of mapping. This design was iterated on to provide a spin-echo sequence with no excitation angle limitations (QRAPMASTER) and forms the basis of the magnetic resonance image compilation

(MAGiC) sequence [76].

Several other examples of such sequences exist, including the gradient echo sampling of FID and echo (GESFIDE) method to jointly measure T_2 and T_2^* by acquiring both FID as well as spin-echo signal [77], a multi-echo MP2RAGE allowing simultaneous 3D mapping of T_1, T_2^*, and susceptibility [78], and the triple echo in the steady state (TESS) method, enabling rapid relaxometry using an iterative golden section search algorithm [79]. However, all of these sequences have difficulty with further acceleration. More niche methods have been developed, such as a myocardial infarction dual quantification technique which relies on rapidly switching between T_1 and T_2 mapping segments of a sequence based on ECG triggers [80, 81], but until recently no sequence has provided flexible, reliable, and fast multiparametric mapping sufficient for dual contrast agent quantification.

1.5.1 Magnetic Resonance Fingerprinting

MRF is a novel acquisition and reconstruction strategy that can generate multiple parameter maps simultaneously [82]. Unlike other multiparameter mapping methods, MRF has proven to be robust to undersampling artifacts [83], allowing for greatly accelerated acquisition times.

MRF relies on pseudorandom variation of sequence parameters, such as echo time, repetition time, and flip angle, throughout acquisition, leading to a constantly evolving signal instead of approaching steady state. The specifics of how the parameters are varied is not critical to the function of MRF sequences, but studies have shown that certain patterns increase sensitivity to desired relaxation rates [84]; what matters is that the pseudorandom variation is known.

The produced signal is by itself useless, but its dynamics are well described by the Bloch equations for a balanced steady state free precession (bSSFP) type sequence [82], or by extended phase graphing (EPG) for a steady state free precession (SSFP) type sequence [85]. Using one of these models, along with the known parameter variation, it is possible to create a simulation of expected signal evolutions for any values of relaxation parameters. A collection of such signals for a range of relaxation rates is known as a 'dictionary'. By comparing the signal produced at each voxel to the dictionary, we can find the best match, and therefore provide an estimation of all

the relaxation rates at this point that were included in the model.

MRF is accurate when acquiring T_1 and T_2 maps using both SSFP and bSSFP implementations, with bSSFP sequences providing higher signal-to-noise ratio (SNR), but at the cost of off-resonance artifacts and a lack of sensitivity to T_2^* [87]. bSSFP has the added complication of requiring off-resonance calculations within the dictionary simulation, leading directly to an increase in dictionary size by two orders of magnitude. As the size of the dictionary directly affects post-processing time, SSFP can, therefore, be processed 100x faster. Fast matching algorithms have been produced to attempt to circumvent this, but as these algorithms also can be applied to SSFP dictionaries, dictionary generation and searching remain slower for bSSFP sequences [88].

As a basis for MRF, SSFP is not without its drawbacks. It has lower SNR, which is less desirable especially on single-channel preclinical machines used in immunology studies, but makes up for this with increased sensitivity to T_2^*, as well as a much smaller dictionary. Due to unbalanced gradients, the more complicated EPG model is required for dictionary simulation. However, this increase in complexity does not come at the cost of computation time.

MRF traditionally adopts a variable density spiral readout to capture the center of k-space while providing acceleration factors of up to 48x, resulting in a minimal compromise to data integrity, albeit on multichannel coils [89]. However, Cartesian readouts still see niche use, such as in the implementation of regularly incremented phase encoding (RIPE), where phase encode lines are incremented at each frame, leading to improved imaging of respiratory and cardiac motion [90].

More recently, there has been an increased interest in further accelerating MRF sequences to allow for larger area coverage, or finer resolution, in a given timeframe. This has led to the development of 3D MRF, where the greater SNR efficiency of 3D sequences is utilized to accelerate acquisition times. This was first attempted with a stack-of-spirals approach, where acceleration was gained through undersampling in the partition-encoding direction [91], introducing additional complications, such as the need for B1 correction to accurately measure parameters, and an increase to motion sensitivity, but demonstrating a large SNR efficiency gain of traditional 2D MRF.

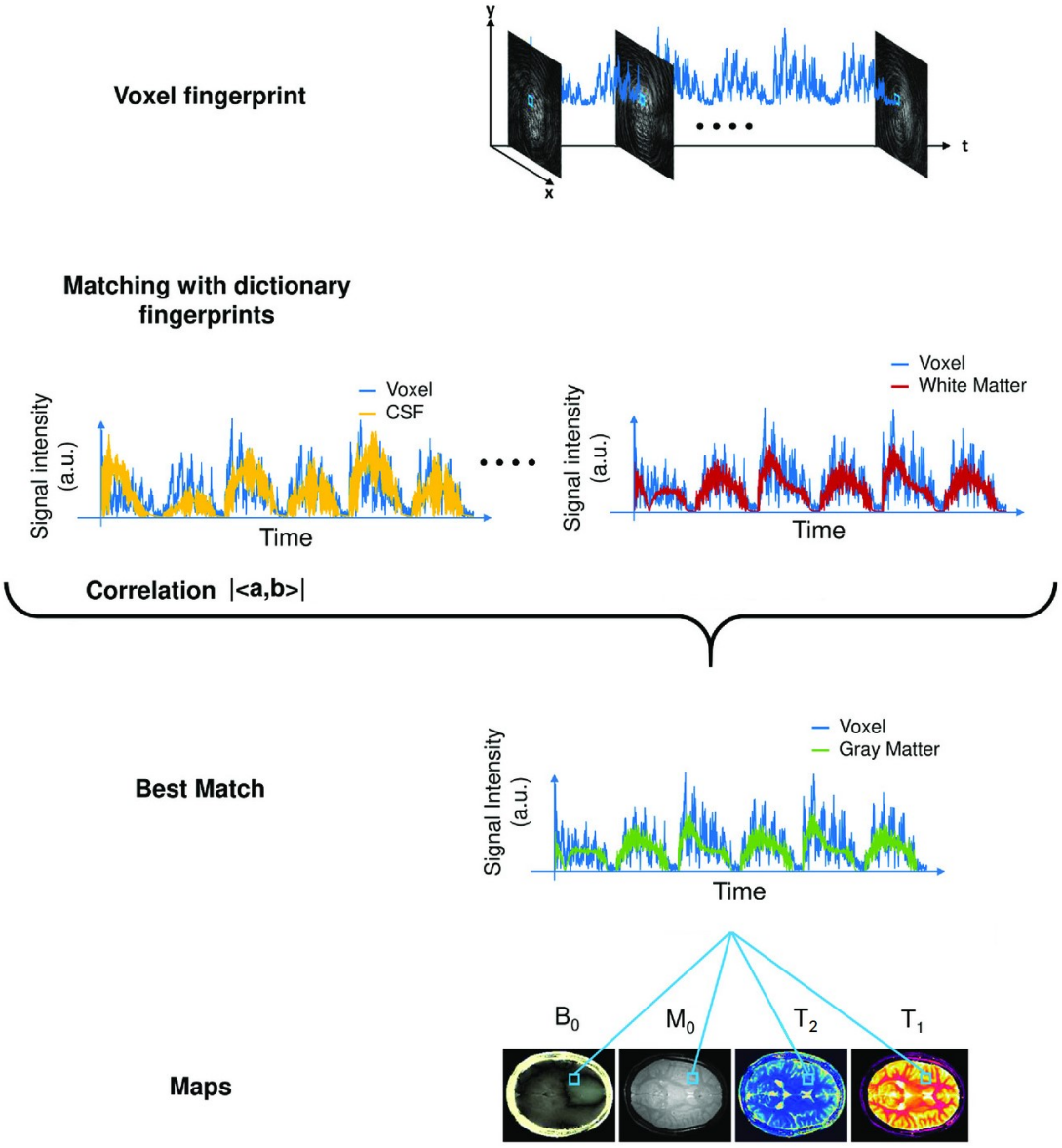

Figure 1.2: Fingerprint matching concept [86]. A signal from each voxel is compared to all entries of different tissue types within the dictionary. The highest correlation is taken to be the best representation of that voxel, and so the parameter values used to create that dictionary entry are assigned to that voxel. When repeated for all voxels, multiple parameter maps are produced in a single scan.

This design has been further iterated upon by introducing parallel imaging, with the addition of either a Sliding Window approach [92], or with the introduction of deep learning to lower the length of pseudorandom parameter variation required for a suitable match [93], and while these provided further acceleration, both of these studies relied on having access to multiple channel coils.

More novel 3D trajectories have also been proposed in the pursuit of sequence acceleration. A multi-axis spiral projection imaging approach has been proposed [94], due to its centroidal interleaves leading to decreased motion sensitivity. This resulted in a disk of interleaves rotating around each plane in turn, leading to a spherical k-space able to achieve fast quantitative imaging for a whole-brain scan. Another 3D trajectory proposed is pseudorandom cartesian sampling in the through-plane, with each readout being assigned a different static TE value, in an attempt to improve robustness to imperfection in the imaging gradients and off-resonance effects [95].

MRF's fast and powerful multiple parameter map acquisition allows for the possibility of quantifying multiple contrast agents simultaneously using MRI. Previous studies have shown that T_1 and T_2 maps acquired using MRF can separate two contrast agents, demonstrating that Gd and Mn contrast agents in various mixed concentrations can be separated and quantified *in vitro* to a high degree of accuracy [96]. Unfortunately, due to the prevalence of SPIO in cellular immunotherapy studies, this implementation would lack the required T_2^* sensitivity for dual contrast cell tracking.

Traditionally, most MRF sequences measure T_1 and T_2 parameter maps, but there is increasing interest in MRF including T_2^* quantification. Initial methods focused on TE variation, such as the inclusion of a sinusoidally varying TE appended to a traditional MRF sequence [97], or adding periodic SPGR sections to the sequence, with rapidly varying TE [98]. Recently there have been some more creative solutions, such as quadratic phase MRF, which varies the sequence phase and expands the dictionary with a Lorentzian distribution to simulate T_2^* effects [99]. However, T_2^* adapted MRF has yet to be shown to allow for the simultaneous quantification of SPIO labelled cells and a second agent. The development of such a sequence will form the basis of the proposed research.

1.6 Project Overview and Hypotheses

The objective of this project is as follows: To develop and apply an implementation of MRF which includes sufficient T_2^* mapping to quantify SPIO labelled cells and a gadolinium contrast agent *in vivo*, in 3D, within a preclinically acceptable scan time of approximately 20 mins. Dual quantification of these two agents *in vivo* would allow for studies mapping complex molecular interactions, such as immunotherapy drug location and cell death maps simultaneously.

The implementation of MRF is described in Chapter 3. Chapter 4 covers the introduction of TE modulation to provide T_2^* sensitivity to MRF, and applies this *in vitro* to demonstrate dual contrast quantification of both a Gd and SPIO agent simultaneously. Pilot *in vivo* data is also included, highlighting the need for acceleration to apply this technique in biological studies.

Chapter 5 tackles the acceleration problem posed in the previous section, but introducing modifications to T_2^* MRF that provide the required speed increase for *in vivo* application. Finally, Chapter 6 demonstrates T_2^* MRF's ability to provide dual contrast quantification *in vivo*, in a biologically appropriate time frame.

Chapter 2

Theory

2.1 Nuclear Magnetic Resonance

Any in-depth discussion of the mathematical background of MRI must first start with a description of the phenomenon of Nuclear Magnetic Resonance (NMR). Atomic nuclei are inherently quantum mechanical in their nature; observing a singular nucleus will result in an observation which has a discrete set of possibilities. However, while observing large collections of nuclei the measurement will often appear continuous at this macroscopic level, referred to as ensemble behaviour. Nonetheless, while a classical description of NMR is often sufficient for use in MRI, ^{1}H atoms are spin $\frac{1}{2}$ particles exhibiting quantum mechanical behaviour. Therefore, we will begin with a brief description the quantum mechanics behind NMR, followed by the more intuitive semi-classical description.

2.1.1 Quantum Mechanical Description

In a quantum mechanical framework, nuclei have an intrinsic angular momentum, or spin. This spin $\vec{S}$ generates a proportional magnetic moment

$$\vec{\mu} = \gamma \vec{S} \tag{2.1}$$

where γ is the gyromagnetic ratio of the nucleus in question. For MRI, this is almost always the ^{1}H nucleus, with $\gamma = 2.68 \times 10^8$ rad/s/T.

For the purposes of NMR, we are interested in how these spins behave and interact in a strong magnetic field. In a magnetic field $\vec{B_0}$, this magnetic moment has energy

$$E = \vec{\mu} \cdot \vec{B_0} \tag{2.2}$$

By combining equations 2.1 and 2.2, and noting that the Hamiltonian operator corresponds to the total energy of the system, when we constrain the $\vec{B_0}$ field to the

z-axis we can write the Hamiltonian of the nucleus as

$$H = -\gamma B_0 S_z \tag{2.3}$$

where S_z is the z component of the spin matrix. For spin $\frac{1}{2}$ particles, the spin operators are the Pauli spin matrices

$$S_z = \frac{\hbar}{2}\begin{pmatrix} 1 & 0 \\ 0 & -1 \end{pmatrix}$$

where $\hbar$ is the Planck's constant, divided by 2π. The z Pauli spin matrix has two eigenstates, which can be thought of as corresponding to if the magnetic moment is parallel or anti-parallel to the $\vec{B_0}$ field. When inspecting the eigenvalues of the Hamiltonian in equation 2.3, we obtain 2 distinct energy levels

$$E_\uparrow = -\hbar\gamma B_0/2$$
$$E_\downarrow = +\hbar\gamma B_0/2$$

with the 'spin-up' state parallel to the $\vec{B_0}$ field having a lower energy, while the anti-parallel 'spin-down' state is a higher energy. This discrete energy level splitting is referred to as Zeeman Effect [100].

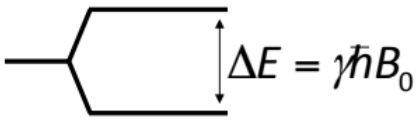

Figure 2.1: Energy level diagram of a spin 1/2 particle in external field. This quantization is referred to as the Zeeman Effect.

Transition between these two states can therefore be caused by either the emission or absorption of a photon of discrete energy ν, such that

$$\Delta E = \hbar\gamma B_0 = \hbar\omega_0 \tag{2.4}$$

where ω_0 is known as the Larmor frequency. Thus in the quantum mechanical description of NMR, the Larmor frequency describes the energy needed to transition between energy states for a nucleus.

The distribution of spins between the high and low energy states, also known as spins anti-parallel or parallel to the external magnetic field, is related to the thermal energy of the system, with the equilibrium state seeing a slight bias towards the low energy. This is described by a Boltzmann distribution

$$\frac{N_{\downarrow}}{N_{\uparrow}} = exp(-\Delta E/k_B T) \tag{2.5}$$

where T is the temperature, and k_B is the Boltzmann constant (1.38×10^{-23} J/K). For a room temperature experiment in an external field strength of 3T, the difference between the population of parallel and anti-parallel spins is 1 for every 1 million nuclei. Altering these variables can lead to an increase in population difference, which can be valuable for nuclei with a lower γ value, or when imaging nuclei not endogenous to the system.

The quantum mechanical framework can lead on from here to provide descriptions for the relaxation mechanics of NMR, but for our purposes it is only important to recognize that NMR is indeed a quantum mechanical process. Thankfully, a semi-classical description of phenomena such as relaxation is far more intuitive, and so the bulk of this work will rely on this description.

2.1.2 Semi-classical Description

In the semi-classical description of NMR, protons are visualised as precessing balls. As the protons carry charge, this precession induces a magnetic field, and so in this framework, protons can be thought of as tiny bar magnets with magnetic moment $\vec{\mu}$, as illustrated in Figure 2.2.

The magnetic moment of the proton is related to the angular momentum $\vec{L}$ by the gyromagnetic ratio γ

$$\vec{\mu} = \gamma \vec{L} \tag{2.6}$$

In the absence of a magnetic field, the system is in thermal equilibrium, and so these bar magnets are randomly oriented. However, when placed in a magnetic field $\vec{B_0}$, these bar magnets experience a torque $\vec{\tau}$

$$\vec{\tau} = \vec{\mu} \times \vec{B_0} \tag{2.7}$$

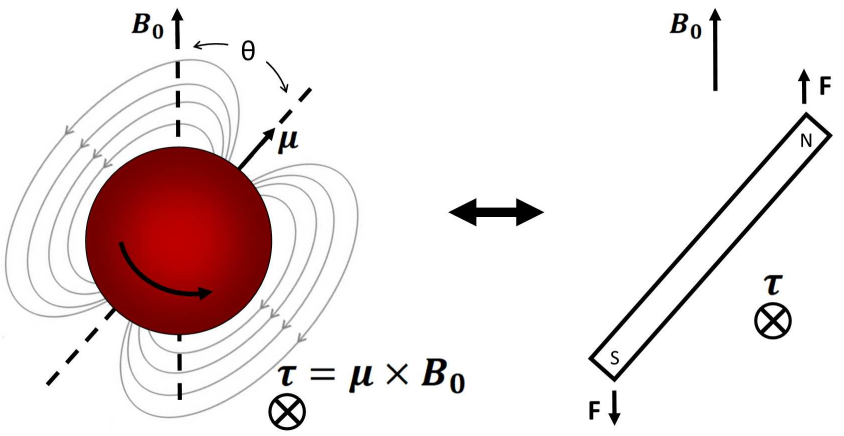

Figure 2.2: Semiclassical model of a protons magnetic moment $\vec{\mu}$. The precession of a proton creates a magnetic field which can be thought of as a bar magnet. When placed in an external magnetic field $\vec{B_0}$, the magnetic moment $\vec{\mu}$ experiences a torque $\vec{\tau}$.

This alignment is not perfect, instead leading $\vec{\mu}$ to precess aligned to the magnetic field at a constant angle θ, analogous to a gyroscope in a gravitational field. As the angle θ is held constant, $\vec{\tau}$ changes direction but not magnitude, so the same can be said for the resulting angular momentum $\vec{L}$

$$\vec{\tau} = \frac{d\vec{L}}{dt} \Leftrightarrow d\vec{L} = \tau dt \tag{2.8}$$

and therefore $\vec{L}$ can be thought of as tracing a circle of radius $Lsin\theta$, in units of angular momentum [101], visualized in Figure 2.3.

We can calculate the frequency of precession of $\vec{L}$, as the speed of precession (in units of angular momentum per time) is given by $\vec{\tau}$ in Equation 2.8,

$$f = \frac{1}{time} = \frac{'speed'}{'distance'} = \frac{\tau}{2\pi L sin\theta} \tag{2.9}$$

Combining Equations 2.7 and 2.9, we find that the precession frequency can be written

$$f = \frac{\mu B_0}{2\pi L} \tag{2.10}$$

and substituting in $\vec{\mu}$ from Equation 2.6, we arrive at

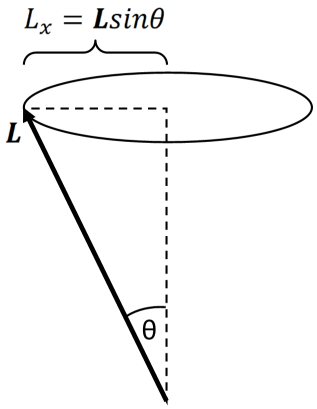

Figure 2.3: Angular momentum $\vec{L}$ of NMR. As $\vec{\tau}$ is a constant magnitude, this is also true of $\vec{L}$, allowing for the derivation of the Larmor frequency.

$$f_{Larmor} = \frac{\gamma}{2\pi} B_0 \tag{2.11}$$

or, as it's more commonly written, noting that $\omega = 2\pi f$

$$\omega_0 = \gamma B_0 \tag{2.12}$$

Analogous to the quantum mechanical description, we arrive at the Larmor frequency, which in the classical description is the frequency of precession for a given field strength. For MRI, the Larmor frequency of a proton in a 3 Tesla magnetic field is approximately 128 MHz.

While the presence of an external field produces a small net magnetization, without careful and deliberate manipulation this is immeasurable. The goal is to measure the net magnetization $\vec{M}$ and its evolution via the application of a secondary magnetic field. Thus the interest of the observer is not the Larmor precession of $\vec{M}$, but the additional behaviour during excitation and relaxation.

This excitation is performed by successive applications of a smaller magnetic field $\vec{B_1}$. However, prior to discussing this mathematically, it is convenient to introduce a coordinate system that suppresses the Larmor precession from the visualization and equations, greatly simplifying conceptualization.

We introduce the rotating frame, a coordinate system in which the z-axis stays aligned with the traditional laboratory z-axis, but the x and y axes are rotated at the

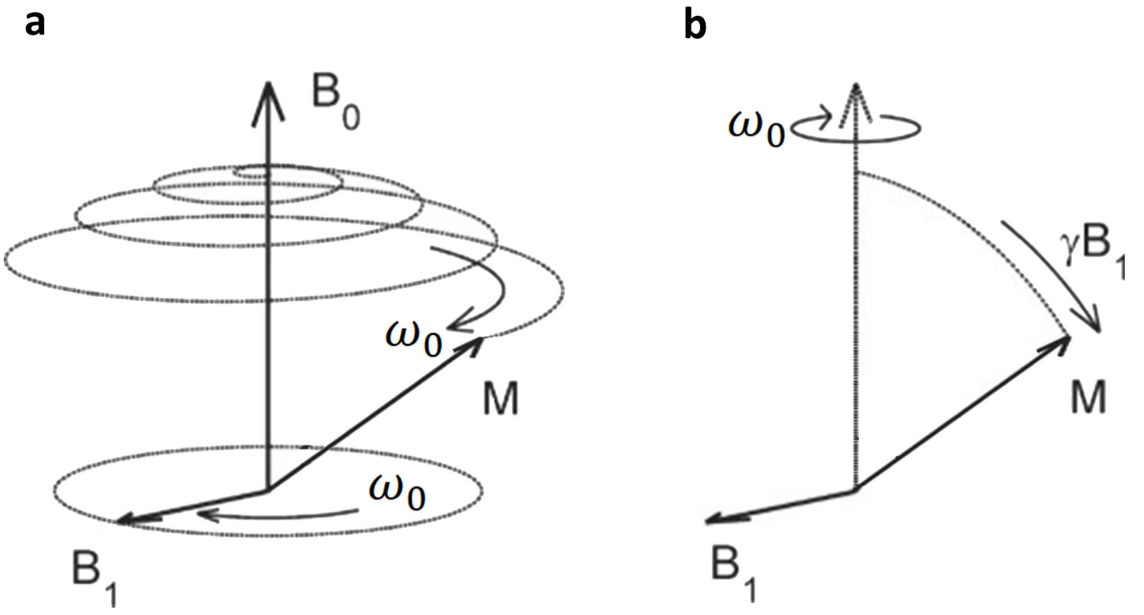

Figure 2.4: Visualization of the rotating frame. (a) Laboratory frame of reference. When a secondary field is applied perpendicular to the $\vec{B_0}$ field at the Larmor frequency ω_0, net magnetization $\vec{M}$ precesses down towards the x-y plane. (b) Rotating frame of reference, where the x-y plane precesses at frequency ω_0. This simplifies the visualisation of an on resonant $\vec{B_1}$ field, while removing the Larmor precession from the $\vec{M}$ dynamics.

precessional frequency ω_0 of the protons. In this rotating frame, the Larmor precession of the net magnetization $\vec{M}$ is completely removed. If a secondary magnetic field B_1 rotating at ω_0 (also referred to as 'on resonance') were applied perpendicular to the external $\vec{B_0}$ field, the laboratory frame of reference would observe $\vec{M}$ precessing at a wider and wider angle. However, in the rotating frame both the $\vec{B_1}$ field and $\vec{M}$ are simplified, as both are no longer rotating relative to the x' and y' axes. A visualization of this is demonstrated in Figure 2.4.

In the rotating frame, the effect of $\vec{B_1}$ on the magnetization $\vec{M}$ will precess about the axis of the $\vec{B_1}$ field at a frequency of γB_1. The angle at which $\vec{M}$ will have rotated in time t is given by the equation

$$\theta = \gamma B_1 t \tag{2.13}$$

$\vec{B_1}$ is several orders of magnitude smaller than the $\vec{B_0}$ field, and is often only applied on the order of milliseconds to rotate the net magnetization into the desired

orientation. As $\vec{B_1}$ is applied at a Larmor frequency in the radio band of the electromagnetic spectrum (for conventional $\vec{B_0}$ field strengths), this is also often referred to as a radio frequency (RF) pulse.

The equations of motion for the net magnetization $\vec{M}$ can be written

$$\frac{d\vec{M}}{dt} = \gamma\vec{M} \times \vec{B_0} \tag{2.14}$$

which, in a static external field $\vec{B_0}$ which is oriented in the z direction become

$$\frac{d\vec{M_x}}{dt} = \gamma\vec{M_y} \times \vec{B_0} \qquad \frac{d\vec{M_y}}{dt} = -\gamma\vec{M_x} \times \vec{B_0} \qquad \frac{d\vec{M_z}}{dt} = 0 \tag{2.15}$$

When combined with a relaxation component, these form the basis for the Bloch equations, which describe the behaviour of a net magnetization as a function of time.

2.1.3 Relaxation and Measurement

NMR is performed by the selective excitation and subsequent relaxation of the net magnetization within the static external field. While at equilibrium, the component of magnetization parallel to the external field, M_z, is maximal. This is referred to as longitudinal magnetization. The component of the magnetic moment in the x-y plane, M_{xy}, is referred to as the transverse magnetization, and at equilibrium is 0, as the vector components of magnetization are equally distributed in the transverse plane.

Application of a secondary field $\vec{B_1}$ perturbs this equilibrium, transferring longitudinal magnetization into the transverse plane, allowing the measurement of the resulting electric field through a suitably tuned receiver. The signal produced during the net magnetization's return to equilibrium is referred to as a free induction decay (FID), and its behaviour with respect to time can convey properties of the tissues of interest. This FID is an oscillating signal and so is more easily displayed as a frequency spectrum, which is obtained through a Fourier transform:

$$S(\omega) = \int_{-\infty}^{\infty} s(t)e^{2\pi i\omega t}dt \tag{2.16}$$

The resulting frequency spectrum imparts information on the magnetic environment of the sample. If a sample contains a homogeneous environment for the protons,

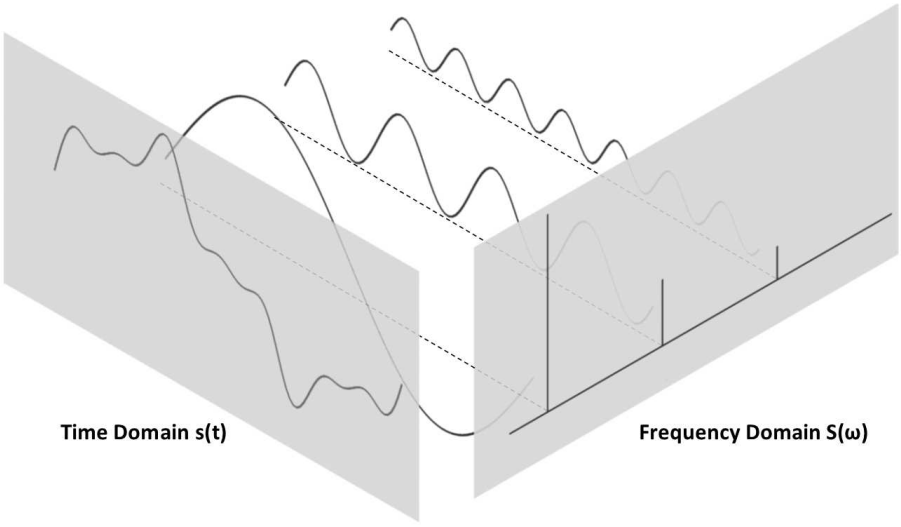

Figure 2.5: Illustration of a composite signal, similar to an expected FID without decay. The Fourier transform allows for extraction of a spectrum in the frequency domain, which is far more useful for NMR analysis.

a single peak at the Larmor frequency will be extracted. However in reality, different atomic species will be shielded from the the external field by their own electron clouds, leading to slightly different Larmor frequencies. These slight differences create a spectrum indicative of the characteristics of the scanned sample, the basis of NMR spectroscopy.

The FID will decay in two distinct ways, return to longitudinal equilibrium, and loss of transverse phase coherence. These two decay types each have an associated time constant, and are fundamental to MRI.

Return to longitudinal equilibrium is caused by individual spins releasing their energy into local tissue, known as spin-lattice relaxation. This is dependent on the molecular structure and arrangement of the local area, and results in an exponential growth in the M_z component of magnetization. The time for 63% of the longitudinal magnetization to recover is known as the T_1 relaxation, and from a fully transverse magnetization ensemble is expressed as the following differential equation

$$\frac{dM_z}{dt} = \frac{1}{T_1}(M_0 - M_z) \tag{2.17}$$

with M_0 the maximum longitudinal magnetization, and t is time. This differential equation has the solution

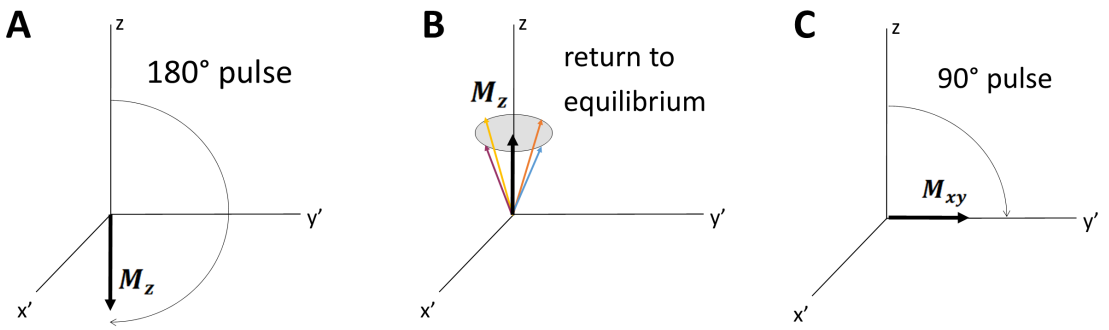

Figure 2.6: Example pulse sequence for the extraction of T_1 data of a sample. (a) A 180° RF pulse is applied to move the magnetization into the -z plane. (b) After some time, the net magnetization with have undergone some return to equilibrium. (c) A 90° pulse brings the net longitudinal magnetization into the transverse plane, where it can be measured.

$$M_z(t) = M_0[1 - exp(-t/T_1)] \tag{2.18}$$

T_1 is shortest in systems where the vibrational frequencies are closest to the resonant frequency, typically solid and slowly moving structures, as this makes for the most efficient energy transfer into the lattice.

One method to determine T_1 is demonstrated in Figure 2.6. The magnetization is initially inverted against its equilibrium position by a 180° RF pulse. The magnetization is then given time to partially return to equilibrium, referred to as inversion time, or TI. A 90° RF pulse then moves the longitudinal magnetization into the transverse plane, allowing for measurement by the receiver coil. By performing this sequence in series with different values for TI, results can be fit to Equation 2.18 to find a value for T_1.

Transverse magnetization decay is the dephasing of a coherent precession signal within the x-y plane. At equilibrium the transverse magnetization is uniformly spread 360°, however the addition of a short RF pulse will temporarily bring the individual spins into phase, creating a net transverse magnetization $\vec{M_{xy}}$. This is the magnetization oscillation that induces current in the receiver, leading to a measurable FID. With time, the shared phase of $\vec{M_{xy}}$ decays, reverting to a net transverse magnetization of 0. The time in which the maximal transverse magnetization takes to decay to 37% signal is known as T_2, and is related to $\vec{M_{xy}}$ by the following differential equation

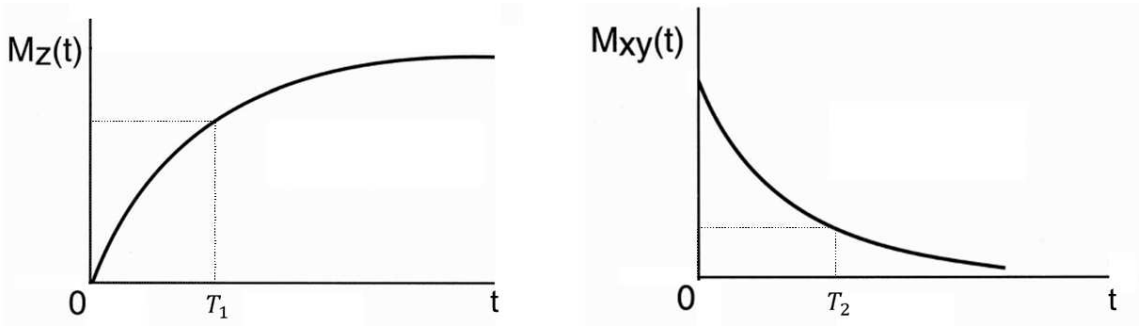

Figure 2.7: Types of relaxation experienced by a magnetic spin ensemble in an external field. M_z returns to longitudinal maximum after being knocked down, whereas $\vec{M}_{xy}$ decays back to 0 net magnetization. Each has an associated time constant, T_1 and T_2 respectively.

$$\frac{d\vec{M}_{xy}}{dt} = -\frac{1}{T_2}\vec{M}_{xy} \tag{2.19}$$

with the following solution

$$\vec{M}_{xy}(t) = M_0 exp(-t/T_2) \tag{2.20}$$

where M_0 is the signal produced from transverse magnetization coherence, and t is time. Both of these equations are expressed in the rotating frame.

Transverse magnetization decay is due to magnetic inhomogeneity within the sample, leading to individual spins precessing at slightly slower or faster than the Larmor frequency via a spin-spin interaction. This field inhomogeneity effect is obscured by fast or rapid molecular motion, so liquids often have a long T_2 time when compared to solids or large molecules.

Transverse decay can be broken down into intrinsic and extrinsic components. Intrinsic inhomogeneity refers to the local spin-spin interaction causing dephasing, while extrinsic sources of dephasing include external field inhomogeneities or the introduction of a high Z element into the sample. The transverse decay including all of these components can be viewed as the 'effective' T_2, and is referred to as T_2^*. These two are related by

$$\frac{1}{T_2^*} = \frac{1}{T_2} + \frac{1}{T_{inhom}} \tag{2.21}$$

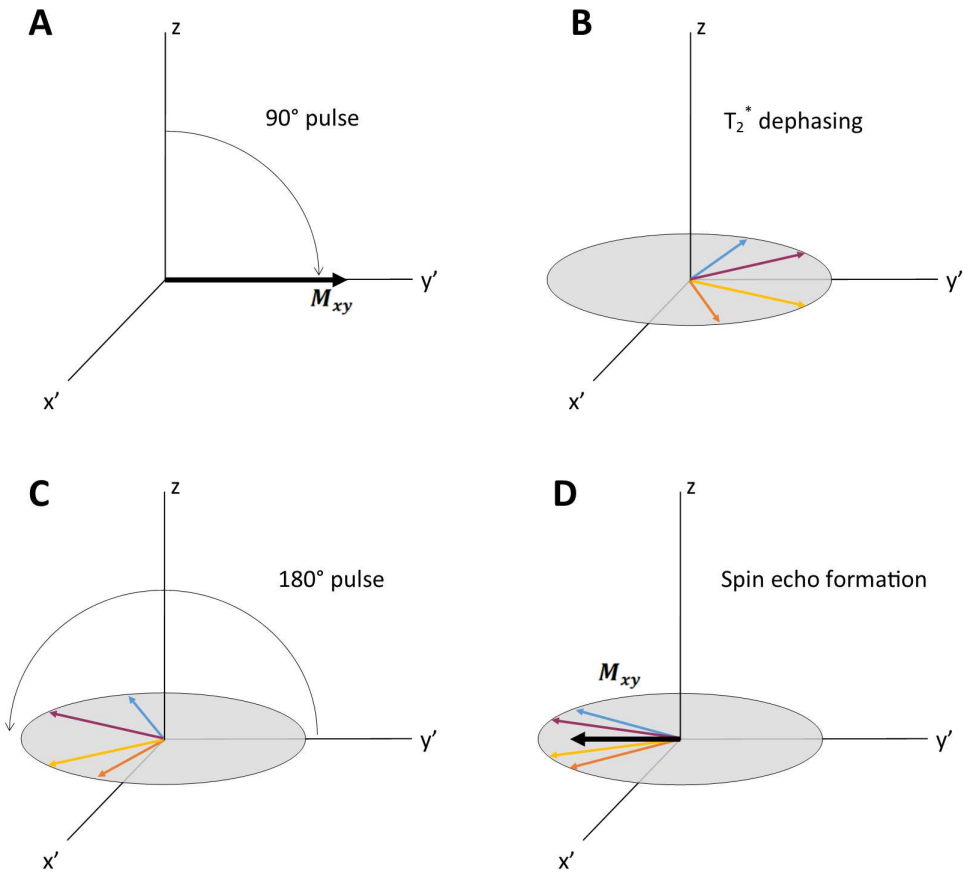

Figure 2.8: Spin echo sequence. (a) A 90° pulse brings the magnetization into the transverse plane. (b) T_2^* decay occurs, dephasing the magnetization. (c) A 180° pulse flips the transverse magnetization. (d) An echo is formed, as the T_2^* effects are temporarily negated, leading to an accurate measurement of T_2.

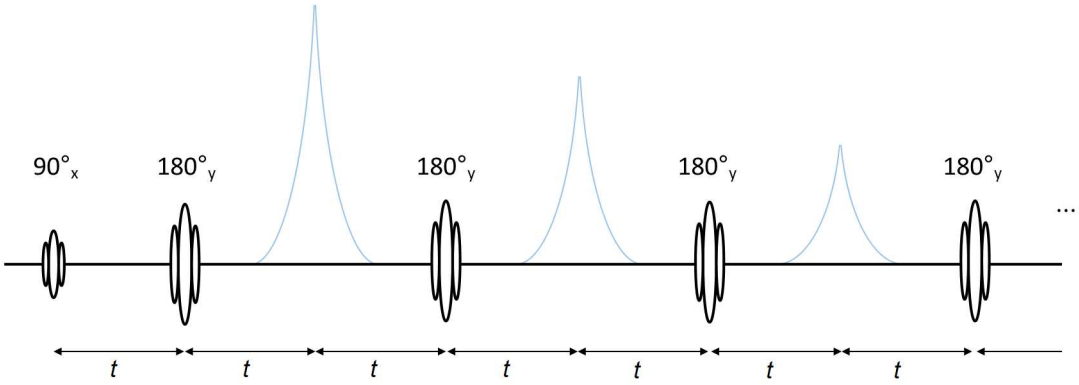

Figure 2.9: CPMG sequence. By repeated application of a 180° pulse, a train of spin echoes can be induced, with their amplitudes decaying as a function of T_2.

Measurement of T_2 therefore requires pulse sequences that intentionally reverse the effects of T_2^*. Once such method is shown in Figure 2.8, the spin echo, where after an initial 90° pulse to shift magnetization into the transverse plane, dephasing occurs according to T_2^*. After time t, a 180° pulse flips the magnetic moments in the x-y plane. Magnetic moments that have precessed further out of phase will now be further away from the point of echo formation, whereas slower precessing spins will be nearer. After another t, an echo will be formed, which results in a reading for the T_2 decay only. These 180° pulses can be applied in succession in what is known as a spin echo train. This is visualized in Figure 2.9, where spin echoes are continuously generated by alternating between a 180° flip and a readout of the magnetization every subsequent t. This is known as a CPMG sequence, named after its inventors, Carr, Purcell, Meiboom, and Gill [102].

These two relaxation types can be utilised simultaneously to provide more complex sequences with mixed T_1 and T_2 contrast. One example is the stimulated echo, demonstrated in Figure 2.10, where after beginning similarly to a spin echo pulse sequence, a 90° RF pulse shifts the T_2^* dephased magnetic moments into the longitudinal axis, causing subsequent relaxation to be primarily driven by T_1. The sequences used in this work, SSFP and bSSFP, are other examples of mixed T_1 and T_2 contrast, and will be discussed in further detail in a later section.

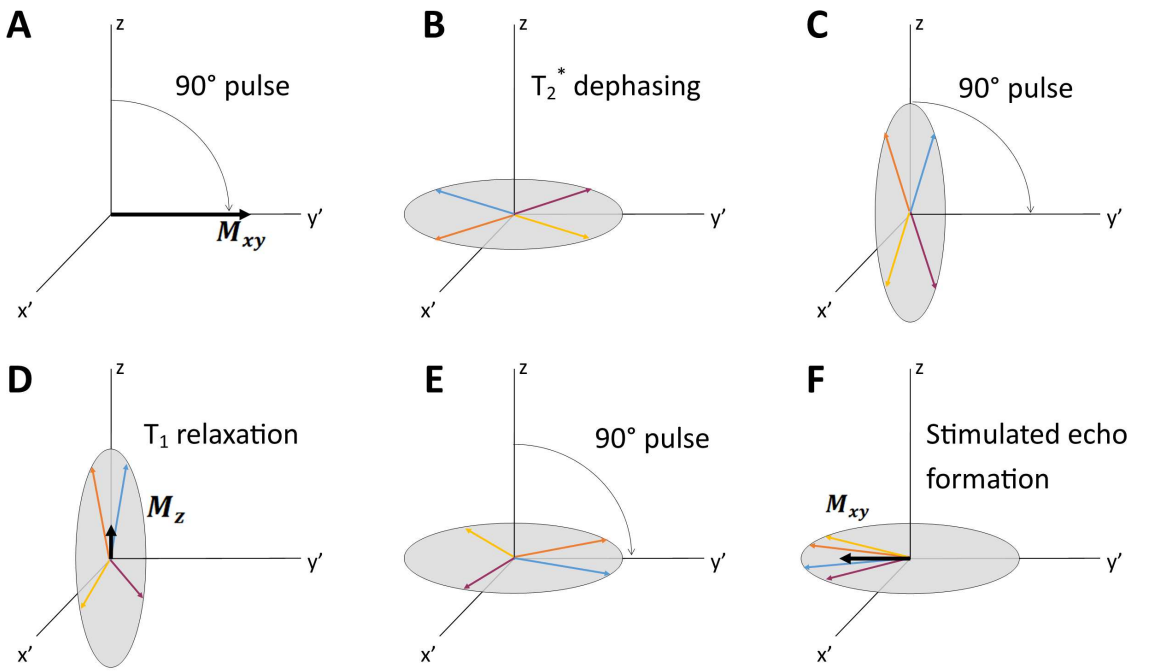

Figure 2.10: Stimulated echo sequence. (a) A 90° pulse brings the net magnetism into phase in the transverse plane, similar to a spin echo sequence. (c) After T_2^* dephasing, a second 90° pulse is applied, flipping the dephasing magnetic moments into the longitudinal plane. (d) Relaxation in the longitudinal plane is dominated by T_1 relaxation. (f) After a third 90° pulse, the resulting echo is based on both T_1 and T_2.

2.1.4 The Bloch Equation

The differential Equations 2.14, 2.17, and 2.19 can be combined to provide a generalized equation for bulk magnetization in the presence of a magnetic field including its relaxation terms. This was first proposed by Felix Bloch in 1946 [103].

$$\frac{dM}{dt} = \gamma \vec{M} \times \vec{B_0} + \frac{1}{T_1}(M_0 - M_z) - \frac{1}{T_2}\vec{M_{xy}} \tag{2.22}$$

This is known as the Bloch equation, and provides a description of the return to equilibrium, given the external field is aligned with the z-axis. In the case of a constant external field, the cross product produces three component equations as seen previously in Equation 2.15.

$$\frac{dM_x}{dt} = \omega_0 M_y - \frac{M_x}{T_2} \tag{2.23}$$

$$\frac{dM_y}{dt} = -\omega_0 M_x - \frac{M_y}{T_2} \tag{2.24}$$

$$\frac{dM_z}{dt} = \frac{M_0 - M_z}{T_1} \tag{2.25}$$

where M_0 is the equilibrium magnetization along the z axis. The solution for these equations can be found be introducing the integrating factors $M_x = m_x exp(-t/T_2)$ and $M_y = m_y exp(-t/T_2)$

$$M_x(t) = e^{\frac{-t}{T_2}} [M_x(0) cos\omega_0 t + M_y(0) sin\omega_0 t] \tag{2.26}$$

$$M_y(t) = e^{\frac{-t}{T_2}} [M_y(0) cos\omega_0 t - M_x(0) sin\omega_0 t] \tag{2.27}$$

$$M_z(t) = M_z(0) e^{\frac{-t}{T_1}} + M_0 \left(1 - e^{\frac{-t}{T_1}} \right) \tag{2.28}$$

To fully model NMR behaviour it is also necessary to mathematically describe perturbation of the magnetization with an RF pulse. To this end, it is often more convenient to express the Bloch equations with operator matrices, such that Equation 2.22 becomes

$$\begin{bmatrix} M_x(t) \\ M_y(t) \\ M_z(t) \\ 1 \end{bmatrix} = X \begin{bmatrix} M_x(0) \\ M_y(0) \\ M_z(0) \\ 1 \end{bmatrix} \tag{2.29}$$

where X is can be replaced with any of the three following operators

$$T_t = \begin{bmatrix} -\frac{1}{T_2} & 0 & 0 & 0 \\ 0 & -\frac{1}{T_2} & 0 & 0 \\ 0 & 0 & -\frac{1}{T_1} & \frac{M_0}{T1} \\ 0 & 0 & 0 & 1 \end{bmatrix} \tag{2.30}$$

$$P_t = \begin{bmatrix} cos\omega_0 t & sin\omega_0 t & 0 & 0 \\ -sin\omega_0 t & cos\omega_0 t & 0 & 0 \\ 0 & 0 & 1 & 0 \\ 0 & 0 & 0 & 1 \end{bmatrix} \tag{2.31}$$

$$RF_\theta^\alpha = \begin{bmatrix} cos^2\theta + sin^2\theta cos\alpha & cos\theta sin\theta cos\alpha & -sin\theta sin\alpha & 0 \\ cos\theta sin\theta - cos\theta sin\theta cos\alpha & sin^2\theta + cos^2\theta cos\alpha & cos\theta sin\alpha & 0 \\ sin\theta sin\alpha & -cos\theta sin\alpha & cos\alpha & 0 \\ 0 & 0 & 0 & 1 \end{bmatrix} \tag{2.32}$$

Where T_t, P_t, and RF_θ^α are the operators for relaxation, precession, and RF excitation respectively. The θ and α terms in Equation 2.32 are the angle of excitation α from the arbitrary angle θ from the x-axis on the x-y plane, as shown in Figure 2.11. Note that the fourth dimension is a result of transforming the affine equation in 3D to a linear equation, to include the $\frac{M_0}{T_1}$ term in Equation 2.30.

This form allows for easy simulation of net magnetism in an static external field, including relaxation, precession, and RF excitation. Often precession is neglected as the rotating frame is used. These operators can be applied together, allowing for efficient calculation of an expected state given starting conditions. For example, the magnetization of a CPMG sequence at time of the first spin echo can be written

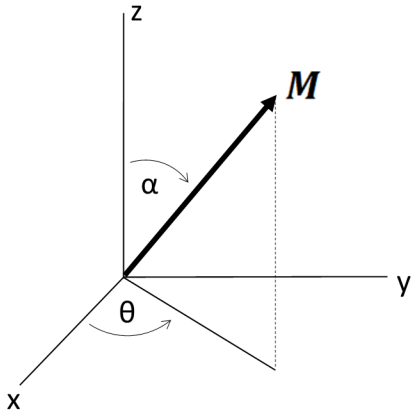

Figure 2.11: Angles of the RF pulse operator in the Bloch Equations. θ is the angle of excitation from the arbitrary angle θ from the x-axis on the x-y plane

$$\vec{M(t)} = T_t \; RF^{\pi} \; T_t \; RF^{\pi/2}_{\pi/2} \; \vec{M(0)} \tag{2.33}$$

where the order of the operators is read from right to left. The number of successive applications of operators is limited by the complexity of the sequence to be modelled, or more likely the computing power of the machine processing the simulation.

2.1.5 Extended Phase Graph Model

While the Bloch equations offer a valuable starting point to simulating NMR behaviour, there are more complicated behaviours which are neglected in the process. The Bloch equations treat magnetization within the external field as a single isochromat, when in reality it is an ensemble of isochromats. As a result, the Bloch equations struggle to accurately simulate NMR signals which are not returned to equilibrium before the next excitation, as well as a number of other parameters including systems with high diffusion. Bloch equation simulations can overcome this by including many isochromats in the simulation and averaging the results, but the elegance of the solutions are quickly lost, where ensemble data sets are time consuming to produce, and resulting data is visually unclear as to when and which type of echoes are occurring. For most applications, the Bloch equations are a sufficient approximation to observed behaviour, but are insufficient for this work.

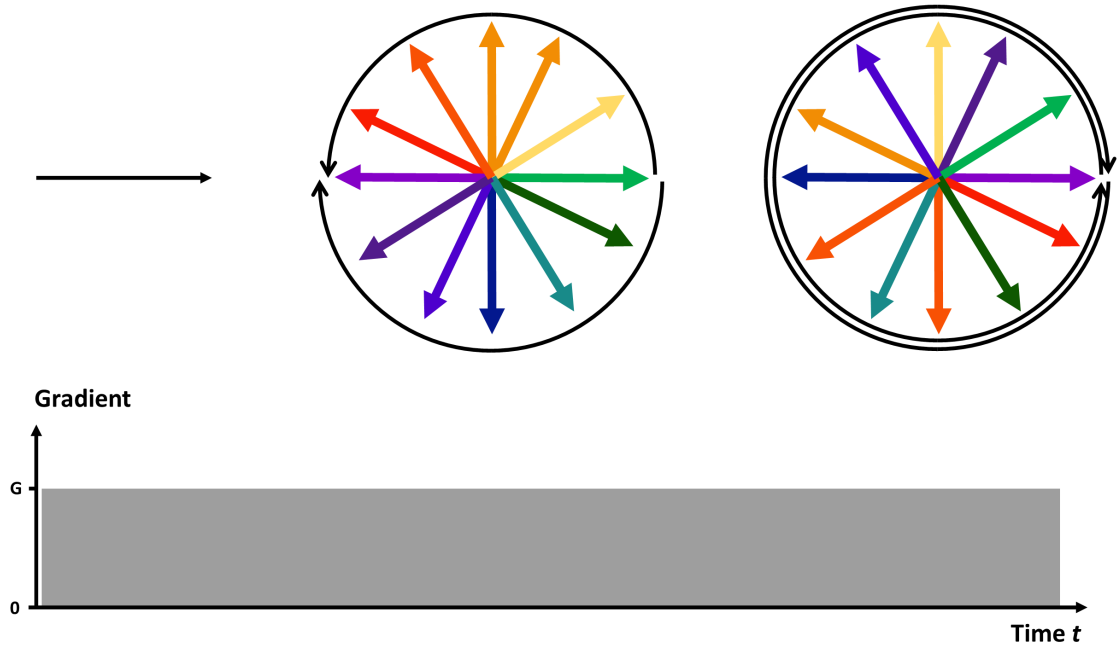

Figure 2.12: Visualisation of isochromat dephasing from an initially coherent magnetization. The 12 representative isochromats dephase linearly with time, leading to complete loss of coherent magnetization. However, further application of a gradient leads to a greater spread of isochromats when compared to the first point of complete dephasing. Subsequent full turns, known as higher order configuration states, are not captured with traditional rotation operator algorithms used for modelling the Bloch equations. EPG allows these higher order configuration states to be accounted for in a computationally efficient manner.

Extended Phase Graphing (EPG) offers a powerful and computationally efficient alternative for simulating sequences under such conditions without needing to solve the Bloch equation for thousands of isochromats. EPG is effectively a method of tracking the dephasing of isochromats which occur during application of a gradient, such as to spatial encoding, or spoiler gradients, which will be discussed in the next section. The following derivations can be found in [85].

To fully capture the higher spatial frequency components of a dephased isochromat ensemble, EPG begins by defining the equation of motion for a single isochomat of magnitude $\vec{M}$ at a position $\vec{r}$ from the center on-resonant isochromat. This can be visualised by imagining the off resonance isochromats winding a helix, where the isochromat at the bottom of the helix is the on-resonant isochromat, and the helix is spread along the direction of the gradient, as visualized in Figures 2.12 and 2.13 A.

This yields the following equations of motion

$$M_x(\vec{r}) = Mcos\left(\gamma\vec{r}\int_0^t \vec{G}(t')dt'\right) = Mcos(\vec{kr}) \tag{2.34}$$

$$M_y(\vec{r}) = Msin\left(\gamma\vec{r}\int_0^t \vec{G}(t')dt'\right) = Msin(\vec{kr}) \tag{2.35}$$

where the phase angle is defined as $\phi(\vec{r}) = \int_0^t \gamma\vec{G}(t')\vec{r}dt'$ as shown in Figure 2.13 B, and the final step relies on noting that $\vec{G}$ and $\vec{k}$ are related by $\vec{k} = \frac{2\pi}{\gamma}\int_0^t \vec{G}(t')dt'$. $\vec{k}$ is shown to represent a quantitative measure of dephasing, as seen in a previous section on k-space. We see that a dephasing gradient generates time-dependent harmonic magnetization components along the spatial axes, which can instead be written as complex magnetization components

$$M_+(\vec{r}) = M_x(\vec{r}) + iM_y(\vec{r}) = \vec{M}e^{i\phi(\vec{r})} = \vec{M}e^{i\vec{k}\vec{r}} = (M_-)^* \tag{2.36}$$

$$M_-(\vec{r}) = M_x(\vec{r}) - iM_y(\vec{r}) = \vec{M}e^{-i\phi(\vec{r})} = \vec{M}e^{-i\vec{k}\vec{r}} = (M_+)^* \tag{2.37}$$

In this notation, M_+ and M_- are shown to be complex conjugates of each other, and from Figure 2.13 B can be shown to be related by M_+ leading to M_- via a 180° refocusing pulse in the x-axis, This allows us to model refocusing pulses within this framework as a complex conjugate operation.

We are interested in modelling the net magnetization, or sum of all isochromats in the gradient direction. This is equivalent to the integral $\int Me^{i\vec{k}\vec{r}}d^3r$ in the continuous limit, where we expect several different orders of dephasing to be present, and can be written as follows

$$\tilde{F}_+(\vec{k}) = \int_V \Big(M_x(\vec{r}) + iM_y(\vec{r})\Big)e^{-i\vec{k}\vec{r}}d^3r = \int_V M_+(\vec{r})e^{-i\vec{k}\vec{r}}d^3r \tag{2.38}$$

$$\iff M_x(\vec{r}) + iM_y(\vec{r}) = M_+(\vec{r}) = \int_V \tilde{F}_+(\vec{k})e^{i\vec{k}\vec{r}}d^3k \tag{2.39}$$

i.e., transverse magnetization can be interpreted as a sum of complex helices with different wave vectors $\vec{k}$ This abstract concept is visualized in Figure 2.14. In effect, this means that magnetization in this framework is defined in 'configuration states'

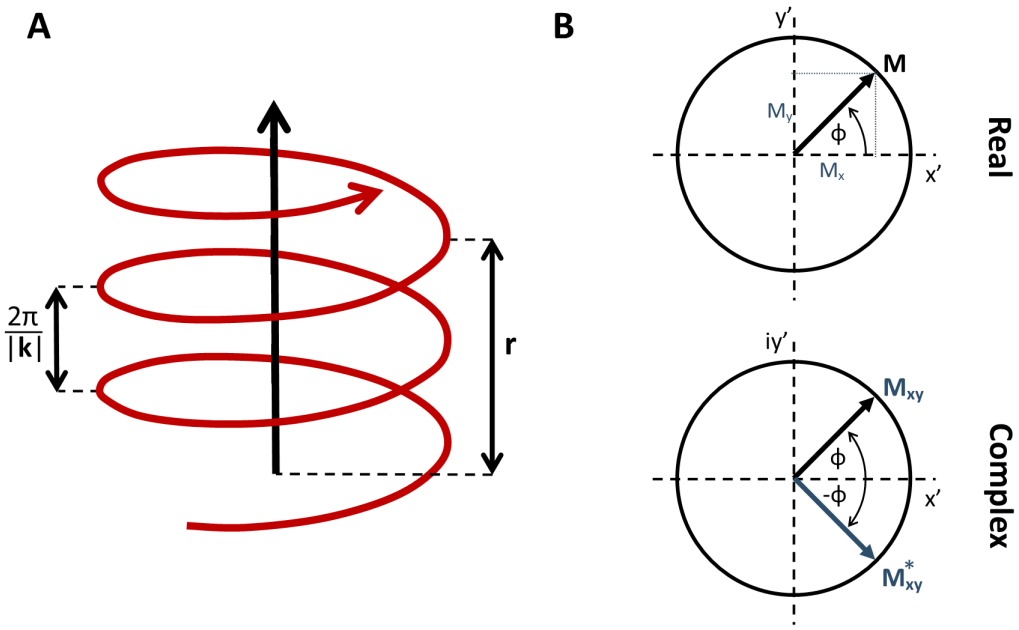

Figure 2.13: Mathematical definition of a single isochromat dephasing from an initially coherent magnetization. A) An ensemble of isochromats along a generalized 1D axis where a gradient is being applied winds isochromats into a helix configuration. Here $\vec{r}$ can be visualised as the distance from the on-resonance isochromat, which is in this helix is assumed to be at the bottom. The pitch of the helix is related to the gradient strength and time applied. B) Top-down view of the transverse magnetization vector $\vec{M}$, which can allow for a change of basis to complex coordinates, simplifying the equations of motion.

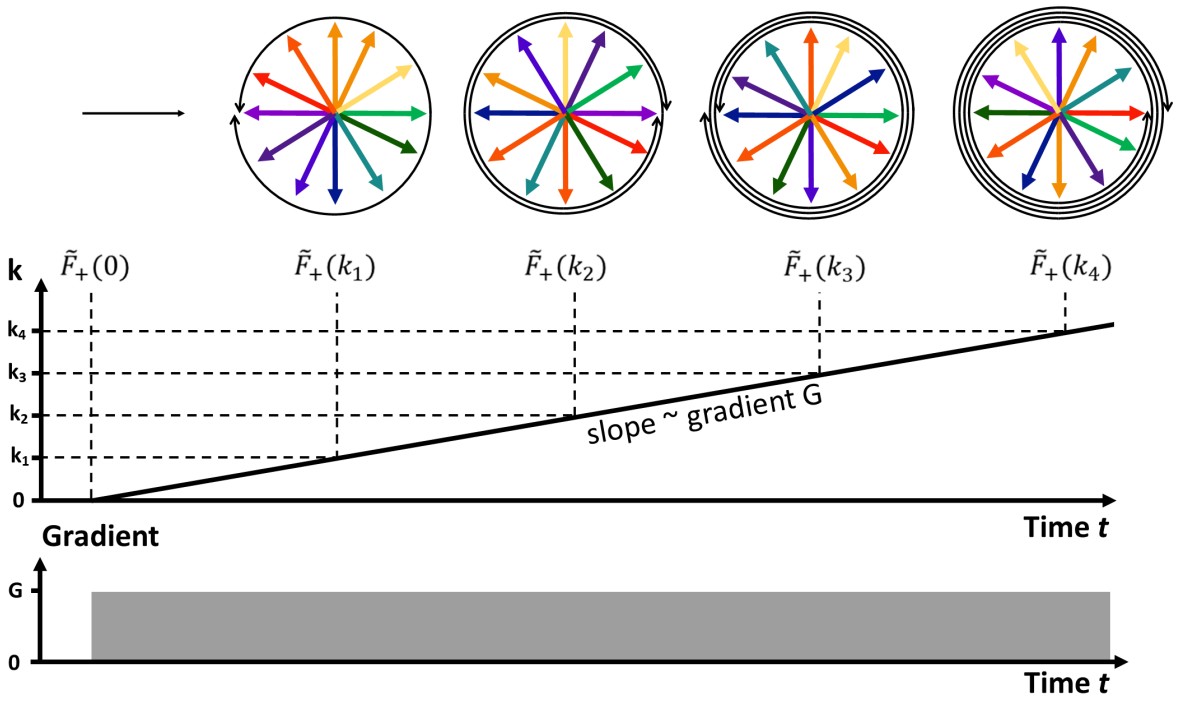

Figure 2.14: EPG allows for expression of transverse magnetization in terms of $\vec{k}$, corresponding to configuration states $\tilde{F}_+(\vec{k})$. These configuration states allow for an elegant method of keeping track of higher order dephasing.

linked to the dephasing coordinate $\vec{k}$, where gradient dephasing can be defined by evolution of these configuration states.

While this demonstrates how EPG can mathematically define gradient effects of an ensemble, we still must define RF pulse application, outside of the already mentioned 180° pulse. The mathematics of this, originally published as *partition state method*, were later referred to as phase graphing. It is the previously defined configuration states that 'extend' this original interpretation.

Phase graphing relies on utilizing the rotation matrices derived from the Bloch Equation in the complex transverse magnetization basis shown in Equations 2.36 and 2.37. This is accomplished by defining a set of similarity matrices to move between the two reference systems such that

$$\begin{pmatrix} M_x \\ M_y \\ M_z \end{pmatrix} \underset{S^{-1}}{\overset{S}{\rightleftharpoons}} \begin{bmatrix} M_+ \\ M_- \\ M_z \end{bmatrix} \tag{2.40}$$

$$S = \begin{pmatrix} 1 & +i & 0 \\ 1 & -i & 0 \\ 0 & 0 & 1 \end{pmatrix} \tag{2.41}$$

$$S^{-1} = \frac{1}{2} \begin{bmatrix} 1 & 1 & 0 \\ +i & -i & 0 \\ 0 & 0 & 2 \end{bmatrix} \tag{2.42}$$

therefore, matrices analogous to the Equations 2.30 - 2.32 rotation matrix can be defined for the complex basis using linear algebra

$$T_x(\alpha) = \begin{bmatrix} cos^2\frac{\alpha}{2} & sin^2\frac{\alpha}{2} & -isin\alpha \\ sin^2\frac{\alpha}{2} & cos^2\frac{\alpha}{2} & +isin\alpha \\ -\frac{i}{2}sin\alpha & +\frac{i}{2}sin\alpha & cos\alpha \end{bmatrix} \tag{2.43}$$

$$T_z(\theta) = \begin{bmatrix} e^{+i\theta} & 0 & 0 \\ 0 & e^{-i\theta} & 0 \\ 0 & 0 & 1 \end{bmatrix} \tag{2.44}$$

Here it is important to note that due to S not being a unitary matrix, T_x no longer possesses the properties of a rotation matrix, and instead should be thought of as a RF pulse matrix. Equations 2.43 and 2.44 can be combined to provide a more generalised RF pulse solution for any RF angle θ, rather than assuming an x-axis rotation.

$$\begin{bmatrix} M_+ \\ M_- \\ M_z \end{bmatrix}^+ = T_z(\theta)T_x(\alpha)T_z(-\theta) \begin{bmatrix} M_+ \\ M_- \\ M_z \end{bmatrix}^- \tag{2.45}$$

where - and + are used to denote the before and after magnetization. This provides precisely the same solution as Equations 2.30 - 2.32 derived from the Bloch equations, but for complex basis magnetization. Equation 2.45 is critical to EPG, as it demonstrates that applying an RF pulse to magnetization results in a superposition of 3 components of magnetization: dephasing transverse M_+, rephasing transverse M_-, and longditudinal M_z, known as Woessner decomposition, or the partitioning effect, demonstrated in Figure 2.15. This effect is responsible for the creation of stimulated echoes discussed in Figure 2.10, and provides an intuitive explanation for why lower flip angles lead to less refocusing of transverse magnetization.

If the formalism of phase graphing is combined with configuration states, we arrive at EPG, expanding configuration states to include M_z

$$\begin{aligned} \tilde{F}_+(\vec{k}) &= \int_V \Big(M_x(\vec{r}) + iM_y(\vec{r}) \Big) e^{-i\vec{k}\vec{r}} d^3r = \int_V M_+(\vec{r}) e^{-i\vec{k}\vec{r}} d^3r \\ &\iff M_x(\vec{r}) + iM_y(\vec{r}) = M_+(\vec{r}) = \int_V \tilde{F}_+(\vec{k}) e^{i\vec{k}\vec{r}} d^3k \end{aligned} \tag{2.46}$$

$$\begin{aligned} \tilde{F}_-(\vec{k}) &= \int_V \Big(M_x(\vec{r}) - iM_y(\vec{r}) \Big) e^{-i\vec{k}\vec{r}} d^3r = \int_V M_-(\vec{r}) e^{-i\vec{k}\vec{r}} d^3r \\ &\iff M_x(\vec{r}) - iM_y(\vec{r}) = M_-(\vec{r}) = \int_V \tilde{F}_-(\vec{k}) e^{i\vec{k}\vec{r}} d^3k \end{aligned} \tag{2.47}$$

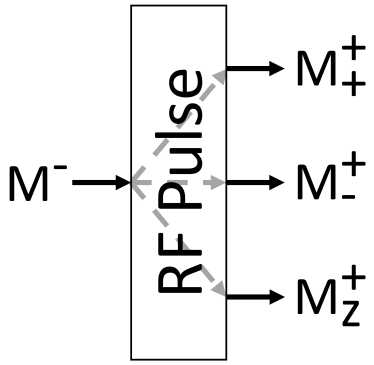

Figure 2.15: Visualization of the partitioning effect defined in Equation 2.45. An isochromat undergoing an RF pulse splits into a superposition of 3 distinct parts: dephasing transverse M_+, rephasing transverse M_-, and longditudinal M_z. This demonstrates how RF pulses refocus magnetization is imperfect, leading to potential stimulated echoes.

$$\begin{aligned} \tilde{Z}(\vec{k}) &= \int_V M_z(\vec{r}) e^{-i\vec{k}\vec{r}} d^3r \\ \iff M_z(\vec{r}) &= \int_V \tilde{Z}(\vec{k}) e^{i\vec{k}\vec{r}} d^3k \end{aligned} \tag{2.48}$$

Equations 2.46 - 2.48 define a reference system in which configuration states $\tilde{F}_+$, $\tilde{F}_-$, and $\tilde{Z}$ can be used to represent all magnetization components, defining a rotator operator algorithm which can concisely predict behaviour of isochromat ensembles while accounting for the partitioning effect. Here, $\tilde{F}_+(k)$ represents dephasing transverse magnetization similar to M_+, and can be visualised as a right-handed helix with integer k turns. Similarly, $\tilde{F}_-(-k)$ represents rephasing magnetization in the transverse plane, not unlike M_-, represented as a left-handed helix. $\tilde{Z}$ still represents longitudinal magnetization, but due to the complex nature of Fourier transformation, is now represented as a complex component, despite always being a real value. This new reference system has the following dependencies

$$\left(\tilde{F}_+(\vec{k})\right)^* = \tilde{F}_-(-\vec{k}) \tag{2.49}$$

$$\left(\tilde{Z}(\vec{k})\right)^* = \tilde{Z}(-\vec{k}) \tag{2.50}$$

These are used frequently when writing EPG simulations. Equation 2.50 ensures that the longitudinal magnetization information contained in $\tilde{Z}(\vec{k})$ is always real, and

represented by the pair of complex configuration states $\tilde{Z}(\vec{k})$ and $\tilde{Z}(-\vec{k})$ which can be visualised as two helices rotated counter to each other. Similarly to M_+, M_-, and M_z, we can express the configuration states in EPG in a way that mathematically demonstrates the effect of RF pulses on the current magnetization state.

$$\begin{bmatrix} \tilde{F}_+(\vec{k}) \\ \tilde{F}_-(-\vec{k}) \\ \tilde{Z}(\vec{k}) \end{bmatrix}^+ = \begin{bmatrix} cos^2\frac{\alpha}{2} & e^{2i\theta}sin^2\frac{\alpha}{2} & -ie^{i\theta}sin\alpha \\ e^{-2i\theta}sin^2\frac{\alpha}{2} & cos^2\frac{\alpha}{2} & ie^{-i\theta}sin\alpha \\ -\frac{i}{2}e^{-i\theta}sin\alpha & \frac{i}{2}e^{i\theta}sin\alpha & cos\alpha \end{bmatrix} \begin{bmatrix} \tilde{F}_+(\vec{k}) \\ \tilde{F}_-(-\vec{k}) \\ \tilde{Z}(\vec{k}) \end{bmatrix}^- \tag{2.51}$$

with the operator being identical to the one seen in Equation 2.43, as Fourier transformation is linear. Equations 2.46 - 2.48 and 2.51 represent the mathematical core of RF pulse calculations in EPG, and are the building blocks from which EPG simulations are created for MRF. Figure 2.16 relates how we traditionally refer to RF pulses relating to bulk magnetization to the EPG methodology, where RF pulses on isochromat ensembles exchange populations between different configuration states. For example, In EPG processes such as storage or stimulated echoes can be seen as exchanging populations between the complex configuration states of $\tilde{F}_-(-\vec{k})$ and $\tilde{Z}(\vec{k})$.

Importantly, coherent states within this formalism always have $\vec{k} = 0$. For $\tilde{Z}(0)$, this is the equilibrium magnetization that we see prior to any RF pulses being applied. The $\tilde{F}(0)$ is the state of an isochromat ensemble that is freshly excited, or an echo state. This is the most important part about using the EPG formalism: echoes only form when an $\tilde{F}(0)$ state appears. All other configuration states are fully dephased, as they have been defined as such, and therefore will not contribute to echo intensity or phase. Calculation of the magnitude and phase of the emerging $\tilde{F}(0)$ state will reveal the echoes intensity and phase respectively. Note here that we can use $\tilde{F}(0)$ without the + and - distinction between dephasing and rephasing due to Equation 2.49.

It is also worth mentioning that while configuration states can have any value of $\vec{k}$, in practice it is often sufficient to use integer values, a condition which is especially true to periodic MR sequences where EPG is most likely employed. To this end, most literature regarding regarding configuration states will use the notation $\tilde{F}_k$, $\tilde{F}^*_{-k}$, and $\tilde{Z}_k$, for $\tilde{F}_+(\vec{k})$, $\tilde{F}_-(-\vec{k})$, and $\tilde{Z}(\vec{k})$ respectively, sometimes altogether dropping the

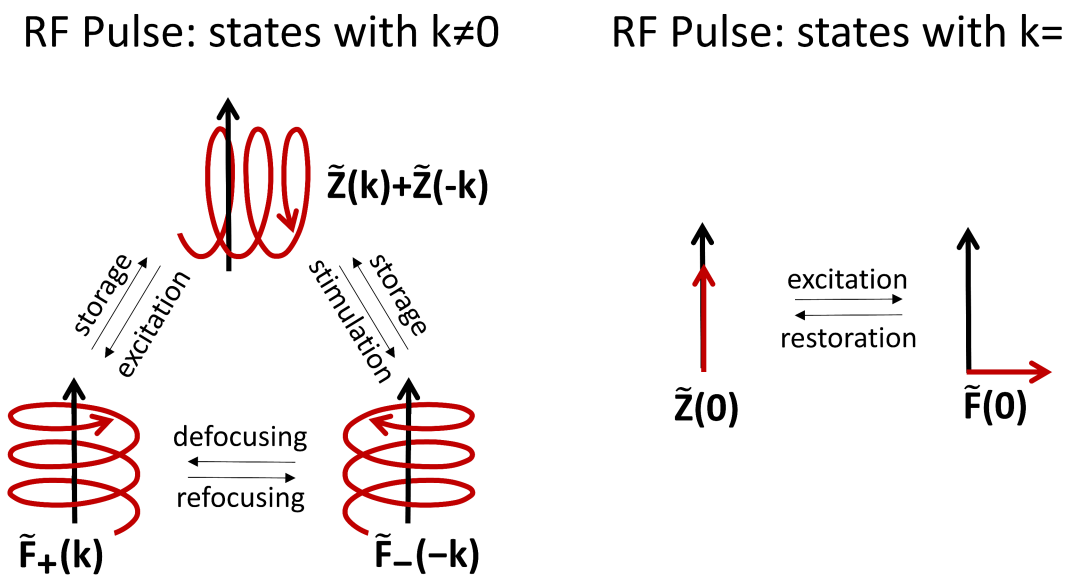

Figure 2.16: Visualization of RF pulse effect on configuration states in EPG. RF pulses calculated by the operator in Equation 2.51 redistribute population of the superposition of configuration states. This process is traditionally described using terms such as excitation or storage. Configuration states with a k value other than zero are said to be incoherent states, where the net magnetization is 0 due to configuration state representing an integer number of turns in the dephasing of the isochromat ensemble they represent. Configuration states with k=0 are coherent states, with $\tilde{Z}(0)$ representing the fully relaxed magnetization, and $\tilde{F}(0)$ representing either freshly excited magnetization, or echoes. Thus EPG is a powerful tool to find $\tilde{F}(0)$ states which we know will be echoes.

tilde notation used to highlight that $\tilde{F}$ is defined in Fourier space. For this work, we will continue to use the notation used in Equations 3.27 - 3.29 and 3.32 when referring to EPG.

With EPG now briefly defined, we can use these configuration states to define operators analogous to Equations 2.30 - 2.32 which allow for a simulation of non-balanced sequences.

$$\boldsymbol{T}(\theta,\alpha) = \begin{bmatrix} cos^2\frac{\alpha}{2} & e^{2i\theta}sin^2\frac{\alpha}{2} & -ie^{i\theta}sin\alpha \\ e^{-2i\theta}sin^2\frac{\alpha}{2} & cos^2\frac{\alpha}{2} & ie^{-i\theta}sin\alpha \\ -\frac{i}{2}e^{-i\theta}sin\alpha & \frac{i}{2}e^{i\theta}sin\alpha & cos\alpha \end{bmatrix} \tag{2.52}$$

$$\boldsymbol{E}(T_1,T_2,t) = \begin{bmatrix} exp(-t/T_2) & 0 & 0 \\ 0 & exp(-t/T_2) & 0 \\ 0 & 0 & exp(-t/T_1) \end{bmatrix} \tag{2.53}$$

$$\boldsymbol{S}(\vec{\Delta k}) : \tilde{F}(\vec{k}) \rightarrow \tilde{F}(\vec{k}+\vec{\Delta k}), \quad \tilde{Z}(\vec{k}) \rightarrow \tilde{Z}(\vec{k}) \tag{2.54}$$

Where $\boldsymbol{T}(\theta,\alpha)$ is the operator for a RF pulse of angle α from an arbitrary angle θ away from the x-axis on the x-y plane. $\boldsymbol{E}(T_1,T_2,t)$ is the relaxation operator for time interval t, and $\boldsymbol{S}(\vec{\Delta k})$ is the dephasing operator if the gradient is defined by $\vec{\Delta k} = \gamma\vec{r}\int_{t'=0}^{t}\vec{G}(t')dt'$. k = 0 configuration states requires an additional relaxation term to account for magnetization recovery towards equilibrium.

$$\begin{bmatrix} \tilde{F}_+(\vec{k}) \\ \tilde{F}_-(-\vec{k}) \\ \tilde{Z}(\vec{k}) \end{bmatrix}^+ = \boldsymbol{E}(T_1,T_2,t) \begin{bmatrix} \tilde{F}_+(\vec{k}) \\ \tilde{F}_-(-\vec{k}) \\ \tilde{Z}(\vec{k}) \end{bmatrix}^- + \begin{bmatrix} 0 \\ 0 \\ M_0(1-exp(-t/T_1)) \end{bmatrix} \tag{2.55}$$

2.2 MRI

2.2.1 K-space and Spatial Encoding

While NMR provides the basis for MRI, there are important steps required to move from the spectra to spatially resolved images. This section focuses on how we can deliberately manipulate the NMR phenomenon to provide the required spatial encoding

needed for MRI. To this end, we must introduce the concept of magnetic field gradients (G). As previously discussed, the precession frequency of spins in a magnetic field are related to the magnetic field strength. Therefore, if the field strength were to change with respect to position, the precession frequency would be dependent on physical location within the magnetic field. One of the most simple examples would be a field that varies linearly with a single dimension:

$$G_z = \frac{dB_0}{dz} \tag{2.56}$$

While this example only encompasses a single dimension, it is possible to linearly vary field strength in 3 dimensions separately. These gradients are manifested via several sets of current carrying wires within the imaging apparatus, known as gradient coils. This leads to each point in space having a different precession frequency, and therefore the amount of signal at a given frequency represents the amount of material located at a specific region. In one dimension, the signal measured can be expressed as the following integral

$$s(t) = \int_{-\infty}^{\infty} \rho(z) e^{i\omega(z)t} dz \tag{2.57}$$

where $\rho(z)$ is the density of spins, and z is the spatial location. As we are varying the magnetic field gradient linearly with z, this becomes

$$s(t) = \int_{-\infty}^{\infty} \rho(z) e^{i\gamma G_z t z} dz \tag{2.58}$$

This allows us to introduce a new quantity, k, which is defined as

$$k_z = \frac{\gamma G_z t}{2\pi} \tag{2.59}$$

and allows us to combine variables t and G_z into a single quantity which represents spatial frequency, known as k-space. As a function of k_z, the signal Equation 2.22 is written as

$$s(k) = \int_{-\infty}^{\infty} \rho(z) e^{i2\pi k_z z} dz = \mathcal{F}[\rho(z)] \tag{2.60}$$

which is to say, this variable change arranges the signal equation in a form recognizable as a Fourier transform of $\rho(z)$. Therefore, the inverse Fourier transform of the signal measured in k-space is the density function in image space.

$$\mathcal{F}^{-1}[s(k)] = \rho(z) \tag{2.61}$$

This can be extended to 3D with the more general definition of $\vec{k}$ as

$$\vec{k} = \frac{\gamma \vec{G} t}{2\pi} \tag{2.62}$$

and $\rho(\vec{r})$ as

$$\rho(\vec{r}) = \int_{-\infty}^{\infty} s(\vec{k}) e^{-i2\pi \vec{k} \cdot \vec{r}} d\vec{k} \tag{2.63}$$

A summary of the relationship between the different domains of MRI are visualised in Figure 2.17.

Magnetic field gradients are typically applied in three very specific ways to give us three different dimensions of separability, which will be discussed in to next few sections.

2.2.2 Slice Select Gradients

The first way in which field gradients are used are slice select gradients. Unsurprisingly, this allows for excitation of a selected slice of the material being imaged. This is performed by using a shaped RF pulse, which excites frequencies over a specific bandwidth (BW), during an applied gradient. This RF pulse is typically sinc shaped, as the Fourier transform of an RF pulse defines its frequency response, and the Fourier transform of a sinc function is rectangular, allowing for a uniform excitation response between the boundaries of the area of interest.

The frequency of spins parallel to a gradient have a variance in frequency according to

$$f(z) = f_0 + \frac{\gamma}{2\pi} G_z z \tag{2.64}$$

By varying the strength of the gradient, and the frequency and duration of the RF pulse, we are able to selectively control the slice being excited, as shown in Figure

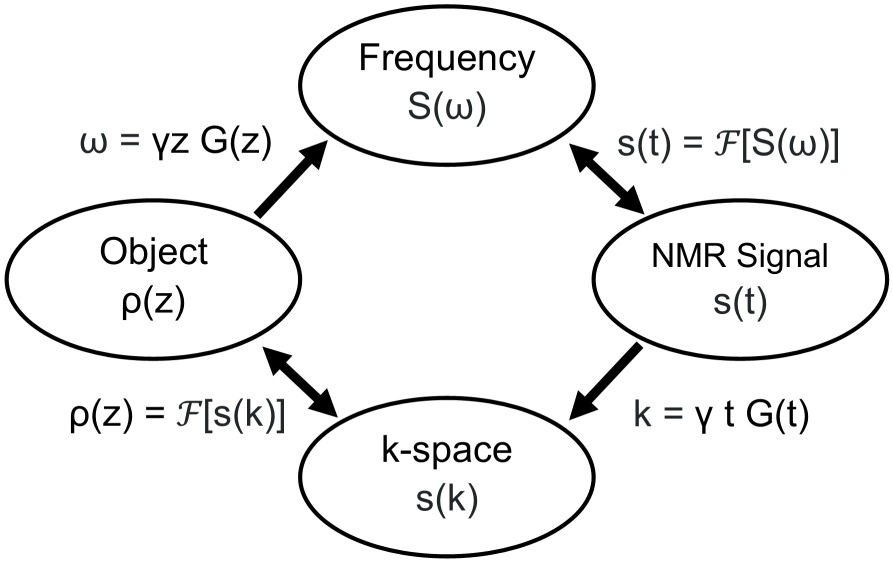

Figure 2.17: Relationship between the domains relevant to MRI. A spatially dependent magnetic gradient creates a Larmor frequency which also varies in space. This can be measured as an NMR signal, which when inverse Fourier transformed gives a spatially resolved image of the object.

2.18.

$$\Delta z = \frac{2\pi BW}{\gamma G_z} \tag{2.65}$$

It is important to note that a slice select gradient must be accompanied with a secondary component to reverse the decoherence effects on the spins during the application of said gradient. This is typically a gradient in the opposite direction with equivalent amplitude applied for half of the time the slice select gradient was, applied post slice selection.

2.2.3 Frequency Encoding

Secondly, we have frequency encoding. This refers to applying a magnetic field gradient *during* collection of the FID. As previously seen, the application of a gradient causes spins to precess at different frequencies dependent on position. Therefore, acquisition of an FID which a gradient is applied will not collect a single point of data, but instead a line of data.

This is easiest to visualize by thinking of gradients as moving the position of

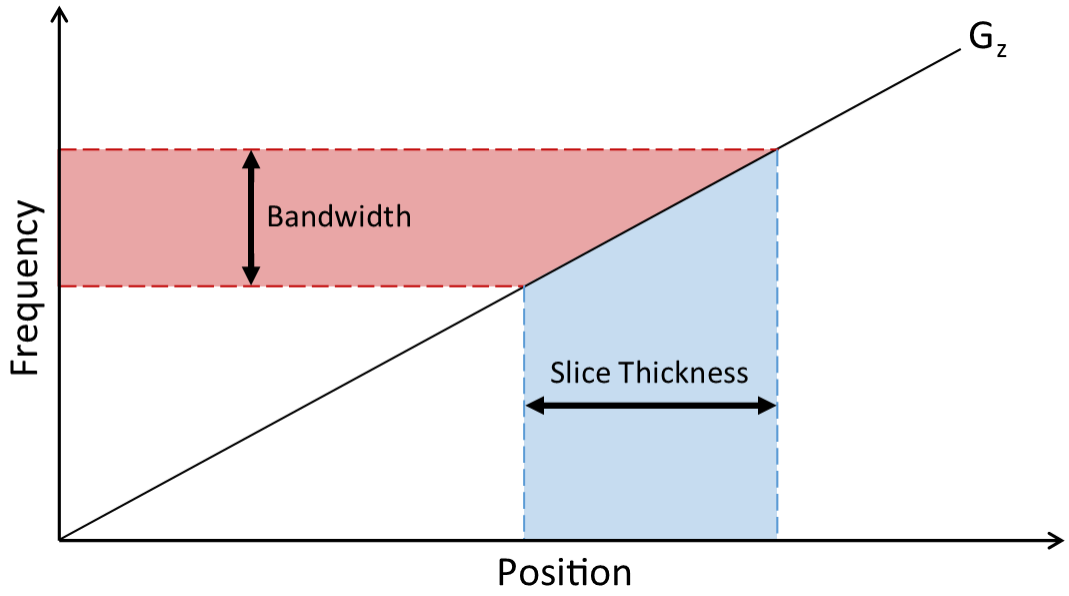

Figure 2.18: Application of a shaped RF pulse during gradient application allows for selective slice excitation. By changing the duration and frequency of the pulse, the slice thickness can be altered.

collected data within k-space, such that

$$\Delta k_x = \frac{\gamma}{2\pi} G_x t_x \tag{2.66}$$

where t_x is the time a gradient has been applied for. Therefore, the application of a gradient during acquisition can be seen as 'sweeping' through k-space, allowing the collection of single line of data. Thus this gradient is often known as a readout gradient.

Similarly to a slice select gradient, it is often necessary to apply additional gradients both before and after the readout gradient, as to either prepare or restore the phase coherence of the sample after acquisition. While a preparation gradient is common in Cartesian MRI data collection (i.e. data is collected in straight lines in k-space), modifications to sequences can include additional gradients. One such example is a rewinder gradient seen in a bSSFP sequence, an additional gradient added after the readout gradient to balance the net gradient area of a sequence, effectively recentering the measured position in k-space after an acquisition window.

While the movement through k-space can be considered continuous throughout the acquisition t_{acq}, the collection of data is divided discretely in time, known as

the dwell time Δt_d, so that the total number of data points acquired is defined as $N = t_{acq}/\Delta t_d$. Thus the FOV in the readout gradient direction can be defined as

$$FOV_x = \frac{1}{\Delta t_d G_x} = \frac{N}{t_{acq} G_x} \tag{2.67}$$

An important consideration is that the FOV must be larger than the size of the object being imaged, else wrapping artefacts will occur.

2.2.4 Phase Encoding

Finally, we have phase encoding gradients. These are gradients which are applied prior to the acquisition of data. If frequency encoding can be thought of as moving through a line of k-space during acquisition, then phase encoding shifts the position of that line prior to readout.

This is achieved via the introduction of a gradient perpendicular to the readout gradient and slice select gradient

$$\Delta k_y = \frac{\gamma}{2\pi} G_y t_y \tag{2.68}$$

However, unlike the readout gradient, the phase encode gradient is only on for a fixed amount of time τ_{PE}. This leads to an ensemble where at the end of the gradient application all spins share an equivalent frequency, but the phase is spatially dependent.

$$\phi = \gamma G_y \tau_{PE} y \tag{2.69}$$

Unlike frequency encoding, phase encoding is performed in discrete steps, with the number of step defined as

$$N = 2\frac{|G_y^{max}|}{\Delta G_y} \tag{2.70}$$

where G_y^{max} is the maximum gradient amplitude, and ΔG_y is the gradient step size. Thus, the FOV in the phase encode direction can be defined as

$$FOV_y = \frac{1}{\tau_{PE} \Delta G_y} = \frac{N/2}{\tau_{PE} |G_y^{max}|} \tag{2.71}$$

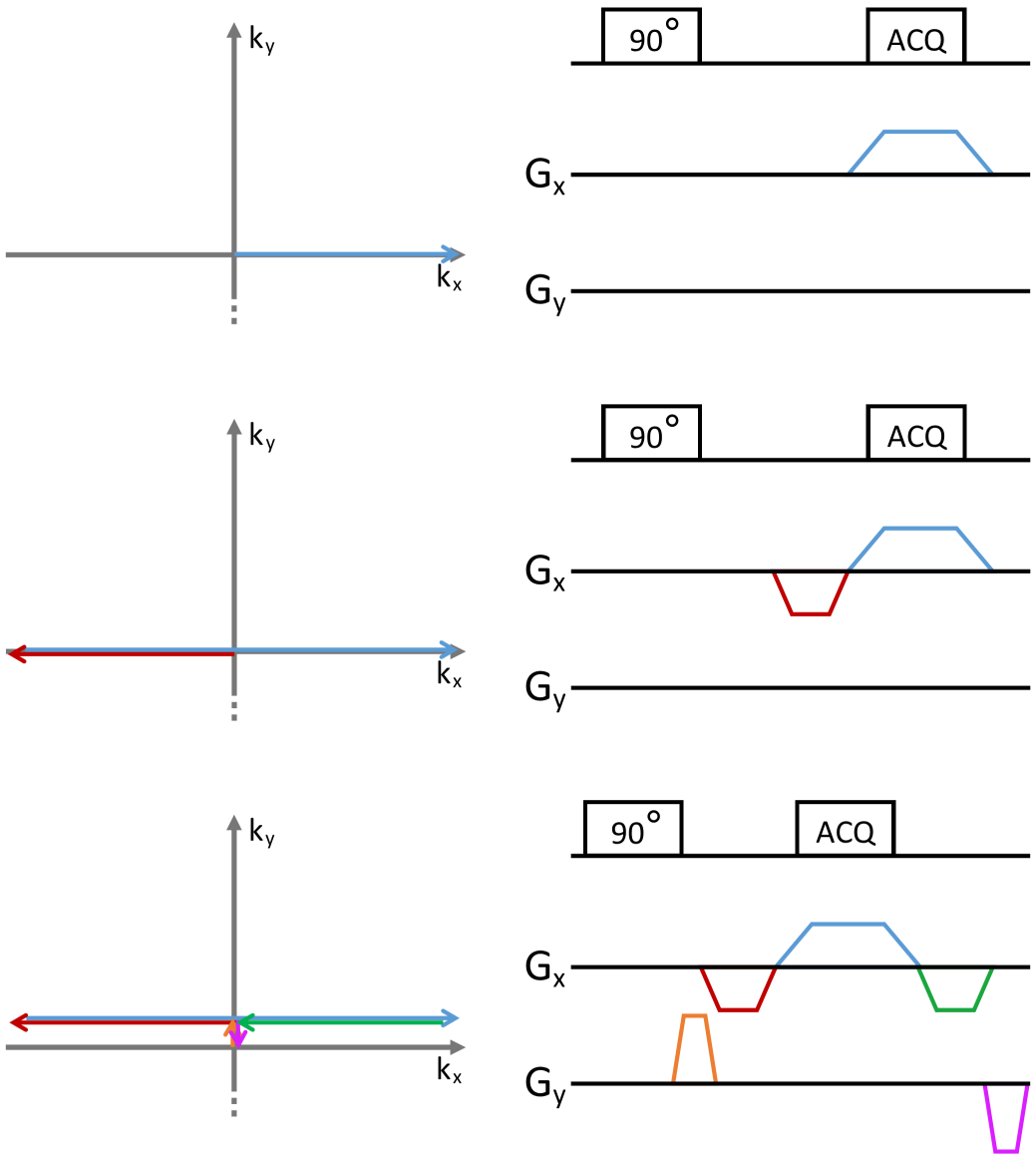

Figure 2.19: Visualization of k-space trajectories using frequency and phase encoding. (top) Via the application of a gradient during the acquisition window, known as a frequency encode or readout gradient, the acquisition occurs along a line of k-space (blue). (middle) In practice, it is often better to collect longer lines of k-space at once, and so prior to a readout gradient, a secondary lobe of opposite magnitude equal to half of the gradient area allows for the acquisition to begin at the edge of k-space (red). (bottom) Introducing another gradient channel orthogonal to the readout, a gradient prior to readout can alter the k_y coordinate of the readout line (orange). Some sequences also require the use of rewinder gradients to re-center the k-space acquisition point, reverting the phase and frequency encoding by balancing out the gradient areas in every channel (green, purple)

A visualization of frequency and phase encoding as it pertains to moving through k-space can bee seen in Figure 2.19.

2.2.5 MRI Pulse Sequences

Similar to NMR, acquisition of data in MRI is performed by a discrete series of manipulations, referred to as a pulse sequence. These include the previously mentioned RF excitation trains which give rise to specific types of echoes and magnetization recoveries, but with the added complexity of localized acquisition over a 3D space. This sections purpose is to briefly cover MRI pulse sequence diagrams, as well as the nomenclature used when discussing the specification of an MRI sequence.

An example of a gradient echo pulse sequence diagram is shown in Figure 2.20. This shows execution of the various components of a sequence along a time axis, running from left to right. While the time axis will span the entirety of the sequence of interest, only a single repetition time (TR) is visualized, referring to a single application of the readout gradient. This is signified by the phase encoding gradient channel showing multiple gradient strengths at a single time point, as this is often the only change with each successive TR. Additional features may accompany the TR section of the sequence, such as a preceding magnetization preparation module. RF pulses are often labelled with their corresponding flip angle and Cartesian axis (e.g. 30_x), shorthand for the nominal angle which the $\vec{B_1}$ field will drive the bulk magnetization vector about said axis. While sometimes omitted, the echo time TE may also be present on the pulse sequence diagram, denoting the time between an RF excitation and the resulting FID.

2.2.6 Non-Cartesian Trajectories

Up until this point is has been assumed that data collection is Cartesian, i.e. that singular straight lines of k-space are collected once per TR, but this is an inefficient method due to how data is stored within k-space. The centre of k-space contains low-frequency spatial information responsible for image contrast, while the peripheral regions contain high spatial frequencies responsible for sharp edges and fine detail. Either one of these areas can be undersampled, leading to artefacts specific to the region chosen. If the centre of k-space is undersampled, resulting images will suffer

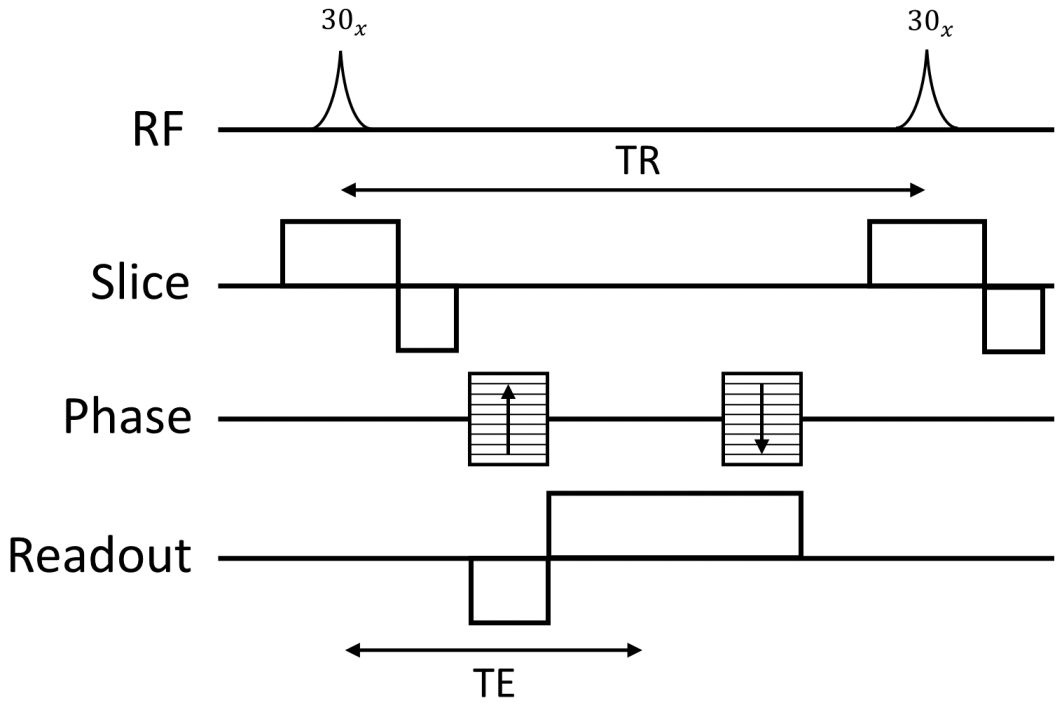

Figure 2.20: Visualization of a gradient echo pulse sequence diagram. Typically showing a single TR, these diagrams show the gradient timing for each individual channel required to generate an image.

from loss of the overall contrast of the image, while undersampling of the periphery can lead to less sharp edges, but is in general much more robust to undersampling.

It is for this reason that k-space trajectories often seek to maximize central k-space data collection while choosing to undersample high frequency information. An example of the effects of undersampling is shown in Figure 2.21.

One of the first attempts to optimize k-space trajectories was to rotate the acquisition lines to form a radial pattern. This is traditionally performed from the centre of k-space, however it is also possible for radial acquisitions to to be performed from one side of k-space to the other through the centre, similarly to back projections in CT. The equation for a radial trajectory in k-space is given by

$$r(t) = kxcos(\omega t) + kysin(\omega t) \tag{2.72}$$

where r(t) is the position of the trajectory at time t, kx and ky are the x and y components of the wave vector, and ω is the angular frequency. One of the additional benefits of radial MRI besides a higher sampling of the centre of k-space is that by uncoupling the frequency and phase encode from specific directions, frequency and phase specific artefacts do not propagate along a single axis. Additionally, the oversampling of the centre of k-space at regular intervals can be exploited to detect and correct motion. While radial MRI was supplanted as an acceleration technique by spin-warp imaging, radial artefact suppression is still used today for imaging specimens with periodic motion, such as in cardiac imaging.

Traditionally, as radial MRI is not a Cartesian technique, raw data collected from k-space is not in an appropriate state for use of efficient Fast Fourier Transform (FFT) algorithms. To overcome this, data must be 'regridded', an iterative process in which the data is morphed onto a Cartesian coordinate system. This has become less of an issue with both the development of the non-uniform Fourier transform (NUFFT)/radial Fourier transforms, and computational power drastically improving since the 1980's, allowing for iterative regridding processes to be completed in seconds.

Another non-Cartesian trajectory, and one more pertinent to this work, are the use of spiral waveforms. There are two main types of spiral trajectories that can be used: Archimedean and variable density.

Archimedean spirals have a constant separation between the turns of the spiral.

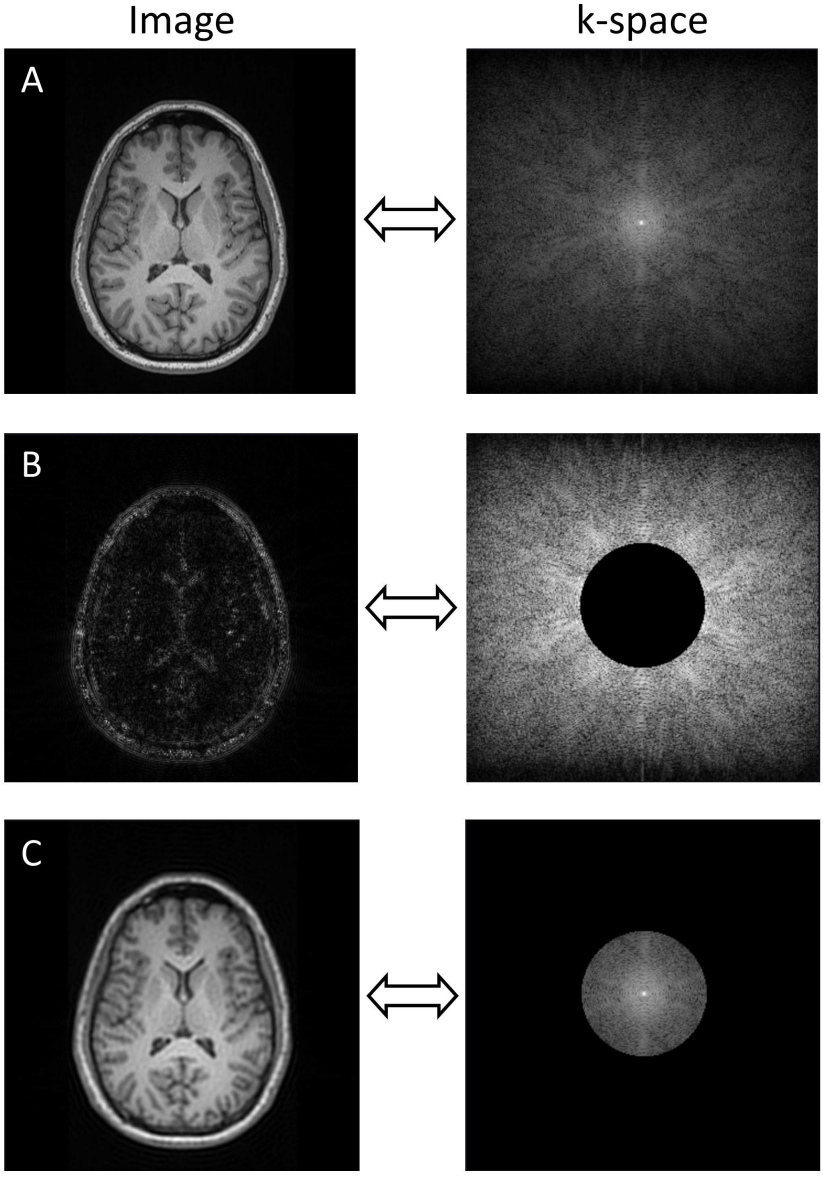

Figure 2.21: Demonstration of the importance of the centre of k-space. A) Fully sampled reconstruction of k-space, where the collection of all data results in a high quality image with no visible artefacts. B) By removing the inner 25% of k-space, we see the the image is completely destroyed, showing the importance of the lower frequencies of k-space for most of the information within the image. The remaining high frequency data remains, and so does information regarding the the edges of the image. C) When we reverse the process and remove 75% of the high frequency data, the image remains intact, while blurred. Thus when choosing to undersample a trajectory, it is critical to prioritize the central, low frequency k-space.

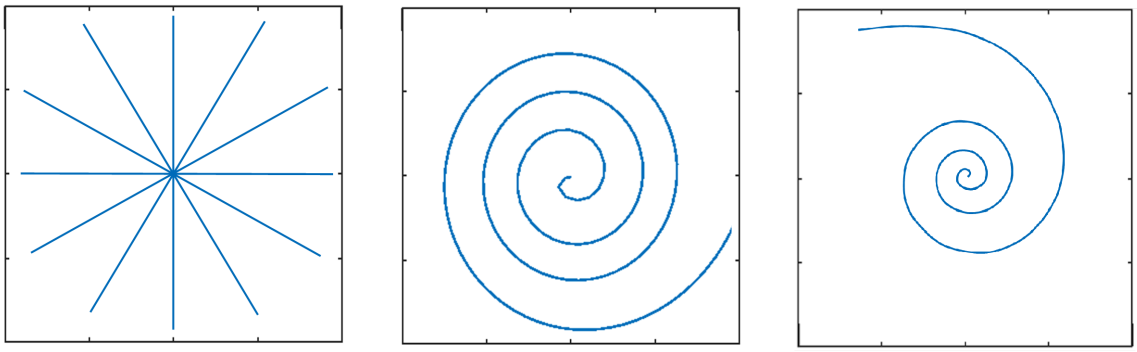

Figure 2.22: Example of three of the non-Cartesian trajectories commonly used in MRI. (Left) Radial trajectory maximises the collection of central k-space by successive rotation of a readout throughout the centre of k-space. (Middle) Spiral trajectory uses sinusoidal gradient waveforms to rotate at in increasing distance from the central point. (Right) Variable density spiral trajectory, focusing acquisition on the central region of k-space.

This means that the spacing between each point in k-space is constant, which makes the reconstruction process simpler. However, the constant spacing can also lead to uneven sampling of k-space, which can result in spiral specific artefacts and reduced image quality.

Variable density spirals, on the other hand, have a non-uniform spacing between the turns of the spiral. This means that the spacing between each point in k-space is varied, which can improve the overall sampling of k-space and reduce image artefacts. However, the non-uniform spacing can make the reconstruction process more difficult, which can increase reconstruction times and computational requirements, but are not often an issue with the processing power of modern computers.

Both Archimedean and variable density spirals have their advantages and disadvantages. In general, Archimedean spirals are better suited for fast imaging applications, such as functional MRI or real-time imaging, while variable density spirals are better suited for high-resolution imaging, imaging of complex anatomies, or highly undersampled datasets.

We begin with defining an Archemidean spiral mathematically, where $\vec{k}$ will be trace a uniformly spaced spiral in k-space. The x and y components of $\vec{k}$ are as follows

$$k_x = \mid \vec{k} \mid cos\theta \tag{2.73}$$

$$k_y = \mid \vec{k} \mid sin\theta \tag{2.74}$$

with θ is defined as

$$\theta = \frac{2\pi n}{t} f(t) \tag{2.75}$$

where n is the matrix size, f(t) is the frequency, and t is time. To create an Archemidean spiral, $\vec{k}$ must follow

$$\mid \vec{k} \mid = \frac{\theta}{2\pi FOV} \tag{2.76}$$

Noting that $\vec{k}$ and $\vec{G}$ are related by the following equation

$$\vec{k} = \frac{2\pi}{\gamma} \int_0^t \vec{G}(t')dt' \tag{2.77}$$

the gradients required to trace an Archemidean can be solved, leading to the following equations

$$G_x = \frac{\dot{\theta}}{\gamma FOV}[cos\theta - \theta sin\theta] \tag{2.78}$$

$$G_y = \frac{\dot{\theta}}{\gamma FOV}[sin\theta + \theta cos\theta] \tag{2.79}$$

The limiting factor for the shape and speed of a spiral trajectory is G_{max}, the maximal amplitude capable by the system, and the rate of change of G_{max}, referred to as the slew rate. The slew rate is the limiting factor while imaging the centre of k-space, while the maximal amplitude is the limiting factor in the periphery. Thus the gradient waveforms are often both slew and amplitude limited to remain within the limits of the gradient amplifiers.

Variable density spiral gradient waveforms can be defined similarly, but often include an exponential term to scale the distance between successive rotations in k-space. A generalized variable density spiral waveform containing both slew and amplitude limiting can be written

$$G_x(t) = G_{max} cos\theta cos(2\pi\alpha t) exp(-\beta t^2) \tag{2.80}$$

$$G_y(t) = G_{max} sin\theta cos(2\pi\alpha t) exp(-\beta t^2) \tag{2.81}$$

where α is the gradient slew rate, and β is the rate of change of the gradient amplitude with time.

Spiral trajectories require the same regridding techniques used for radial acquisition, while having its own unique complications. Spiral trajectories are more sensitive to motion artefacts as they sample less evenly throughout k-space, as well as increased sensitivity to field inhomogeneities. However, when compared to radial trajectories, a spirals longer single readout leads to a faster data collection as well as higher spatial resolution. Variable density spiral also offers the ability to 'tune' the rate of undersampling in the lower/higher spatial frequencies by adjusting the density function, leading to more customization for the specific application.

2.3 MRI Contrast Agents

Contrast agents have been a core part of MRI since the 1980s, with gadopentetate dimeglumine, marketed as Magnevist, becoming the first contrast agent clinically approved by the U.S. Food and Drug administration in 1988 [104]. Today, a myriad of contrast agents are available for use in MRI. Contrast agents intentionally modulate the magnetic properties of the protons being measured by MRI, with how and where that modulation occurs being down to the chosen contrast agent. While care must be taken for the biological safety of the patient via choice of contrast agents which are non-toxic, contrast enhanced MRI has been shown to greatly enhance the capabilities of MRI.

For MR images, the contrast which is seen is dependent on the aforementioned relaxation values, T_1, T_2, and T_2^*, as well as proton density, all of which can be highlighted by performing sequences which highlight the contrast of interest. While some illnesses of interest may display differences in one of these relaxation values between healthy and pathological tissue, there are many conditions which do not lead to a morphological change, where the introduction of a contrast agent may elucidate the physiological difference.

MR contrast agents are typically defined by their relaxivites r_1 and r_2, or the strength at which they will affect the relaxation values of surrounding tissue, expressed in $mM^{-1}s^{-1}$. Mathematically, these can be represented as

$$R_{1,obs} = R_{1,tissue} + r_1 \cdot [A] \tag{2.82}$$

$$R_{2,obs} = R_{2,tissue} + r_2 \cdot [A] \tag{2.83}$$

$$R^*_{2,obs} = R^*_{2,tissue} + r^*_2 \cdot [A] \tag{2.84}$$

where $R_{1,tissue}$, $R_{2,tissue}$, and $R^*_{2,tissue}$ are the intrinsic relaxations of the tissue with no added contrast agent, $R_{1,obs}$, $R_{2,obs}$ and $R^*_{2,obs}$ are the measured relaxations of the tissue in the presence of the contrast agent, and [A] is the concentration of the contrast agent.

The ratio between r_1 and r_2 often determine whether the agent is defined as a T_1 or T_2 weighted agent, with T_1-weighted agents typically having a high $\frac{r_1}{r_2}$ value. Other types of contrast agents exist, such as chemical exchange saturation transfer (CEST) agents, reduce the water proton signal through a chemical exchange site. These will not be discussed in detail in this work.

Initial contrast agents were designed with this goal; through an intravenous bolus injection, reach the site of interest and improve contrast to the tissue of interest. These non-specific contrast agents still see use in areas such as MR angiography, and via *in vitro* labelling, can even enable MR cellular imaging.

2.3.1 T_1 Contrast Agents

T_1 contrast agents create a dipole-dipole interaction between the agent and the surrounding protons, which is described in the Solomon-Bloembergen-Morgen theory [105]. Qualitatively, the agents local magnetic field provides a relaxation pathway for the surrounding protons. The specific characteristics of this interaction can be defined by the parameters exchange correlation time τ_m, rotational correlation time τ_r, and diffusion correlation time τ_d.

The exchange correlation time τ_m refers to the time scale on which the contrast agent's magnetic properties fluctuate. When the exchange correlation time is long,

the paramagnetic ions in the contrast agent interact with water molecules in the surrounding tissue for a longer duration, which leads to a greater effect on the relaxation times and, therefore, stronger contrast. The exchange correlation time is dependent on the size and shape of the contrast agent, as well as the nature of the paramagnetic ions used. The rotational correlation time τ_r refers to the time scale on which the contrast agent undergoes rotational motion around its axis. When the rotational correlation time is long, the contrast agent rotates slowly, resulting in a more prolonged interaction with water molecules in the surrounding tissue. This prolonged interaction leads to a greater relaxation effect, which translates to stronger contrast in the image. The diffusion correlation time τ_d refers to the time scale on which the contrast agent undergoes translational motion within the tissue. When the diffusion correlation time is long, the contrast agent moves slowly, resulting in a more prolonged interaction with water molecules in the surrounding tissue. This prolonged interaction leads to a greater relaxation effect, leading to stronger contrast in the image. Diffusion correlation time is particularly important in diffusion-weighted MRI, which measures the diffusion of water molecules in the tissue. Contrast agents that have a long diffusion correlation time can interfere with the diffusion measurements and can lead to errors in the interpretation of the diffusion data. τ_m, τ_r, τ_d are all tied to the contrast agent being used, with small ions tending to rotate and diffuse faster, leading to shorter diffusion correlation times and weaker contrast. Thus creating new contrast agents with desirable τ_m, τ_r, τ_d values is an active field of study.

For T_1, Gd based contrast agents are still the most commonly used clinical contrast agent used with ^{1}H radiofrequency coils [106]. Structurally, Gd^{+3} ions are either attached to elongated molecular ligands which wrap around them, or trapped in the cavity of a cage-like structure, referred to as linear or macrocyclic agents respectively [107]. Over 30% of all clinical MRI scans utilize Gd contrast agents, increasing lesion detection and improving disease characterization for a variety of pathologies [108].

2.3.2 T_2/T_2^* Contrast Agents

T_2 and T_2^* agents can affect nearby relaxation values via the same paramagnetic contribution, but T_2 and T_2^* agents also produce superparamagnetic relaxation on a scale which typically contributes the majority of the transverse relaxation. Of

particular interest to this work are superparamagnetic contrast agents constructed of iron oxide nanoparticles, known as SPIO.

When ferromagnetic material particles are sufficiently small, typically less than 100 nm, the magnetization can be approximated as a single magnetic moment. At this size, the energy required for magnetization reversal is close to the thermal energy at room temperature, so the magnetic moment will randomly flip direction with no external field applied. If the time between direction change, known as the Neel relaxation time, is less than the measurement time for the magnetization, then the net moment is zero due to the fluctuation, and these nanoparticles are said to be super paramagnetic.

Super paramagnetic materials behave much like paramagnetic ones, but with much higher magnetic susceptibility. Paramagnetic behaviour in super paramagnetic nanoparticles occurs below the Curie temperature, while in most ferromagnetic materials this paramagnetic behaviour occurs above the Curie temperature. Super paramagnetic materials also exhibit no hysteresis effect when responding to a magnetic field. This is directly related to the size of the particles, and so it is possible to define a critical size in which super paramagnetism is reached for magnetic materials. The coercivity, or the ability to not become demagnetized in a magnetic field, of super paramagnetic materials is 0.

SPIO are commercially available and composed of biodegradable iron oxide crystals typically coated in dextran. These are specified by the size of the particle; 10-50 nm particles are referred to as ultra-small super paramagnetic iron oxide (USPIO), or sometimes monocrystalline iron oxide nanoparticles (MION) if a single iron oxide crystal is at the core. 'Standard' SPIO particles are defined as having a diameter of 50-100 nm, and above 300 nm they are typically referred to as microparticles of iron oxide (MPIO). SPIO is easily detectable via electron microscope [109], has been generally shown to not alter cell behaviour and dynamics [110, 111], is biocompatible, non-toxic and, beneficially for cellular imaging, the T_2/T_2^* ratio for SPIO changes when compartmentalized.

SPIO contrast agents affect the transverse relaxation, stemming from the magnetic susceptibility difference between the SPIO and the surrounding tissues, causing a loss of phase coherence. The resulting signal is seen as a void in conventional T_2 weighted

imaging.

Chapter 3

Implementing MRF

3.1 Introduction

MRF's high robustness to undersampling and novel acquisition method provide a promising foundation for multi-parameter mapping, with a scan time greatly outperforming conventional quantitative methods. Due to this, MRF has become an actively researched area of MR, with over 700 dedicated publications in the last decade. MRF is easy to conceptualize and understand, highly adaptable to a specific requirement, and the verbose nature of its post-processing pipeline leaves much room for optimization.

The core concept of MRF that differs from other imaging methodologies is the generation of unique signal evolutions for different tissue properties. While this is similar to the idea behind relaxometry, where multiple time points are collected throughout an ensemble's return to equilibrium, MRF operates in a way which the resulting signal is indicative of more than one relaxation time.

Thus, the fundamentals of MRF are concerned with how to generate these unique signals for each tissue type, and how to distinguish the resulting signals to decipher the corresponding parameters. Research in MRF broadly falls into two categories: providing sensitivity to a new tissue property, or improving the constraints to the methodology, typically speed. This chapter covers the initial implementation of MRF with T_1 and T_2 sensitivity on a preclinical system.

3.1.1 Signal Acquisition

The sequence MRF is based on is somewhat arbitrary, provided it is sensitized to the tissue properties of interest; originally these were T_1 and T_2, which both continue to be included in most implementations. MRF was originally designed for bSSFP sequences, and most implementations continue to use either balanced or non-balanced

SSFP.

SSFP is a gradient recalled echo sequence where successive excitation pulses are phase coherent, TR is approximately equal to or less than T_2, and the resulting phase accumulated steady state is not spoiled. These conditions are met if the gradient area does not change between successive TR windows, and successive excitation pulses contains the same phase (or alternate with each application). BSSFP is a special instance of SSFP, with the additional requirement that the net gradient area between successive instances of TR is zero.

If these conditions are met, a steady state of longitudinal and transverse magnetization will be achieved, containing two transverse parts. The first is a FID-like signal which decays after each applied excitation, and the second is an echo formed just prior to the next excitation. The strength of these components can be calculated with the following expressions, with the full derivation being provided by Freeman and Hill in 1971 [112]

$$SSFP_{FID} = M_0 tan\left(\frac{\alpha}{2}\right)\left(1 - \frac{(E_1 - cos\alpha)(1 - E_2^2)}{\sqrt{p^2 - q^2}}\right) \tag{3.1}$$

$$SSFP_{echo} = M_0 tan\left(\frac{\alpha}{2}\right)\left(1 - \frac{(1 - E_1 cos\alpha)(1 - E_2^2)}{\sqrt{p^2 - q^2}}\right) \tag{3.2}$$

where

$$E_1 = e^{-TR/T_1} \quad E_2 = e^{-TR/T_2}$$
$$p = 1 - E_1 cos\alpha - E_2^2(E_1 - cos\alpha)$$
$$q = E_2(1 - E_1)(1 - cos\alpha)$$

that is, SSFP sequences have a weighting which is both T_1 and T_2 dependent, ideal for MRF.

Despite being a GRE sequence, SSFP's two-component signal has some properties that differ from conventional GRE, primarily contrast behaviour in the resulting images. GRE sequences typically produce a predominantly T_1 weighted image, where SSFP will image fluid more brightly and provide less overall contrast. This is due to spoiled GRE removing the long T_2 signal each TR, where the SSFP-echo component

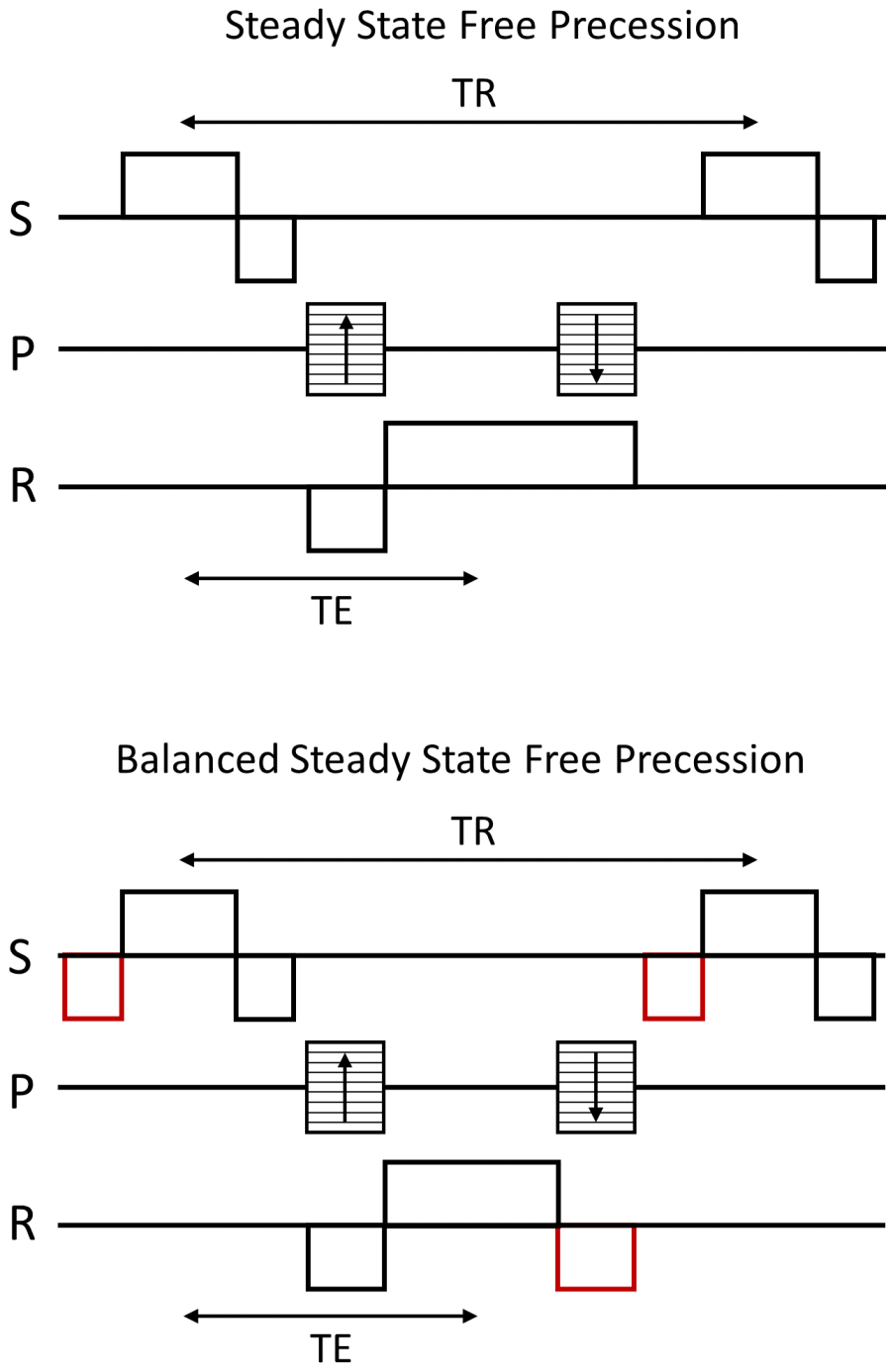

Figure 3.1: SSFP and bSSFP pulse sequences. Gradient channels are slice select, phase, and readout respectively. bSSFP sequences must precede gradients with a 'dewinder' gradient, so that the resulting net gradient for each channel is zero (bottom)

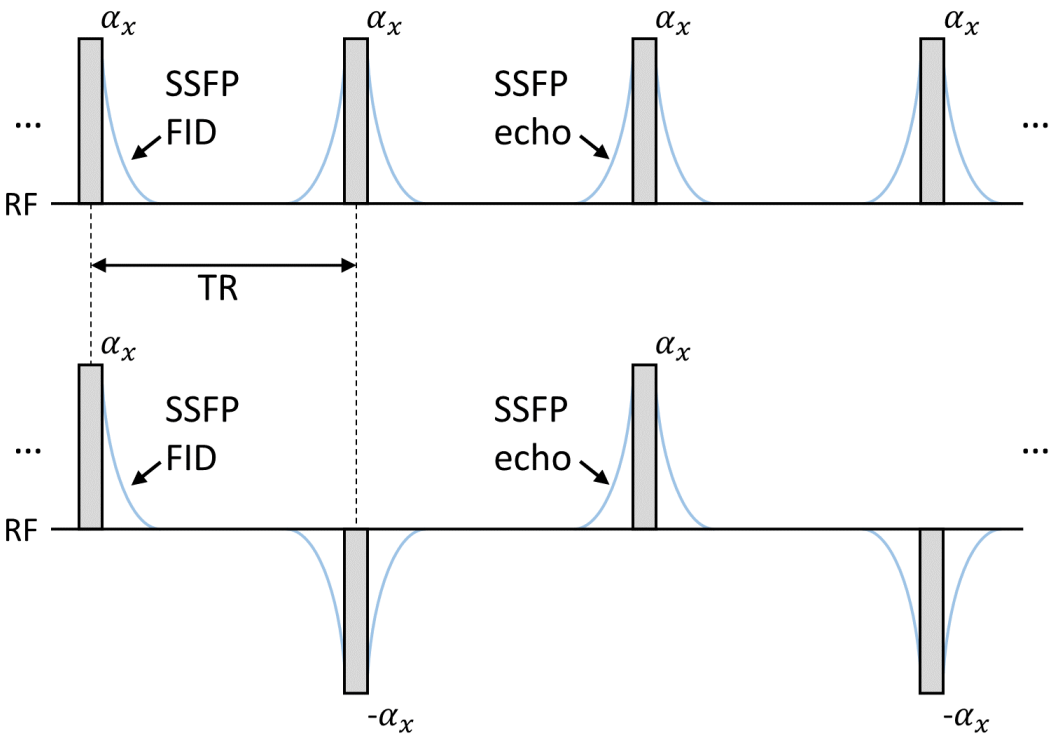

Figure 3.2: SSFP FID and echo components. SSFP's traverse magnetization is made up of two components, a FID-like decay after an excitation is applied, and an echo forming prior to the next excitation (top). An anti-parallel phase coherence of the RF pulses leads to a slightly different transverse magnetization profile, where successive signal is sign-alternated with each TR.

will preserve the longer relaxation times. This also means the SSFP has a much higher SNR than traditional GRE sequences.

If the conditions for bSSFP are met, the FID and echo peaks will converge at the same TE. The resulting signal is dependent on the whether the sign of the RF pulse is alternated for each TR or not

$$bSSFP_{alt} = M_0 sin\alpha \frac{1 - E_1}{1 - (E_1 - E_2)cos\alpha - E_1 E_2} e^{-TE/T_2} \tag{3.3}$$

$$bSSFP_{noalt} = M_0 sin\alpha \frac{1 - E_1}{1 - (E_1 + E_2)cos\alpha + E_1 E_2} e^{-TE/T_2} \tag{3.4}$$

with sign alteration leading to a greater signal, it is often the preferred method for bSSFP. When compared to bSSFP, SSFP offers less SNR due to not coalescing the FID and echo components of the steady state. Unfortunately, the phase dependent nature of the resulting signal for bSSFP is highly susceptible to signal loss via accrual of phase shifts, as is often the case in MRI. This generates banding artefacts which need to be accounted for in the dictionary of an MRF sequence, adding an additional dimension. Therefore, bSSFP for MRF can provide higher SNR, with the trade-off of greater post processing time and dictionary size.

To create an MRF sequence, traditional sequences must be modified to intentionally and temporarily disturb the steady state, producing a signal indicative of the imaged tissue. This is achieved by modulation of sequence parameters, providing flexibility of design so long as the resulting variation is sensitive to the tissue of interest, while preserving sufficient SNR. MRF traditionally varies both the repetition time, and the flip angle of the sequence to achieve a T_1 and T_2 sensitivity, although there are many examples of additional variations to sensitize to a novel tissue parameter.

3.1.2 The MRF Dictionary

The signal acquired from an MRF sequence is meaningless until paired with a simulation database. Referred to as a dictionary, these are constructed using the known parameter variation of a sequence, and a model for spin behaviour and signal evolution. The resulting dictionary dimensions are dependent on the number of imaging frames of the corresponding sequence, and the number of properties the dictionary is modelling.

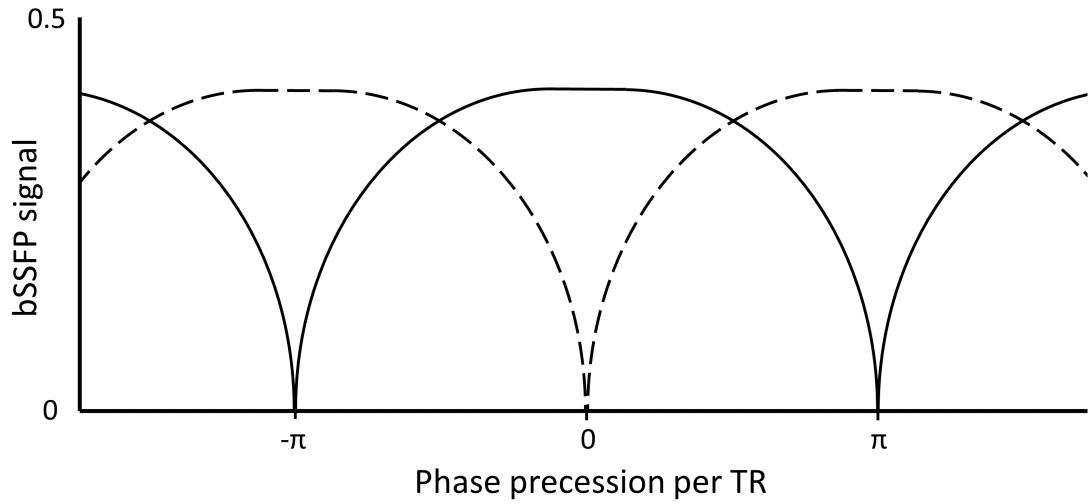

Figure 3.3: Representation of bSSFP signal vs the phase accrual for successive TRs. Cycling the phase of the RF excitation pulse by π radians each TR results in strong on-resonance signal (solid line), with a band occurring at $\pm\pi$. Not cycling the phase (dashed line) results in an on-resonance band, with maximum signal occurring at $\pm\pi$. Either method is therefore highly susceptible to banding artefacts, as unintentional phase accrual is common in MR sequences.

Regardless of the method used to generate the dictionary, the signal from each voxel must be paired with its best matching dictionary counterpart, allowing for assignment of parameter values for said voxel. Matching relies on finding the highest vector-dot product of the voxel signal and a dictionary entry, a process which scales temporally with dictionary size. With a single *in vivo* study imaging multiple mice at multiple time-points, dictionary matching processing times can quickly scale uncontrollably. For this reason, fast dictionary matching has been a focus of MRF research.

Several options exist[88], but one with universal application for MRF is singular value decomposition (SVD). MRF signals and the dictionary entries are sparse, and SVD provides a method in which to greatly compress the meaningful information of such datasets, leading to vastly improved post processing times for MRF.

SVD relies on a simple principle: expressing a sparse dataset in a configuration which allows for utilization of a low rank approximation, containing sufficient data necessary to accurately represent the original dataset concisely. This is performed by expressing the original dataset as a product of three matrices in the following way

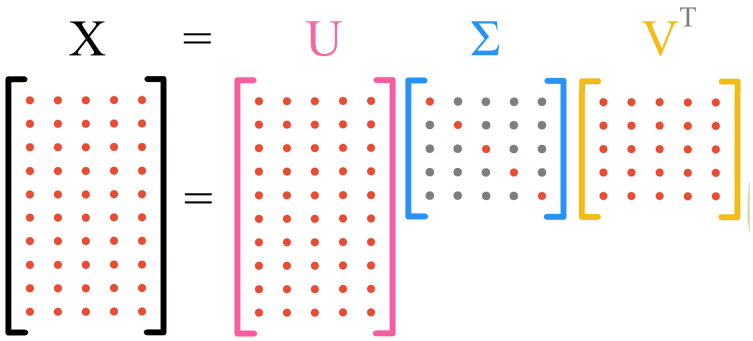

Figure 3.4: Visual demonstration of how any dataset can be represented as the product of three matrices, with the middle matrix containing only diagonal values of descending size.

$$\boldsymbol{X} = \boldsymbol{U}\boldsymbol{\Sigma}\boldsymbol{V}^T \tag{3.5}$$

where $\boldsymbol{U}$ is an m x m orthogonal matrix, $\boldsymbol{V}$ is an n x n orthogonal matrix, and $\boldsymbol{\Sigma}$ is an m x n diagonal matrix of increasingly vanishing entries from top to bottom. Matrices $\boldsymbol{U}$ and $\boldsymbol{V}$ are referred to as the left and right singular vectors respectively, while the values within $\boldsymbol{\Sigma}$ are referred to as singular values. A visual example of this can be seen in Figure 3.9.

The factorization of Equation 3.7 leads to the equivalent expression

$$\boldsymbol{X} = \sum_{i=1}^{min\{m,n\}} \sigma_i \vec{u}_i \vec{v}_i \tag{3.6}$$

where σ_i is the singular value in $\boldsymbol{\Sigma}$ at index $[i,\ i]$, $\vec{u}_i$ is the i'th column of matrix $\boldsymbol{U}$, and $\vec{v}_i$ is the i'th row of matrix $\boldsymbol{V}^T$. This is to say that $\boldsymbol{X}$ can be expressed as a sum of positive rank-1 matrices or vectors, with $\boldsymbol{U}$ and $\boldsymbol{V}$ providing said vectors, and $\boldsymbol{\Sigma}$ providing scaling factors.

While this true for all matrices $\boldsymbol{X}$, it is only of value when $\boldsymbol{X}$ is sparse, allowing for low-rank approximation. By definition, $\boldsymbol{\Sigma}$ contains a diminishing set of values along its diagonal; each increment of i in Equation 3.8 will provide a smaller value for σ_i. In a sparse dataset, σ_i can rapidly approach values approximating 0 in as little as 10 indices, leading to large components of both $\boldsymbol{U}$ and $\boldsymbol{V}$ which are effectively

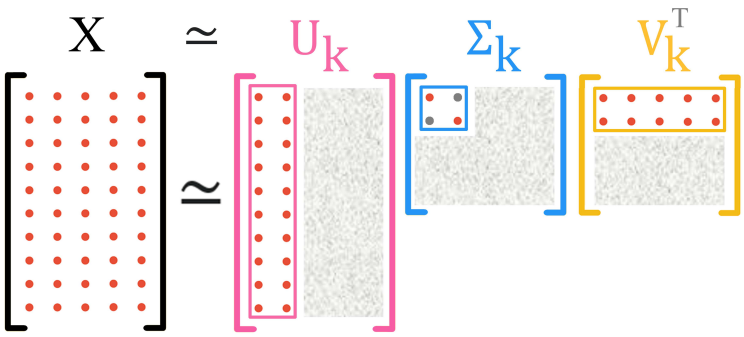

Figure 3.5: A rank 2 approximation of dataset $\boldsymbol{X}$. by removing all by the first few columns/vectors of the singular vectors, SVD can greatly compress large sparse datasets.

multiplied by 0, adding nothing to the summation in Equation 3.8. Thus we can introduce a rank-k approximation to $\boldsymbol{X}$, $\boldsymbol{X}_k$, such that

$$\boldsymbol{X} \simeq \boldsymbol{X}_k = \boldsymbol{U}_k \boldsymbol{\Sigma}_k \boldsymbol{V}_k^T \tag{3.7}$$

where $\boldsymbol{U}_k$ is the first k columns of $\boldsymbol{U}$, $\boldsymbol{V}_k^T$ is the first k rows of $\boldsymbol{V}^T$, and $\boldsymbol{\Sigma}_k$ is the first k rows/columns of $\boldsymbol{\Sigma}$.

Rank-k approximation can compress large sparse datasets by over 99%, and with careful appropriate choice of k, can approach a high approximation of a lossless compression technique. However, the value of k must be appropriately chosen to not degrade the dataset.

3.2 Methods

3.2.1 Sequence Design

A variable density spiral trajectory was used to fully sample k-space in 64 interleaves. Each interleaf sampled 923 points with a 5 μs dwell time, resulting in a 5 ms acquisition window. Dephasing of at least 2π radians was achieved with an unbalanced 3 ms crusher gradient in the slice-select direction as a spoiler between each completed 1000 TR signal acquisition. Each completed 1000 frame segment was appended with a 0.5 s delay, which, while insufficient relaxation time to return spins to thermal

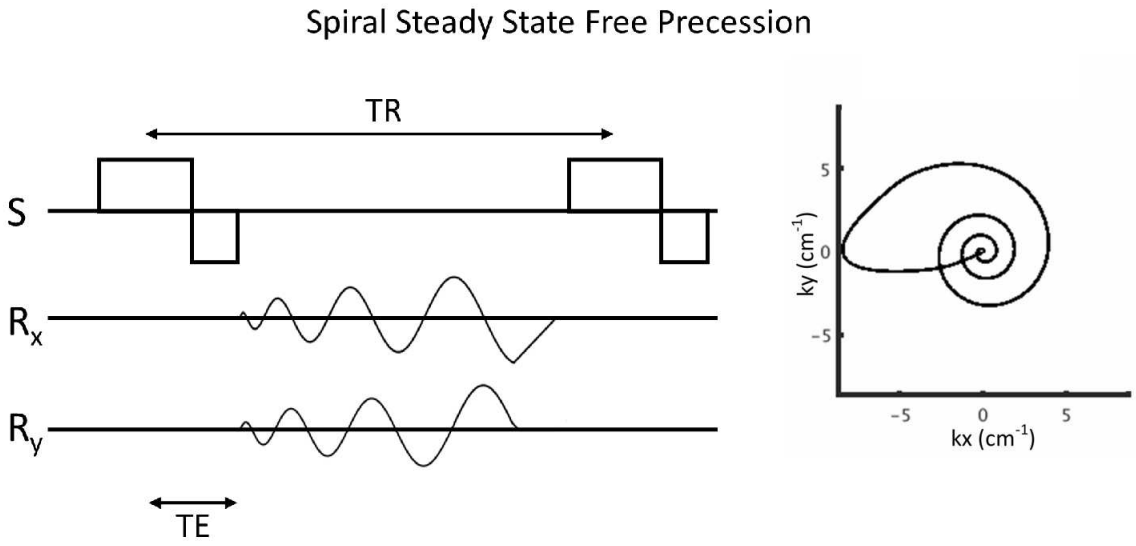

Figure 3.6: (left) Spiral SSFP pulse sequence. This differs from a Cartesian sequence due to the lack of a slice select channel, instead moving in two dimensions during acquisition. (right) k-space trajectory for proposed sequence.

equilibrium, has been shown in previous studies to still allow robust accurate matching once the system has reached a 'stationary fingerprint response', bypassing the assumption of a relaxed initial spin state in dictionaries, and drastically improving scan times[113]. Maximum gradient strength and maximum slew rate were set to 91 mT/m and 200 T/m/s respectively. Slew rate was limited to 66% of the hardware maximum to improve image quality.

The total acquisition time for a full set of 1000 imaging frames each containing a single rotating interleaf is approximately 15 seconds, which is repeated 64 times to acquire a total of 64 interleaves per imaging frame, fully sampling k-space with a total scan time of approximately 20 mins. Each of the 64, 1000-frame interleaf sets were rotated by 360°/64 relative to each other, while individual imaging frames rotated by 7.5° during acquisition.

Often the first step in MRF sequence design is to determine a variation regime which maximizes parameter map accuracy. Three of the most common parameter variations are shown in Figure 3.7. The first is a simple Gaussian noise addition to a baseline value for each parameter, the second is a sinusoidal ramping up and down of the value from 0. The third is 1D Perlin noise, originally designed for providing graphical texture variation without overstressing limited GPUs for use in CGI in

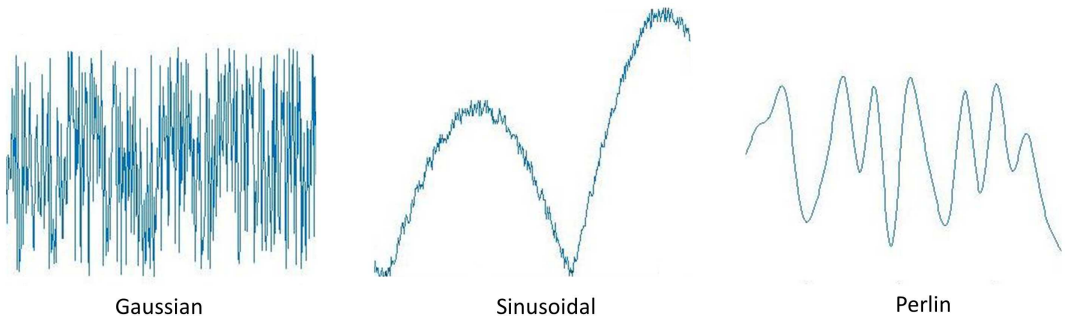

Figure 3.7: Example parameter variations for MRF sequence generation.

the early 90s[114]. It has since been used for its simplicity to implement and high customization, offering a middle ground between the smoothness of a sinusoidal ramp, and Gaussian noise.

To assess various sequence designs sensitivity to parameters, a study similar to one previously analysing sequence encode capability was designed [115]. The intention is to determine both the length and type of sequence variation which leads to the most distinct signals for given T_1 and T_2 values. The combinations of parameter variation tested can be seen in Table 3.1. A basic dictionary was generated for each of the 9 combinations of parameter variation, and a Monte Carlo simulation was implemented to assess the encode capability of each sequence. This was performed by random selection of the same dictionary entry for each sequence variation. Gaussian noise was added to the chosen entries (SNR of 4), which was then rematched back the the respective dictionary. Matching was performed with entry lengths of 50 - 1000 in steps of 50 to assess if fingerprint length affected matching accuracy. This entire process was repeated for 1000 times, and the average percent error for T_1 and T_2 was measured for each variation of parameters.

3.2.2 Dictionary Design

The following equation described the evolution of the magnetization vector at each TR:

$$\vec{M(t)} = P_{TR-TE}\, T_{TR-TE}\, ACQ\, P_{TE}\, T_{TE}\, RF_{\pm\pi}^{FA}\, \vec{M(0)} \tag{3.8}$$

where T, P, and RF are the Bloch operators for relaxation, precession, and RF

	TR	Flip
1	Perlin	Perlin
2	Perlin	Sinusoidal
3	Perlin	Gaussian
4	Sinusoidal	Perlin
5	Gaussian	Perlin
6	Sinusoidal	Sinusoidal
7	Sinusoidal	Gaussian
8	Gaussian	Sinusoidal
9	Gaussian	Gaussian

Table 3.1: Variations used for the Monte Carlo simulation for encode capability testing. Patterns refer to those shown in Figure 3.6.

excitation respectively, and ACQ is the acquisition window. Note that this equation is for a single TR iteration, and does not include additional actions or end-of-interleaf dephasing.

However, as this sequence is non-balanced, EPG provides a more elegant simulation for dictionary entries. Equation 3.8 can be written in analogous terms for an EPG simulation

$$\boldsymbol{\Omega}(t) = \boldsymbol{E}(TE - TR)\, \boldsymbol{S}(TE - TR)\, \boldsymbol{T}(\pm\pi, FA)\, \boldsymbol{E}(TE)\, \boldsymbol{S}(TE)\, \boldsymbol{\Omega}(0) \tag{3.9}$$

where T, E, and S are the RF pulse, relaxation, and dephasing operators respectfully, defined in Equations 2.52 - 2.54. This was used to construct the dictionaries in this work. The primary difference is that in EPG, the operators act on $\boldsymbol{\Omega}$, a matrix containing the three base states for each dephasing order, rather than components of magnetization, allowing for an elegant method of tracking higher order dephasing.

$$\boldsymbol{\Omega} = \begin{bmatrix} \tilde{F}_0 & \tilde{F}_1 & \tilde{F}_2 & \tilde{F}_3 & \tilde{F}_4 & \tilde{F}_5 & ... \\ \tilde{F}_0^* & \tilde{F}_{-1}^* & \tilde{F}_{-2}^* & \tilde{F}_{-3}^* & \tilde{F}_{-4}^* & \tilde{F}_{-5}^* & ... \\ \tilde{Z}_0 & \tilde{Z}_1 & \tilde{Z}_2 & \tilde{Z}_3 & \tilde{Z}_4 & \tilde{Z}_5 & ... \end{bmatrix} \tag{3.10}$$

Despite not including T_2^* sensitivity yet, the dictionary built for this thesis is generated as a 4 dimensional dictionary containing T_1, T_2, and T_2^*. T_2^* entries were set equal to T_2, and were not included in the EPG simulation. The primary purpose of the addition of this length 1 dimension was to allow for future T_2^* additions to

not require a dictionary redesign. Without reshaping, this dictionary scales with increased resolution in the following way:

$$\boldsymbol{D} = N_{T_1} * N_{T_2} * N_{T_2^*} * N_{imagingframes} \tag{3.11}$$

Figure 3.9 (left) demonstrates the redundancy of this dictionary shape. Prior to simulation, nonsensical parameter combinations such as where $T_2 > T_1$ are removed. Conceptualizing a dictionary as a series of 3D data cubes, this removal leaves a substantial corner of each cube empty. If we instead rearrange the dictionary as follows:

$$\boldsymbol{D} = [N_{T_1} \times N_{T_2} \times N_{T_2^*}] * [3 + N_{imagingframes}] \tag{3.12}$$

where the individual dimensions for parameters were concatenated, and three additional columns, referred to as $\boldsymbol{D}_{dir}$, are created, we can greatly decrease dictionary size. These three new columns act as a directory address to each entry, by labelling their associated parameters. This transformation also utilises MATLAB's parallel processing and matrix multiplication, and is also a necessary step for SVD acceleration. Figure 3.9 (right) provides a visualisation of the optimized dictionary architecture.

It is important to strike a balance between the possible accuracy of a dictionary and its size. While the perfect dictionary would contain relaxation time variation with an infinitely small step size, this is not realistic. Thus we must define a dictionary resolution for each relaxation time.

The constructed dictionary in this work originally used a linear step size for all relaxation values over the ranges T_1 = 10-4000 ms, T_2 = 5-1000 ms. This led to a dictionary with over 300,000 entries, with unnecessarily high resolution around the larger values. While this size would be acceptable for traditional MRF, we have to account for future T_2^* addition, which would scale dictionary size to over 3 million. Changing to an incremental step size which increases at higher parameter values greatly decreased dictionary size while still allowing for larger values to be modelled. After removing the nonsensical entries, the final dictionary size is ∼60,000 entries, or 600,000 entries with future T_2^* addition.

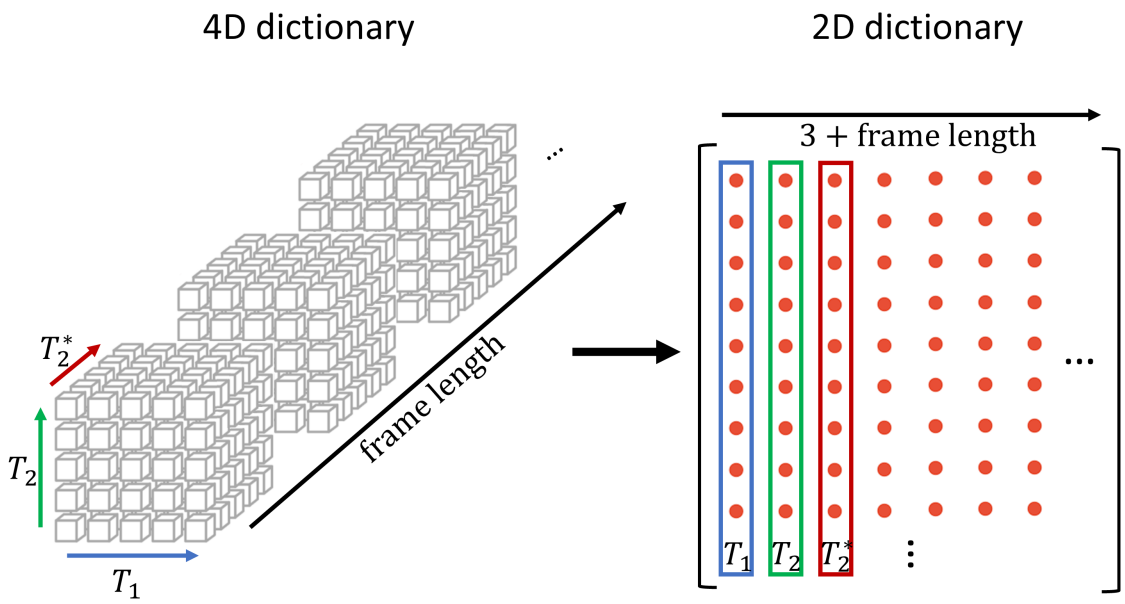

Figure 3.8: Visualization of 4D MRF dictionary at creation, and the 2D dictionary transformation for use/storage. When modelling for multiple parameters, dictionary dimension increases, leading to data which is both difficult to conceptualise and process. Note that while the 4D dictionary in this image is visualised as cubes, prior to simulation, nonsensical entries are removed, such as where $T_1 < T_2$. Therefore these 3D cubes visualized along a 4th axis contain some entirely empty corners. When translating to a 2D dictionary, redundancy is shifted to the parameter columns where they can be removed. These columns, labelled $\boldsymbol{D}_{dir}$, contain all permutations of parameter combinations.

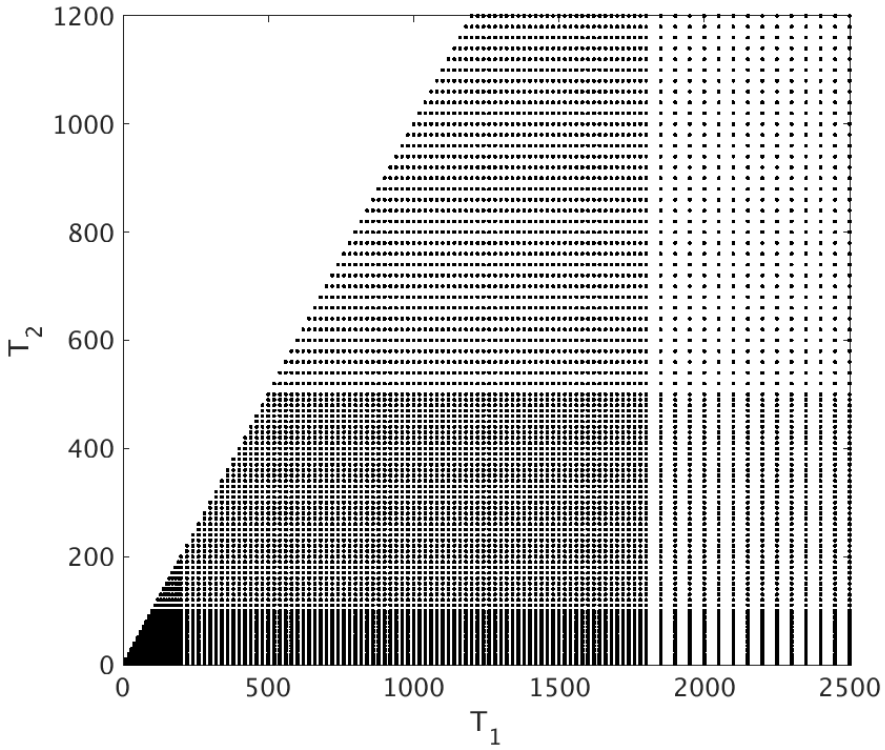

Figure 3.9: Visualization of T_1 and T_2 dictionary resolution. A larger step size is used between higher values of each parameter.

MRF post-processing contains two seperate areas in which SVD can improve both processing speed and digital storage space. The first is the raw FID data prior to reconstruction, and the second is reconstructed data matching to the dictionary. For the former, SVD application has an expected yield of ∼50% increase in processing speed for the proposed method. For the latter, modest application of SVD could improve both matching times and storage needs by over 90%. The primary focus then, was applying SVD to the dictionary matching process.

To apply SVD to the dictionary, it was necessary to reshape the data into the form $\boldsymbol{X}$ in Equation 3.5, which was achieved by cleaving the parameter map directory $\boldsymbol{D}_{dir}$ from the matrix and storing the parameter information separately.

Appropriate choice of rank for SVD is critical; too large a value restricts acceleration, but too few degrades results. To assess the effect of rank on the resulting images, dictionaries with rank ranging from 5 to 30 were generated, as well as a dictionary with no SVD acceleration included. Phantoms containing MnCl2 were created and imaged using the MRF sequence (64 x 64, 30 mins). Prior to dictionary matching, SVD was retrospectively applied to the regridded MRF signal with various ranks ranging from 5 - 30. SVD Dictionaries were used to match their respective MRF signals, and the resulting T_2 maps were compared to the non-SVD dictionary map. T_2 was chosen as the metric for SVD sensitivity as the values are much closer in the dictionary, and therefore more likely to be degraded compared to T_1.

3.2.3 Parameter Map Generation

While optimizing sequence variation for sensitivity and dictionary for speed are important, it is also necessary to demonstrate that the implementation of MRF can provide accurate parameter maps. Figure 3.10 shows the final iteration of parameter evolution chosen for this MRF version. Here, both Perlin and sinusoidal variation are utilized, as well as brief periods with 0° flip angle serve to increase T_1 accuracy.

A phantom set doped with various concentrations of MnCl2 in 8% gelatin was created and imaged using fully sampled spiral MRF. The concentrations can be found in Table 3.2. To verify the accuracy of MRF parameters, T_1 and T_2 MRF maps (FOV 35 × 35 × 1 mm FOV, 128 × 128 resolution) were compared to conventional methods for bulk quantification. Bulk T_1 measurements were made using an inversion recovery

	1	2	3	4	5
Concentration (mM)	0.025	0.05	0.1	0.2	0.4

Table 3.2: Concentrations for phantoms containing MnCl2 in 8% gelatin.

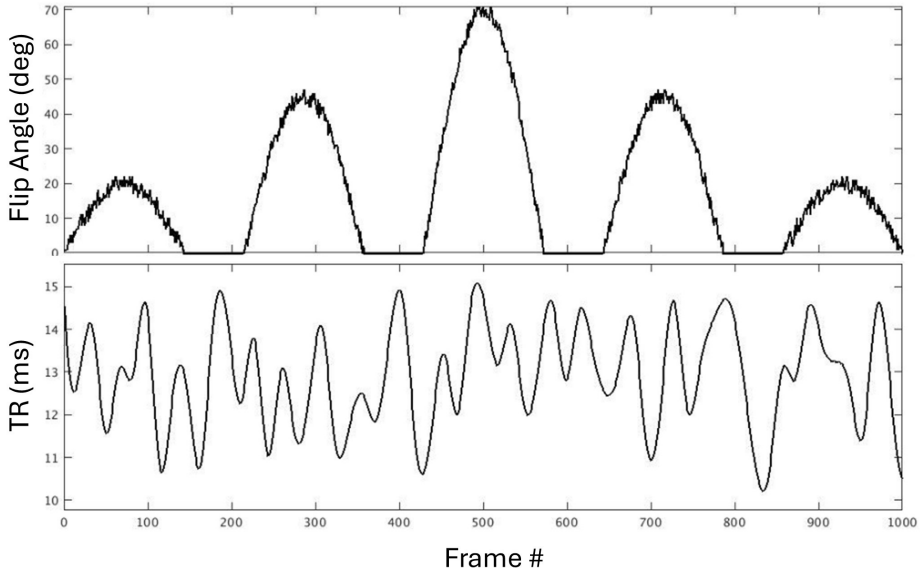

Figure 3.10: MRF Parameter Variation. Flip angle variation is performed via 5 sinusoidal ramps of varying height, with periods containing no flip angle to increase T_1 sensitivity. TR is defined by a 1D Perlin variation between 10 and 14 ms.

spin-echo sequence, with TI varying from 0.1 to 6.4 s in 7 steps, leading to an acquisition time of 30 seconds. Bulk T_2 measurements were made using a spin-echo sequence, with a TE varying from 0.05 to 0.5 s in 10 steps, for a total acquisition time of 30 seconds. Results were compared using Lin's concordance correlation coefficient[116].

3.3 Results + Discussion

3.3.1 Sequence Design

Figure 3.11 shows the results of the Monte Carlo simulation to determine the sequence variation with the most sensitivity to parameter changes. The two best performing sequence variations, Perlin TR/Perlin flip, and Perlin TR/sinusoidal flip are shown, as well as Gaussian TR/Perlin flip as a representative of a less well performing sequence. The other 6 sequence variations are not shown for clarity, but all perform roughly

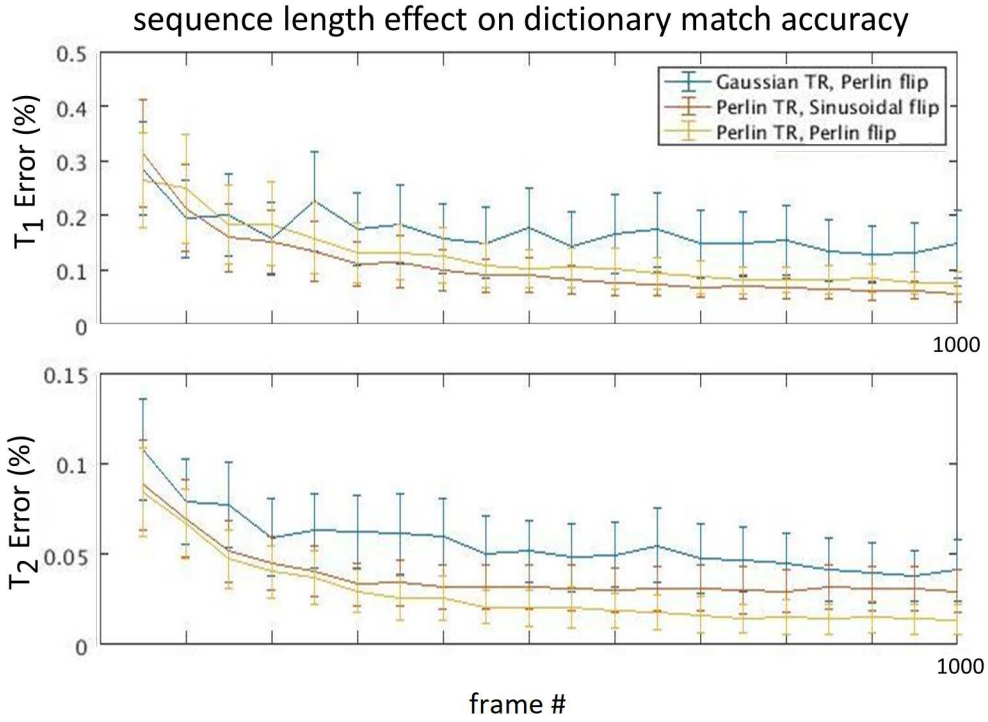

Figure 3.11: Results of parameter variation tests. Of the nine parameter variation combinations testing, here are the results for the three with the lowest error. In general, any addition of Gaussian variation was outperformed by sets where it was not present.

equivalent to Guassian TR/Perlin flip, as shown in Table 3.3. In general, we see that the addition of Gaussian variation degrades sensitivity of the MRF sequence; with the except of Guassian TR/Perlin flip, non-Gaussian sequences outperform Gaussian sequences in error percentage in every case. We also see that T_1 error is minimized by a Perlin TR/Perlin flip pattern, but T_2 error was minimized in the Perlin TR/sinusoidal flip sequence. This may suggest that the optimal sequence configuration for this implementation contains both Perlin and sinusoidal sections of variation to maximize both T_1 and T_2 sensitivity, or support that T_1 sensitivity is improved when 0° flip is included throughout the sequence. Lastly, we note that at above 350 iterations of TR, increasing the fingerprint length of single pattern provided no parameter accuracy increase. This data therefore may support switching to a new sequence variation every 300 frames to increase parameter accuracy.

TR	Flip	T_1 Error (%)	T_1 std (%)	T_2 Error (%)	T_2 std (%)
Perlin	Perlin	0.131	0.0527	0.024	0.0115
Perlin	Sinusoidal	0.112	0.048	0.037	0.01
Perlin	Guassian	0.165	0.0561	0.059	0.017
Sinusoidal	Perlin	0.176	0.0614	0.048	0.017
Guassian	Perlin	0.181	0.076	0.062	0.021
Sinusoidal	Sinusoidal	0.168	0.0691	0.055	0.02
Sinusoidal	Guassian	0.199	0.074	0.069	0.027
Guassian	Sinusoidal	0.207	0.078	0.072	0.03
Guassian	Guassian	0.238	0.09	0.082	0.032

Table 3.3: Monte Carlo Results using 350 frames of fingerprint data. Figure 3.11 shows that results stabilize at approximately this point.

3.3.2 Dictionary Design

Figure 3.12 and show the results of SVD tests for our implementation of MRF. The primary focus for application of SVD was the dictionary matching process, to greatly increase matching times and dictionary storage size. As expected, we find that lowering the rank of the SVD dictionary degrades results, increasing the nRMSE of T_2 maps when compared to the no-SVD results. We also find that above rank 17, SVD implementation has no effect on results. As we are expecting to include T_2* sensitivity in the future, a rank-25 SVD was chosen to be sufficient acceleration, without danger of too closely approaching a value which may affect data fidelity. Rank-25 SVD resulted in a 95% improvement to both speed and storage. Application of rank-25 SVD took approximately 5 mins, which reduces matching times from 2 hours to 5 mins. Dictionary storage space was reduced from 2 GB to 10 MB, and while the initialization of an SVD dictionary can take up to 2 hours, this process is only performed a single time.

3.3.3 Parameter Map Generation

Figure 3.13 shows the results for the parameter map validation for spiral SSFP MRF. When compared to conventional values, both T_1 and T_2 show excellent agreement, with Lin's concordance correlation coefficient [116] CCC values exceeding 0.99. Visually, we find that T_1 tends to slightly underestimate when compared to gold standard inversion recovery, but still shows robust scaling from 300-1800 ms, a similar scale to

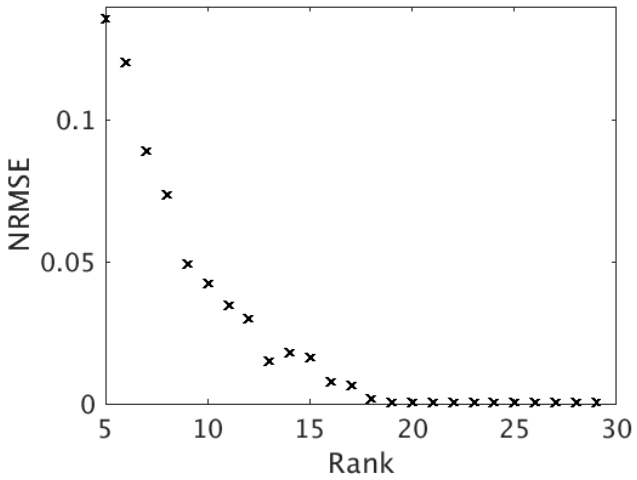

Figure 3.12: SVD rank effect on parameter map accuracy. Matching results started to deviate from the standard matching at under a rank of 20.

that found in preclinical imaging. When moving forward, including inversion recovery at the start of each interleaf may help to more accurately capture T_1 dynamics.

3.4 Conclusion

In this chapter, we have outlined the requirements to successfully generate parameter maps using an MRF sequence based on SSFP with a spiral readout. After a brief introduction to the underlying theory behind MRF sequences and their dictionaries, a method was laid out to implement MRF on our preclinical system. This included a Monte Carlo simulation to help elucidate the best TR/flip angle variation for parameter sensitivity, as well as dictionary acceleration using SVD, and validation of parameter map accuracy.

Sequence TR/flip angle variation results showed that 1D Perlin variation offered the lowest error in parameter values in general, while Gaussian variation offered the highest error percent. It was also found that sinusoidal flip angle variation may increase T_1 variation, but that this may has also been related to the 0° sections included in the sinusoidal pattern. Lastly, results showed that after around 350 frames of the same pattern, longer sequences did not increase the accuracy of matching.

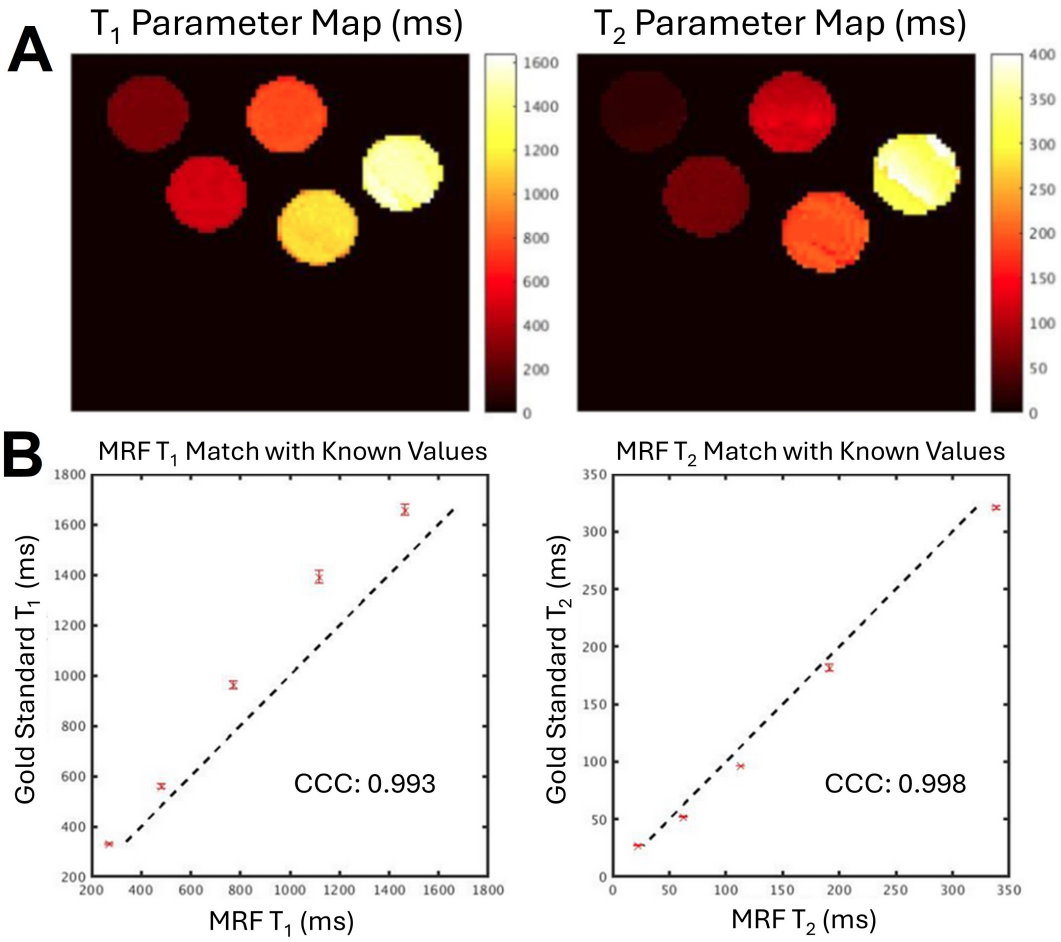

Figure 3.13: Parameter validation for T_1 and T_2 spiral SSFP MRF.

SVD results showed that above rank-17, dictionary matching results were not degraded when compared to non-SVD dictionary matching, and that a 95% acceleration in dictionary matching speed and size could be achieved with this method. Finally, parameter map validation tests against gold standard bulk measurements showed that this implementation of MRF can accurately map both T_1 and T_2, and while slightly underestimating T_1, CCC values for both parameters exceeded 0.99, showing excellent matching. This provides a strong foundation on which to build a dual contrast MRF sequence with T_2^* sensitivity on.

Chapter 4

Simultaneous Dual Quantification of Contrast Agents

The contents of this chapter were published in https://doi.org/10.1016/j.mri.2021.03.017

4.1 Abstract

Purpose: Develop a magnetic resonance fingerprinting (MRF) methodology with R_2^* quantification, intended for use with simultaneous contrast agent concentration mapping, particularly gadolinium (Gd) and iron labelled cytotoxic lymphocytes.

Methods: Variable-density spiral SSFP MRF was used, modified to allow variable TE, and with an exp(-TE·R_2^*) dictionary modulation. In vitro phantoms containing SPIO labelled cells and/or gadolinium were used to validate parameter maps, probe undersampling capacity, and verify dual quantification capabilities. A C57BL/6 mouse was imaged using MRF to demonstrate acceptable *in vivo* resolution and signal at 8x undersampling necessary for a 25-minute scan.

Results: Strong agreement was found between conventional and MRF-derived values for R_1, R_2, and R_2^*. Expanded MRF allowed quantification of iron-loaded cytotoxic lymphocytes. Results were robust to 8x undersampling and enabled recreation of relaxation profiles for both a Gd agent and iron labelled cells simultaneously. *In vivo* data demonstrated sufficient SNR in undersampled data for parameter mapping to visualise key features.

Conclusion: MRF can be expanded to include R_1, R_2, and R_2^* mapping required for simultaneous quantification of gadolinium and SPIO *in vitro*, allowing for potential implementation of a variety of future *in vivo* studies using dual MR contrast agents, including molecular imaging of labelled cells.

4.2 Introduction

MR contrast agents are routinely used for the detection of pathological changes with high sensitivity and specificity by enhancing the contrast between healthy and unhealthy tissue[117]. Due to MRI's excellent contrast and resolution deep within soft tissue and its non-invasive nature, it is also uniquely suited to quantifying contrast agents *in vivo*, by using the linear relationship between agent concentration and the relaxation rate of the surrounding tissue[118]. Imaging different time points as an agent moves through a system can, therefore, highlight migration patterns of individual agents, making MRI an excellent tool for tracking cells labelled with contrast agents.

MRI-based cellular imaging can yield valuable information about the localization of crucial immune cell subsets, and has been used by several groups to follow adoptive transfer of immune cells that are used as a therapy or to track macrophages[119, 120, 109]. However, immune cell tracking to explore non-cell-based therapies is still in its infancy, and many of the challenges of MRI cellular tracking have still yet to be addressed. In this rapidly developing field, it is critical that MR cell tracking techniques be improved to increase the efficacy of cell tracking studies, improve quantification capabilities, and decrease financial costs and scan times.

In recent years, the range of available contrast agents being developed has rapidly expanded, in particular for molecular imaging studies, where advances within the field have allowed for contrast agent targeting of specific molecular species[120, 109, 12, 121]. This diversity in options has led to increasing interest in not only imaging but quantifying multiple contrast agents simultaneously. Multi-parametric MRI using two or more forms of contrast (whether endogenous or exogenous agents) offers more molecular information without trade-offs of increased time or resources.

Unfortunately, simultaneous quantification of two contrast agents requires a method that provides multiple relaxation maps within a time frame narrow enough to capture the dynamics of the mechanism of interest. Few sequences fulfil these requirements since conventional methods of mapping R_1 or R_2 rely on sampling at multiple points during signal evolution [73, 75], which is a time-consuming process, both preclinically and clinically.

Magnetic resonance fingerprinting (MRF) offers a novel imaging methodology that

can generate multiple parameter maps simultaneously[82], with the additional benefit of being robust to undersampling artifacts[83], allowing for greatly accelerated acquisition times. MRF traditionally measures R_1 and R_2 parameter maps, and previous studies have shown that R_1 and R_2 information gathered using MRF can separate two contrast agents (a Gd-based agent and a Mn-based agent) administered simultaneously in vitro, providing concentration estimations[96].

Recently there has been an emergence of MRF including R_2^* quantification, either by phase manipulation[99] or TE variation[97, 98]. However, simultaneous concentration estimation of an R_2^* weighted contrast agent (such as SPIO) and an R_1 agent has not yet been demonstrated. The additional challenges when attempting to quantify R_2^* agents are related to their nature as "negative" contrast agents, whereby increased concentrations decrease the signal magnitude, creating difficulties in acquiring sufficient signal for a dictionary match. In this paper, we propose a method for accurately estimating concentrations of an R_1 and R_2^* agent simultaneously *in vitro*.

The goal of this study was to develop an MRF methodology that included R_2^* quantification, and assess its capabilities for preclinical concentration mapping of two contrast agents present simultaneously. Accurate mapping of R_1, R_2, and R_2^* was demonstrated with a similar degree of confidence to previous methods. *In vitro*, both a gadolinium agent and SPIO loaded cytotoxic lymphocyte (CTL) concentrations were shown to be measured simultaneously, and the effects of undersampling capacity on resulting parameter maps were evaluated. Finally, MRF was applied *in vivo*, to act as a pilot study, demonstrating the potential feasibility of this technique to provide sufficient resolution and signal within a 30-minute scan.

4.3 Methods

All studies were performed on a 3T preclinical scanner (Agilent, Santa Clara, CA), with a quadrature RF coil. Experiments involving the use of mice were carried out following protocols approved by the University Committee on Laboratory Animals at Dalhousie University, Halifax, NS, Canada. All mice were housed at the IWK *In Vivo* Animal Care Facility with food and water *ad libitum* under filter top conditions. Reconstruction and matching were performed in MATLAB (The MathWorks; Natick, MA), on a virtual machine with 200 GB memory and 24 CPUs running on a Linux

enterprise cluster.

4.3.1 Pulse Sequence Design

The proposed acquisition strategy, shown in Figure 4.1, is based on a gradient spoiled Steady-State Free Precession (SSFP) type sequence with varied TR, TE and flip angle (FA) for 1000 imaging frames. An adiabatic inversion pulse is used at the start of the sequence to improve R_1 sensitivity. The sequence can be split into 3 segments, as shown by the divided parts of Figure 4.1B. In the first segment, TR, TE and FA are held constant, to allow for traditional steady-state restoration for a total of 200 frames. The second segment contains 1D Perlin variation[114] of TR between 16 and 20 ms, and a FA Perlin noise pattern between 20 - 60°, with 2 areas where no FA is applied. This section lasts for 400 iterations, and during this time TE is held constant. In the final section, FA is held constant, while TE is varied sinusoidally increasing from 5 to 10 ms. The TE variation sensitizes the sequence to R_2^* effects.

A variable density spiral trajectory was used to fully sample the centre of k-space in 8 interleaves, and the outer areas of k-space in 64 interleaves. Each interleaf sampled 923 points with a 5 μs dwell time, resulting in a 5 ms acquisition window. Dephasing of at least 2π radians was achieved with an unbalanced 3 ms crusher gradient in the slice-select direction as a spoiler between each completed 1000 TR signal acquisition. Each completed 1000 frame segment was appended with a 0.5 s delay, which, while insufficient relaxation time to return spins to thermal equilibrium, has been shown in previous studies to still allow robust accurate matching once the system has reached a 'stationary fingerprint response', bypassing the assumption of a relaxed initial spin state in dictionaries, and drastically improving scan times[113]. Maximum gradient strength and maximum slew rate were set to 91 mT/m and 200 T/m/s respectively. Slew rate was limited to 66% of the hardware maximum to improve image quality.

The total acquisition time for a full set of 1000 imaging frames each containing a single rotating interleaf is approximately 15 seconds, which is repeated 8 times to acquire a total of 8 interleaves per imaging frame per slice, fully sampling inner k-space with a total scan time of approximately 2 mins. Each of the 8 1000-frame interleaf sets were rotated by 360°/8 relative to each other, while individual imaging frames rotated by 7.5° during acquisition.

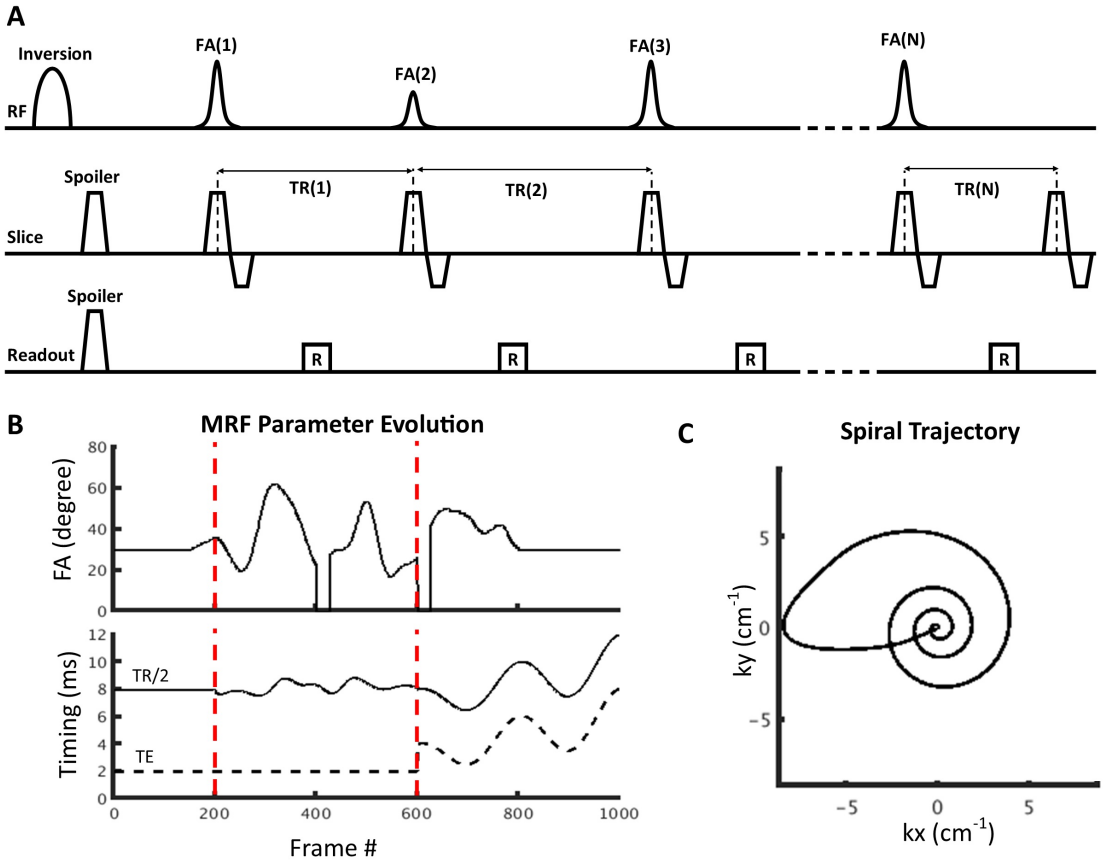

Figure 4.1: MRF sequence details. A, Acquisition sequence for SSFP MRF indicating approximate RF pulse and gradient timings. B, flip angles (FA) and TE/TR for each imaging frame. Red lines show the transitions between different parameter regimes, increasing the sensitivity of the sequence. C, Variable density spiral trajectory for a single interleaf.

4.3.2 Dictionary Design

A dictionary-based on the Extended Phase Graphing (EPG)[85] framework was used to estimate R_1, R_2 and R_2^* from the data following reconstruction. SSFP's lack of sensitivity to off-resonance signal allows such behaviour to be neglected in the dictionary[87], reducing the dictionary size and enabling faster processing.

After R_1 + R_2 dictionary generation, R_2^* decay was simulated by scaling the signal according to the echo time at each TR by via the equation exp(-TE$\cdot R_2^*$). The dictionary was calculated over values of R_1 = 0.25-100 s^{-1}, R_2 = 1-200 s^{-1}, and R_2^* = 4-1000 s^{-1}, all with an increment of 5% per step. Illogical entries were removed, such as entries where $R_1 > R_2$. The dictionary was approximately 600,000 entries, taking around 15 minutes to construct.

Dictionary matching was performed by calculating the maximum dot product of the signal with each dictionary entry. The largest product was taken to represent the closest match, providing an estimation of R_1, R_2, and R_2^* within approximately 2 minutes per slice for a 64 x 64 image.

4.3.3 Parameter Map Validation

Phantoms were prepared which contained either ProHance (Gadoteridol; Bracco Imaging) and/or CTLs labelled with SPIO. CTLs were isolated from female C57BL/6 mice (6-8 weeks old, pathogen-free) obtained from Charles River Laboratories (St. Constant, PQ).

For cell isolation, inguinal, axial, brachial, and mesenteric lymph nodes (LNs) were removed from C57BL/6 mice. CTLs were isolated as previously described[38]. Nine days after isolation, CTLs were washed and incubated with Molday IONTM Rhodamine B SPIO (75 µg/mL; 30 nm, BioPal Inc, Worchester, Massachusetts, USA), hereafter referred to simply as SPIO, at a density of 4 million cells/mL in cRPMI supplemented with IL-2 (100 U/mL) for 22 hours. Labelled cells were washed thoroughly in 1XPBS and resuspended in 1XPBS before adding gelatin and manganese chloride (Sigma, 0.05 mM concentration) during phantom preparation. Gadolinium (ProHance) was also added to some tubes. For single-agent tubes, 10 phantoms were prepared with concentrations ranging from 0.05 – 8.75 million cells/mL, suspended in 8% gelatin in 5 mm NMR tubes. For dual agent tubes, gadolinium concentration

I a

1	2	3	4	5	6
0.54	0.36	0.27	0.21	0.17	0.135

I b

1	2	3	4	5	6	7	8	9	10
0.1	0.25	0.5	1	3	5	7.5	10	15	17.5

I c

1	2	3	4	5	6	7	8	9	10
0.45	0.4	0.35	0.3	0.25	0.2	0.15	0.1	0.05	0
0.125	0.25	0.5	1.25	2.5	3.75	5	6.25	7.5	0

I c (cont.)

11	12	13	14	15
0.2	0	0.2	0.4	0.3
1.25	1.25	7.5	7.5	7.5

Table 4.1: Composition of all phantoms. I a, Gadolinium doped phantoms used to demonstrate the undersampling capacity of MRF. I b, SPIO-loaded cell phantoms, demonstrating concentration mapping using MRF in Figure 4.5. I c, Dual contrast phantoms. This set was also doped with 0.05 mM of MnCl2 to achieve more biologically relevant relaxivities.

ranged from 0.05 – 0.5 mM, ascending, and the number of cells ranged from 0.125 – 7.5 million/mL, descending (see Table 4.1).

To verify the accuracy of MRF parameters, R_1, R_2, and R_2^* MRF maps (FOV 35 $\times$ 35 $\times$ 1 mm FOV, 128 $\times$ 128 resolution) were compared to conventional methods for bulk quantification. Bulk R_1 measurements were made using an inversion recovery spin-echo sequence, with TI varying from 0.1 to 6.4 s in 7 steps, leading to an acquisition time of 30 seconds. Bulk R_2 measurements were made using a spin-echo sequence, with a TE varying from 0.05 to 0.5 s in 10 steps, for a total acquisition time of 30 seconds. R_2^* maps were acquired using a TurboSPI sequence[122] (128 $\times$ 128 matrix, 30 $\times$ 30 $\times$ 10 mm FOV, 15 mm slab excitation, ETL = 8, TE/TR = 8/250 ms, echo spacing = 8 ms).

4.3.4 Undersampling Capacity

To evaluate the undersampling capabilities of the MRF sequence, data from the parameter map validation experiment was retrospectively undersampled by factors of 2, 4, 8, and 16. A single slice was acquired (FOV 20 $\times$ 20 $\times$ 1 mm FOV, 128

$\times$ 128 resolution), and R_1, R_2, and R_2^* maps were generated via dictionary matching. Parameter estimation was compared with fully-sampled data, both visually, and quantitatively by calculating the normalized root mean squared error (NRMSE). A pixel-wise correlation was performed on the resulting parameter maps, both for phantoms containing SPIO and ProHance, as well as those containing only ProHance, to verify undersampling capacity for a variety of scenarios.

4.3.5 Cellular Concentration Map Validation

Single Agent

MRF was performed with 8x undersampling to expedite scan times (FOV 35 $\times$ 35 $\times$ 1 mm FOV, 128 $\times$ 128 resolution). Concentration maps were created by the use of the well-established concentration-dependent linear model[118]:

$$R_2^* = R_{2,0}^* + r_2^*[A] \tag{4.1}$$

$R_{2,0}^*$ is the relaxation rate in the absence of iron-loaded cells, r_2^* is the relaxivity of the cells, and [A] is the cellular concentration. To validate cellular concentration mapping, an average of the central 5 x 5 voxels for each phantom was compared to known values. CCC and linear regression fits were used to determine how well the estimate matched the known values over a range of concentrations.

Dual Contrast Agents

To assess MRF's ability to quantify two contrast agents simultaneously, the phantoms containing both ProHance and CTLs labelled with SPIO were used. Parameter estimation maps were found using MRF (FOV 35 $\times$ 35 $\times$ 1 mm FOV, 64 $\times$ 64 resolution), and concentration maps were created using these maps, via an expansion to the linear relaxation model[97]

$$R_1 = R_{1,0} + r_{1A}[A] + r_{1B}[B] \tag{4.2}$$

$$R_2^* = R_{2,0}^* + r_{2A}^*[A] + r_{2B}^*[B] \tag{4.3}$$

where [B] is the concentration of the second agent, in this case Gadolinium, and r_{1B} and r^*_{2B} are the magnetic relaxivities of the second agent. The ProHance r_1 relaxivity value was taken from the literature[123]. The relaxivity values of the CTLs, as well as r^*_2 for ProHance, were calculated by comparing conventional R_1 and R^*_2 values of phantoms containing fixed amounts of the other contrast agent. These concentration maps were compared to the known concentration values after masking was applied using a threshold based on the strength of the match to the best dictionary entry for each pixel.

4.3.6 *In Vivo* Experiments

For *in vivo* tests a C57BL/6 mouse was imaged. The mouse was anesthetized using an induction dose of 3% isofluorane and maintained at 1.5-2%, with temperature and breathing rate monitored during all experiments. Breathing rate was maintained between 60-100 breaths per minute, and internal temperature at around 37 °C via forced warm air.

To demonstrate *in vivo* feasibility of this technique, the mouse was imaged using MRF, as well as an R_2-weighted scan (TE=6.3 ms, ETL = 8) for anatomical reference. MRF was undersampled 8x to produce $128 \times 128 \times 8$ images in 25 minutes and T_1, T_2 and T^*_2 maps were generated for a representative slice.

4.4 Results

4.4.1 Parameter Map Validation

Figure 4.2A, B shows the comparison between R_1 and R_2 values acquired by conventional methods and by MRF. These show an excellent match, with CCC values exceeding 0.94. Figure 4.2C, which demonstrates the match between conventional and MRF R^*_2 values, is also very good, albeit less than R_1 and R_2, with a CCC of 0.88. MRF appears to slightly underestimate R^*_2 values below 50 s^{-1} and marginally overestimate R^*_2 values over 100 s^{-1}, as compared to the TurboSPI estimate.

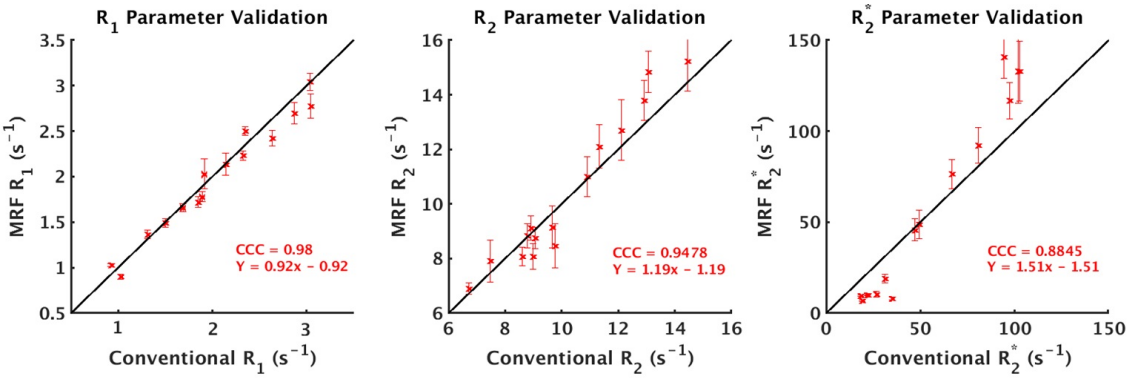

Figure 4.2: Parameter map validation of MRF extended for R_2^*, using phantoms with both SPIO and ProHance. The correlation between MRF parameter estimations and the gold standard (bulk relaxation rate measurements) for R_1, R_2, and R_2^* are shown in (A), (B), and (C), respectively. The equations correspond to the linear regression fit. Error bars represent the standard deviation of the inner 5 x 5 area of each phantom.

4.4.2 Undersampling Capacity

Data from various undersampling factors R are shown in Figure 4.3. As undersampling is increased, more artifacts are seen within the images, and in each voxels corresponding fingerprint signal. Despite this, R_1 and R_2 maps are robust to this undersampling and yield values similar to fully-sampled data.

Figure 4.4 A, B, C show the correlation between 5 individual randomly selected voxels from the inner 5 x 5 region of each phantom, for both fully-sampled and 8x undersampled data. All three parameters demonstrate exceptional robustness to 8x undersampling, with CCC values exceeding 0.94, and visually there is a clear and strong correlation between the undersampled and fully-sampled parameter values.

The NRMSE for R_1, R_2, and R_2^* as a function of the undersampling factor is shown in Figure 4.4D. NRMSE increases for all parameters as undersampling increases. All parameters demonstrated an NRMSE of 0.05 at 8x undersampling, with R_2^* displaying a marginally smaller value than R_1 and R_2 for undersampling factors of less than 8x. However, at 16x undersampling, the NRMSE of R_2^* is greatly increased, exceeding that of both R_1 and R_2.

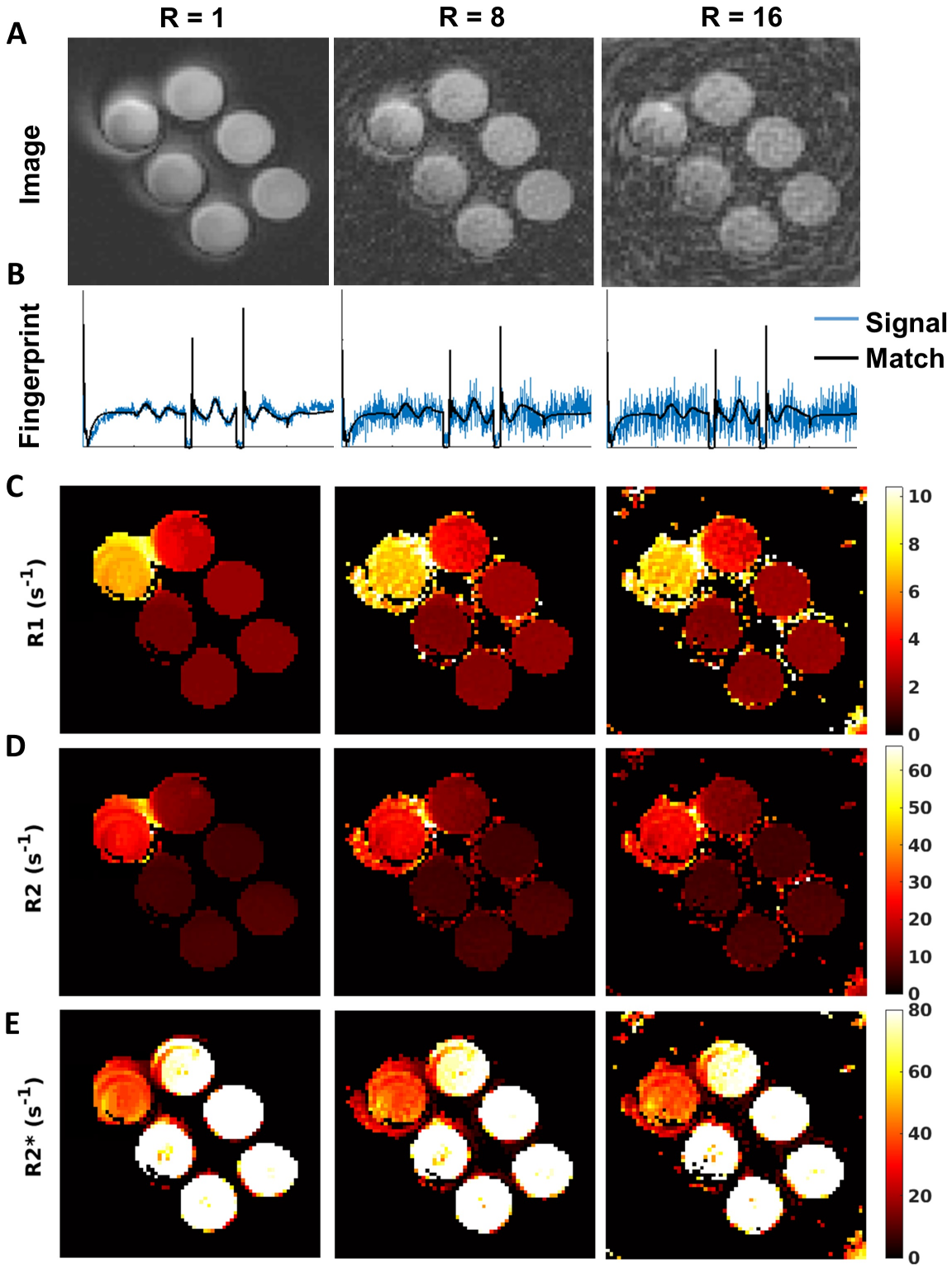

Figure 4.3: Relaxation rate maps from fully-sampled and undersampled SSFP-MRF with R_2^* modifications. Phantoms contain varying amounts of ProHance. A, Images are taken from a single imaging frame of the sequence with varying undersampling factors. B, Example signal from a single pixel within the image showing its evolution through the sequence, and the corresponding best-matched fingerprint. C, D, E Reconstructed R_1, R_2, R_2^* and maps from undersampling factors R = 1, 8, 16.

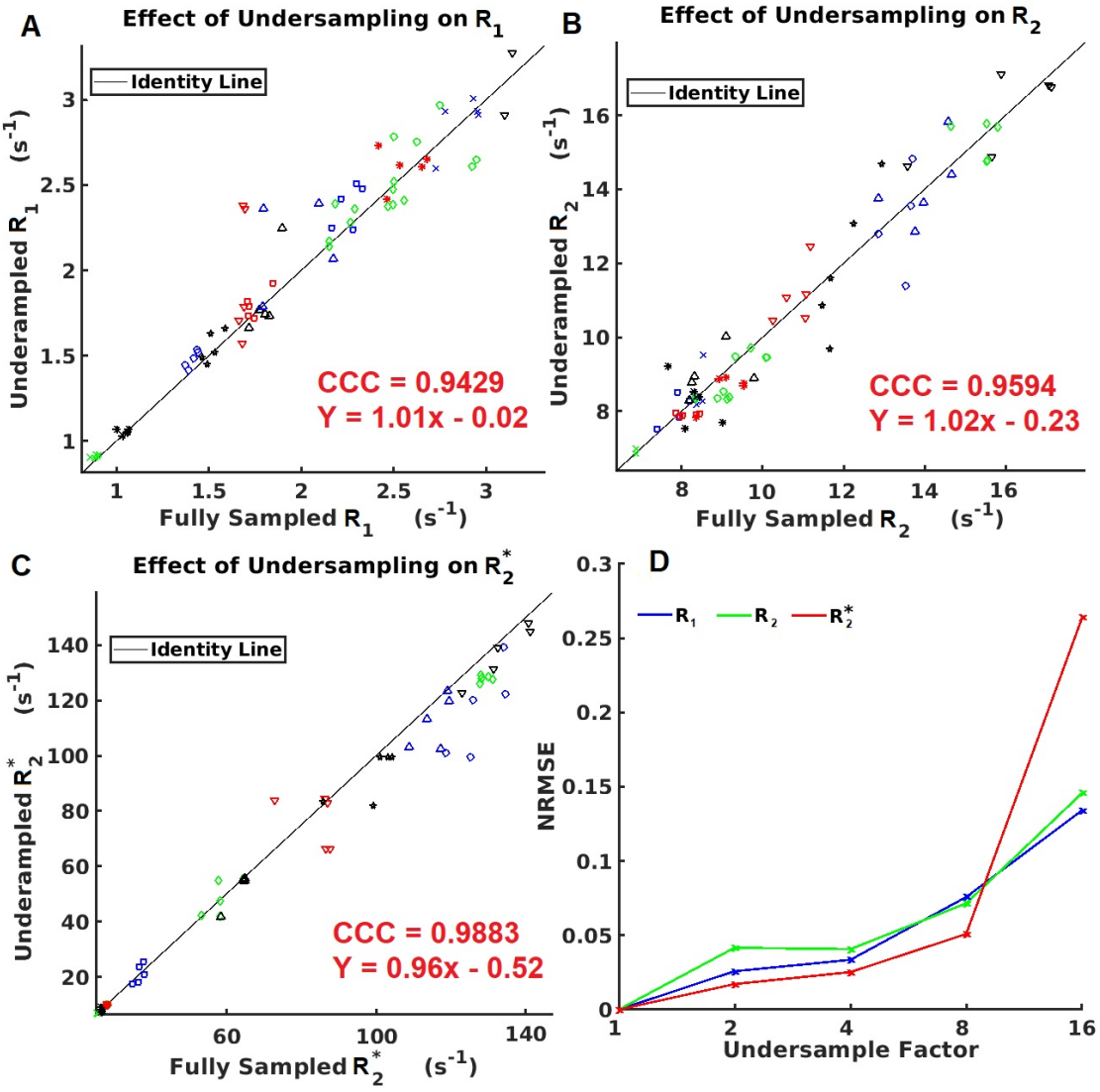

Figure 4.4: Data integrity calculations for R_1, R_2, and R_2^* from undersampled data. The correlation between fully-sampled and undersampled data (R=8) for R_1, R_2, and R_2^* are shown in (A), (B), and (C), respectively. Different colours/shapes indicate different phantoms from within the SPIO + ProHance phantom set. D, Normalised RMSE of R_1, R_2, and R_2^* values with increasing undersampling factor, as compared to fully-sampled values.

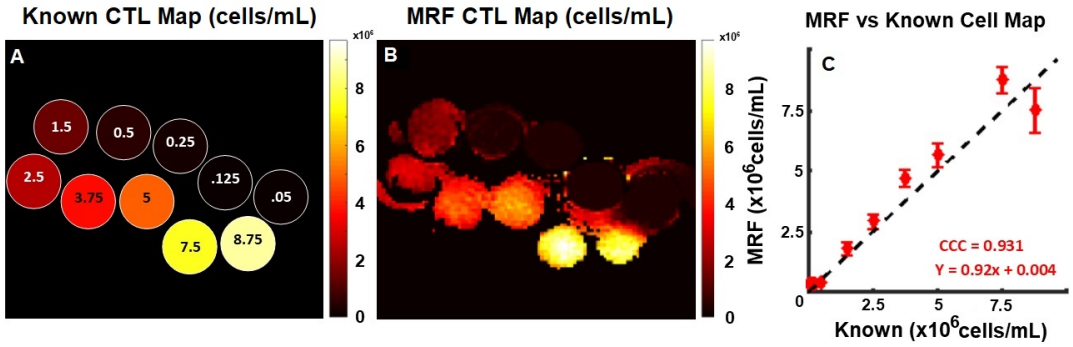

Figure 4.5: Concentration mapping results from the phantoms containing only SPIO-loaded CTLs. A, Known CTL map (10^6 cells/mL) B, MRF CTL estimation map (cells/mL) at R = 8 undersampling factor. C, Correlation between known concentration values and estimated concentration value (10^6 cells/mL). The equations and dashed line correspond to the linear regression fit. Error bars represent the standard deviation of the inner 5 x 5 area of each phantom.

4.4.3 Concentration Map Validation

Single Agent

A comparison between the known and estimated number of CTLs is shown in Figure 4.5. The data shows strong agreement, with CCC greater than 0.93. Maps obtained with MRF agree visually with the known phantom layout, with some small spiral artifacts. Between the ranges of 2.5 million to 7.5 million cells/mL, CCC exceeds 0.99. Below approximately 500,000 cells/mL, the estimation is shown to plateau.

Dual Contrast Agent

Figure 4.6 displays the results of the dual contrast concentration mapping. 4.6A, D show the known concentrations of each of the respective agents. 4.6B, E show the MRF generated concentration maps. Masking delineates between most of the phantoms, with the exception being the bottom right tubes, which demonstrate some artefactual blooming. The MRF-estimated concentration maps show reasonable homogeneity within each phantom and are visually similar to the known concentration values.

Figures 4.6C, F show the numerical match between the inner 5 x 5 voxel region of each phantom to the known concentration value. CCC and linear regression fit

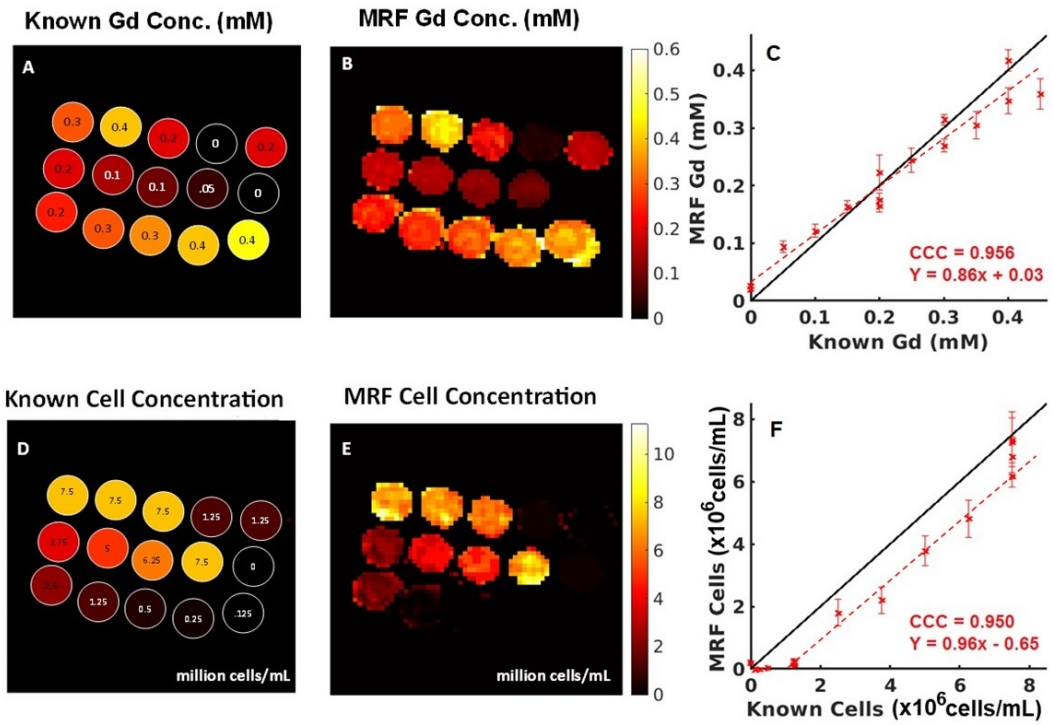

Figure 4.6: Concentration mapping results for phantoms with both SPIO loaded CTLs and ProHance. A, D, Known concentration map. B, E, MRF concentration estimation map. C, F, Correlation between known concentration values and estimated concentration values. Equations correspond to the linear regression fit. Error bars represent the standard deviation of the inner 5 x 5 area of each phantom.

for both figures show good agreement between MRF and known values. The MRF estimation of cell concentration appears to slightly underestimate the concentration value within the phantoms which contain fewer than 500,000 cells/mL. This underestimation can directly be attributed to the technique's slight underestimation of R_2^* values below 50 s^{-1}.

In Vivo Experiments

Figure 4.7 contains results for MRF *in vivo* feasibility. Figure 4.7A provides an anatomical axial slice for reference. Figures 4.7B, C, and D are the associated T_1, T_2, and T_2^* parameter maps generated via MRF. Parameter maps are threshold masked to the anatomical image for improved comparison. Even at 8x undersampling, maps demonstrate sufficient SNR and contrast distinctions to be able to localize major

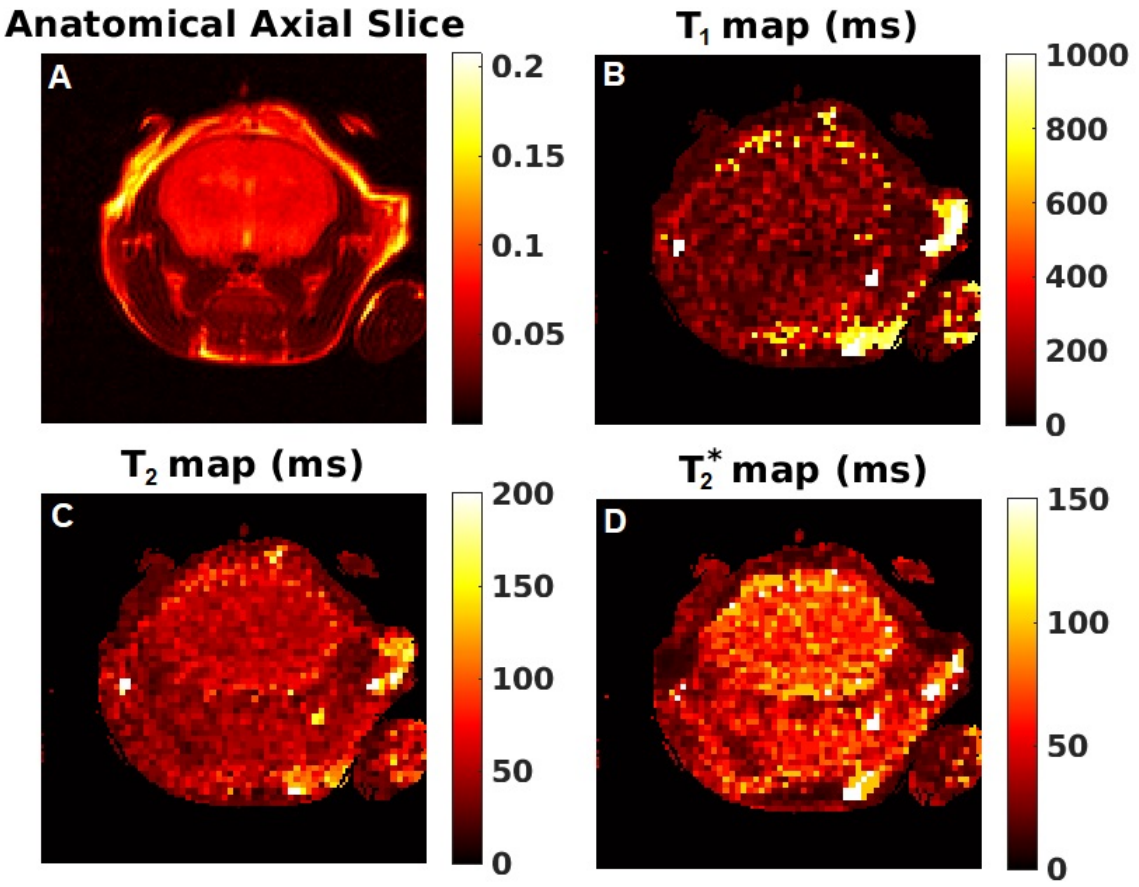

Figure 4.7: C57BL/6 MRF results. A, Anatomical axial FSE of a naïve C57BL/6 mouse. B, C, D, T_1, T_2, and T_2^* maps generated using MRF. A scan of 8 slices covering the mouse brain were performed with 8x undersampling resulting in a scan time of approximately 3 mins per slice or ∼25 min total.

structures (such as the brain).

4.5 Discussion + Conclusions

Simultaneous concentration mapping of two contrast agents is not practical with conventional MRI methods. This is especially true for SPIO, a contrast agent commonly used in cell tracking, which produces a negative contrast that makes quantification challenging. In this study, we have implemented an extension of SSFP-based MRF, allowing the inclusion of R_2^* quantification. This was leveraged to allow simultaneous quantification of two contrast agents: SPIO-labelled CTLs and a Gd agent

(ProHance). Dual quantification of contrast agents could remove the need for multi-modality hardware, and drastically decrease the number of mice required for preclinical studies tracking multiple cell types, offering a crucial tool for increasing efficacy, and decreasing both the temporal and financial cost of said studies.

In our parameter validation tests, CCC values exceeded 0.94 for R_1 and R_2, showing an excellent match between the known and estimated values. These CCC values were comparable to previous *in vivo* MRF studies[124]. While both R_1 and R_2 as generated by MRF showed strong agreement with the conventional values (Fig 4.2A, B) throughout the entire range of tested values, R_2^* quantification demonstrated a small deviation from the known values below 50 s^{-1} and above 100 s^{-1}. Despite this, R_2^* was shown to have the highest robustness to undersampling of all the relaxation rates (Figure 4.4C), with a CCC exceeding 0.988 when 8x retrospectively undersampled. Previous studies have shown that golden angle spiral arm rotation has allowed further increases in undersampling robustness at acceleration factors of up to 48x[97]; however, hardware restrictions prevented validation of this approach using our current system.

As this study represents the first time MRF has been used to quantify R_2^* using pre-clinical hardware, it is difficult to directly compare performance to previous studies. When employing a quadratic RF phase approach in a study using clinical hardware[99], it has been shown that MRF can quantify R_2^* with equivalent fidelity to that seen in R_1/ R_2, in the range of 12.5 - 50 s^{-1}. Likewise, MRF with variable echo times[97] has been used to provide excellent $^{-1}$ matching in the range of 12.5-50 s^{-1}. Currently, the method introduced in this manuscript slightly underestimates R_2^* values below 50 s^{-1}, corresponding to the phantoms containing large amounts of Gd and low amounts of SPIO labelled CTLs. We believe that this is due to the pseudorandom parameter generation not providing sufficiently different dictionary matches for smaller R_2^* values when SNR is low. We are currently looking into parameter regimes for R_2^* values below 50 s^{-1} by including smaller minimum TE and greater overall TE variance to increase sensitivity to both greater and smaller values of R_2^*[97], as an increased dynamic range would help further separate background R_2^* artifacts from labelled cells. It would also further improve the minimum concentration of cells that can be quantified, as seen in Figure 4.5. Importantly, the use of MRF for cellular

tracking of SPIO and other agents requires measurements of relaxation rates larger than required for single-agent detection. Our method demonstrates an increased range of up to 100 s^{-1}, which becomes critical when quantifying SPIO labelled cell populations of ∼10 million cells/mL. Given the small size of cells and the heterogeneous density of recruitment to certain small regions, cellular density can easily be on the order of thousands of cells/mm^3 (corresponding to millions of cells/mL).

MRF literature involving non-Cartesian readouts primarily focuses on clinical application, while studies showing pre-clinical techniques for overcoming respiratory artifacts in mice[125] or overcoming high field effects[126] have opted to use Cartesian trajectories. One study into the use of MRF for dynamic contrast-enhanced studies in mice[124] used a similar spiral trajectory to that used in the present work, achieving similar scan times on the order of 2 minutes per slice.

As mentioned, previous studies have shown that MRF can separate 2 agents administered simultaneously[96] provided this does not include an R_2^* agent. These studies also quantified Gd over a similar range as shown in Figure 4.6C. Our results show an R_2 value of 0.9560 compared to their 0.9987, demonstrating similar performance in both cases. Additionally, R_2^* values in earlier studies were derived from an average of 12 repositions of the phantoms, whereas our R_2^*-adapted dual contrast quantification results are taken from a single scan, to better demonstrate the real-world applicability of the technique.

Previously, it has been shown that SPIO-labelled cells can be quantified using R_2^* values acquired from an SPGR sequence[127]. However, the range of cells quantified was 0.5 – 2.5 million cells/mL, demonstrating a range of 4x less than that of MRF. SPIO-labelled cell quantification has more recently been performed using R_2^* values from a TurboSPI [128] sequence. While cell quantification range is not included in that work, an R_2^* range of up to 1000 s^{-1} is demonstrated. With equivalent cell loading used within our studies, this would yield a theoretical maximum of up to 40 million cells/mL. However, TurboSPI has the drawback of not providing additional parameter maps alongside R_2^*, making it unsuitable for dual quantification. TurboSPI signals can also be contaminated by the presence of fat, which can significantly bias R_2^* quantification[66].

Guided by our *in vitro* results for undersampling, our pilot *in vivo* studies demonstrated that acceleration factors of 8x allow acquisition of 128 × 128 × 8 parameter maps of a C57BL/6 mouse brain within 25 min for 8 slices (3 min per slice). While these preliminary results are promising, with maps corresponding well to the anatomical FSE data provided in figure 4.7A, further studies are required to assess the viability of this technique for *in vivo* dual concentration mapping, especially including a predominantly R_2^* sensitive agent, where susceptibility issues will be substantial compared to similar *in vitro* results.

While a scan time of 25 mins was sufficient for demonstration of *in vivo* parameter mapping, future work aims to further accelerate acquisition time greatly, to prepare for the use of Gd contrast agents. This MRF sequence also provides the as yet unused R_2 parameter maps, which we are in the process of evaluating if addition of R_2 maps into the concentration calculation can improve the robustness of results, potentially allowing for further acceleration.

In conclusion, we have demonstrated that SSFP MRF, expanded to include R_2^* quantification, can be used to simultaneously generate concentration maps of two contrast agents, one of which consists of SPIO-labelled cells *in vitro*. This technique is also able to produce 3D parameter maps *in vivo* in reasonable acquisition times (∼25 mins) for preclinical studies. Simultaneous R_1/R_2^* and concentration mapping provides the future potential for increased molecular information in cellular imaging studies without increased scan times or other modalities, enabling many molecular imaging studies using diverse targeted Gd contrast agents and SPIO cell tracking.

4.6 Supplementary Information

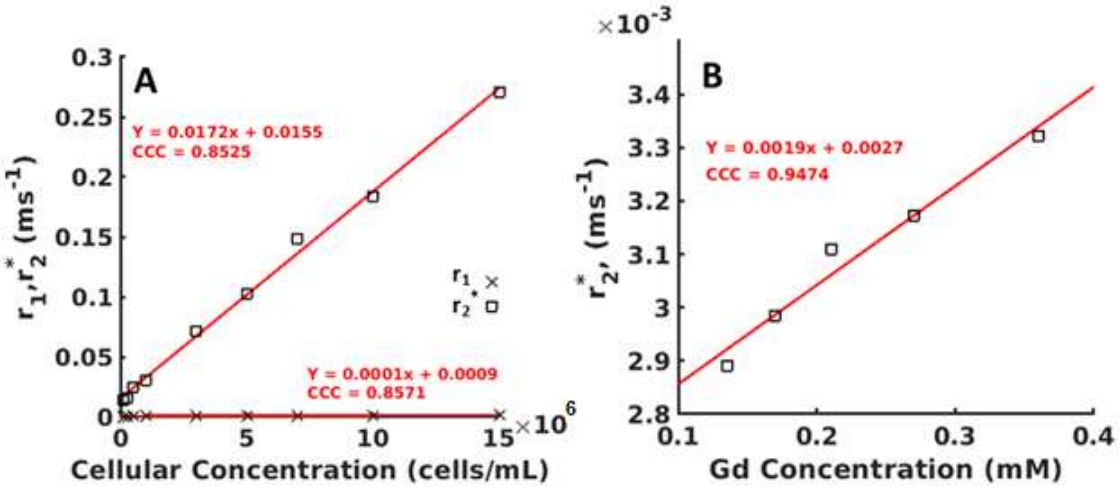

Figure 4.8: Relaxivity calibration result for Gadolinium and iron labelled CTLs. A, r_1 and r_2^* calibration data for iron labelled cells suspended in 4% gelatine. B, r_2^* calibration data for ProHance in 4% gelatine. Equations correspond to the linear regression fit. R_1 measurements were made using an inversion recovery spin-echo sequence, with TI varying from 0.1 to 6.4 s in 7 steps, leading to an acquisition time of 30 seconds. R_2^* values were obtained by linewidth measurements for each phantom separately.

Chapter 5

Sliding-Window Reconstruction for Accelerated MR Fingerprinting with T_2^* Quantification

The contents of this chapter were published in https://doi.org/10.1007/s10334-023-01140-9

5.1 Abstract

Background: MR Fingerprinting (MRF) can enable preclinical studies of cell tracking by quantifying multiple contrast agents simultaneously, but faster scan times are required for *in vivo* applications. Sliding window (SW)-MRF is one option for accelerating MRF, but standard implementations are not sufficient to preserve the accuracy of R_2^*, which is critical for tracking iron-labelled cells *in vivo*.

Purpose: To develop a SW approach to MRF which preserves the R_2^* accuracy required for accelerated concentration mapping of iron-labelled cells on single-channel preclinical systems.

Methods: A nonuniform SW was applied to the MRF sequence and dictionary. Segments of the sequence most sensitive to R_2^* were subject to a shorter window length, preserving the R_2^* sensitivity. Phantoms containing iron-labelled cytotoxic lymphocytes and gadolinium were used to compare 24x undersampled uniform and nonuniform SW-MRF parameter maps. Dual concentration maps were generated for both uniform and nonuniform MRF and compared.

Results: Lin's concordance correlation coefficient, compared to gold standard parameter values, was much greater for nonuniform SW-MRF than for uniform SW-MRF. A Wilcoxon signed-rank test showed no significant difference between nonuniform SW-MRF and gold standards. Nonuniform SW-MRF outperformed the uniform SW-MRF concentration maps for all parameters, providing a balance between R_2^* sensitivity of short window lengths, and SNR of longer window lengths.

Conclusions: Nonuniform SW-MRF improves the accuracy of matching compared to uniform SW-MRF, allowing higher accelerated concentration mapping for preclinical systems.

5.2 Introduction

Contrast agents are routinely used to enhance the ability of MRI to differentiate between healthy and unhealthy tissue, allowing for the detection of pathological changes with high sensitivity, specificity, resolution and penetration[117]. This enables longitudinal *in vivo* studies to collect detailed information on migration patterns of contrast agents, which strengthens molecular imaging studies, particularly those using cell tracking.

MR cellular imaging is already crucial for gathering information on immune cell subsets, and has been used by several groups to follow adoptive transfer of immune cells that are used as a therapy or to track immune cells in disease models, both untreated and treated with immunotherapy agents[119, 109, 120, 38, 129]. While cellular MRI is most commonly performed with iron-based contrast agents due to their high relaxivity, biocompatibility, and ease of cellular labelling[130], contrast agents targeting specific molecular species are becoming more popular to probe a wider range of cellular and molecular targets [109, 120, 12, 121]. Unfortunately, current MR cell tracking techniques are limited to only a single contrast agent tracked at once, greatly limiting the complexity or speed of preclinical studies. Further improvements in efficacy, quantification capabilities, scan times, and financial costs are critical for developing MR cell tracking. Access to simultaneous tracking of two contrast agents has the potential to address these needs.

Magnetic Resonance Fingerprinting (MRF) has been shown to meet the criteria for simultaneous contrast agent imaging[82]. MRF relies on a novel acquisition strategy which provides multiple relaxation maps simultaneously and is highly robust to undersampling, leading to greatly accelerated acquisition times. Previously, it was demonstrated that MRF can provide concentration maps for multiple contrast agents simultaneously, referred to as dual contrast MRF[96]. This was expanded to include R_2^* contrast agents, a critical step in adapting MRF for tracking of iron-labelled cells in preclinical MRI[131]. While that work demonstrated the potential for *in vivo* dual

contrast MRF including R_2^*, it required a scan time of over 400 seconds per slice, which is far too slow to capture the temporal dynamics of many contrast agents, making it logistically unfeasible to use.

A number of traditional and state-of-the-art techniques can be used for MRF acceleration, but many are not accessible in a preclinical setting. For example, a lack of a multichannel RF coil inhibits the use of parallel imaging, and insufficiently sized datasets preclude machine learning-assisted acceleration[132, 133]. *In vivo* dual contrast MRF for use in cell tracking requires additional technical development to produce the required resolution and accuracy in a preclinical setting.

Some techniques remain applicable to preclinical MRF for accelerated acquisition, including novel parameter regimes to lessen the total length of the sequence[113], and 3D acquisition to utilize undersampling in the Z plane[134]. One method of note is the sliding window (SW) reconstruction. Originally proposed for dynamic contrast-enhanced imaging, SW reconstruction offers a method of trading temporal fidelity for improved signal-to-noise ratio (SNR) by combining undersampled subsets of data to produce less undersampled images [135]. SW reconstruction has already been used in MRF studies, and has demonstrated the ability to improve the image quality of reconstructed frames, leading to more accurate fingerprint matching[134] and allowing for motion suppression[136]. However, complications arise when applying this technique to R_2^* sensitive methods. Short window lengths fail to provide enough SNR to highly undersampled MRF preclinical datasets, while application of longer window lengths can lead to greater degradation in the R_2^* sensitivity, necessitating additional care when a SW is applied to preclinical multiparametric MRF.

If MRF is to be fully utilized for MR immune cell tracking, it is vital that acceleration techniques available for a preclinical setting, such as SW, are further improved to include accurate R_2^* quantification. This would allow for dual contrast cellular imaging, including an iron-based contrast agent, on an *in vivo* appropriate timescale. We aim to address this issue by implementing a 'nonuniform' SW to provide higher temporal resolution in the regions of the sequence which are most sensitive to R_2^* changes, enabling higher accelerated quantification of two contrast agents simultaneously, within 80 seconds per slice.

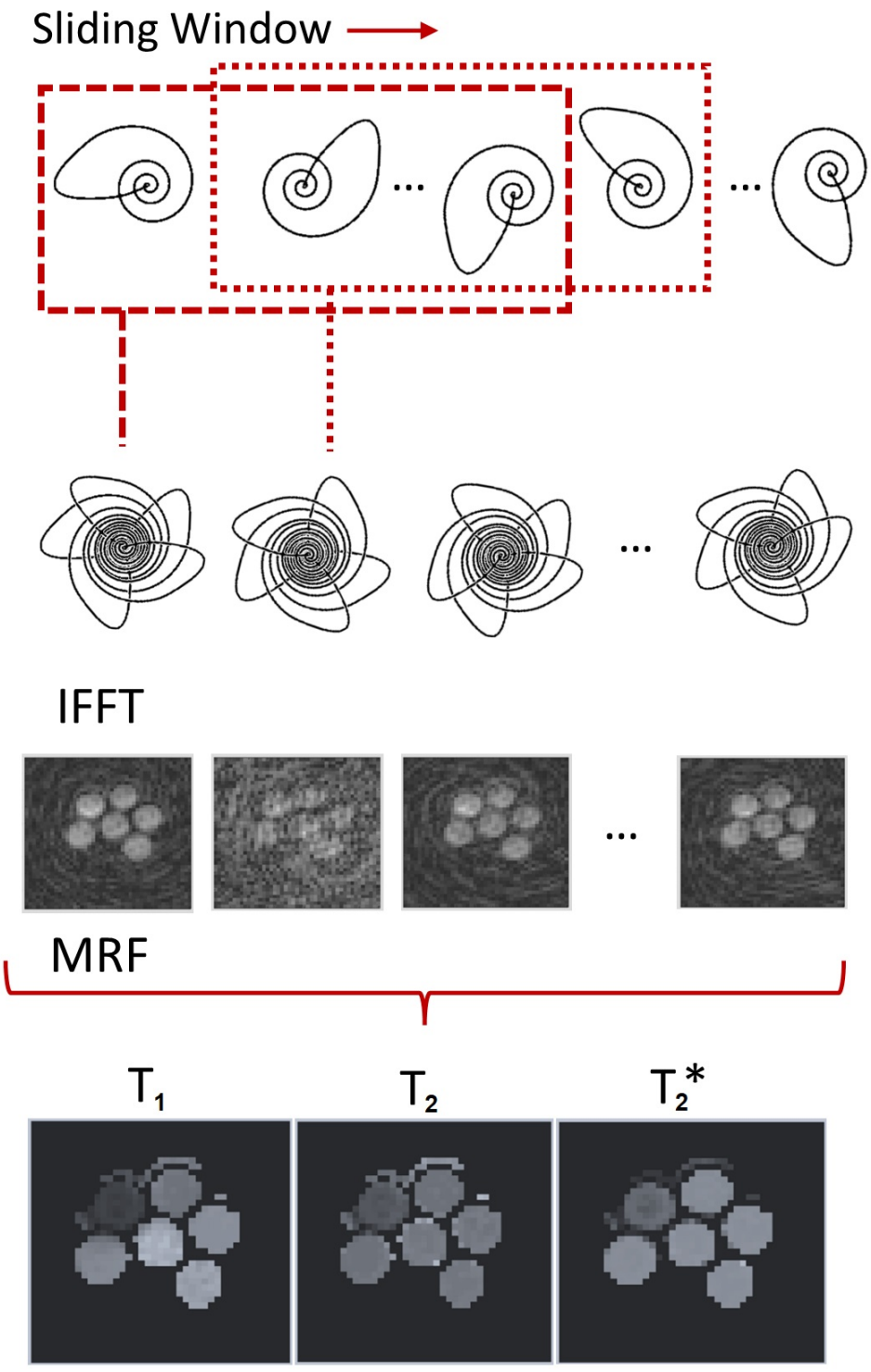

Figure 5.1: Workflow of Sliding Window Reconstruction. Prior to reconstruction via IFFT, individual interleaves are combined. This trades temporal resolution for increased spatial fidelity. When applied to MRF, the same sliding window reconstruction must also be applied to the dictionary.

5.3 Materials and Methods

5.3.1 Pulse Sequence Design

In this work, a non-balanced steady-state free precession (SSFP) sequence is the basis for the MRF acquisition and dictionary, similar to previous implementations of R_2^* MRF[131]. A sinc-shaped slice selection pulse (TBW = 8) is followed by an adiabatic inversion pulse before the imaging frames to improve R_1 sensitivity. TR, TE and flip angle (FA) are varied throughout the sequence's 1000 imaging frames. Three distinct segments of parameter variation are employed to enable R_2^* sensitivity. In the first segment, TR, TE, and FA are held constant, to create a traditional steady-state free precession decay, for a total of 200 imaging frames. The second segment of 400 imaging frames contains Perlin noise varied TR (between 16 and 20 ms) and FA (between 20 and 60°), while TE is held constant at 2 ms. The final section contains a stationary 30° FA, while TE is varied sinusoidally between 5 and 10 ms. While it has been shown that TR variation may be unnecessary for MRF[133], this final section contains TR variation to allow sufficient room for TE variation in the shortest possible acquisition time.

The trajectory for k-space acquisition is a variable density spiral, which fully samples the centre of k-space with 8 interleaves, and the outer region fully within 64 interleaves. Each interleaf samples 923 points with a dwell time of 5 μs. The maximum slew rate and gradient strength are set to 200 T/m/s and 91 mT/m respectively, corresponding to ∼66% of the hardware maximum. Dephasing of at least 2π radians is achieved using a 3 ms crusher gradient between each set of 1000 imaging frames, followed by a 0.5 s delay to relax the spins into thermal equilibrium. Total imaging time per slice is approximately 30 seconds, consisting of 1000 imaging frames with 2 interleaves collected for each frame. Interleaves are rotated by the golden angle between each imaging frame, as well as between each set of 1000 imaging frames. The resulting MRF images have an FOV of 35 mm^2, with a slice thickness of 1 mm, and a matrix size of 64 x 64.

5.3.2 Sliding Window Reconstruction

In our previous work, we demonstrated that single channel MRF with R_2^* sensitivity achieved sufficient image quality for *in vivo* application up to 4x undersampling. For *in vivo* MRF to provide multi-slice imaging in an *in vivo* appropriate timeframe, this must be accelerated to 24x, while providing sufficient data fidelity to still enable dual contrast agent mapping. Preliminary tests suggested that the application of a SW reconstruction improved SNR, but hindered R_2^* quantification.

Sliding window reconstruction for MRF is outlined in Figure 5.1. Prior to inverse nonuniform fast Fourier transform (NUFFT), the k-space data from the individual time frames are combined to produce a new set of k-space data. After reconstruction, each image now represents a wider temporal footprint (and therefore decreased temporal fidelity) but has increased SNR and fewer undersampling artifacts.

The proposed nonuniform SW seeks to optimise MRF to allow for both a higher undersampling factor, and R_2^* sensitivity, for use on a single channel RF coil. This is achieved by maintaining a shorter SW length during the parts of the MR fingerprint which are most sensitive to R_2^*. Figure 5.2A shows the fingerprints of the proposed sequence for a range of R_2^* values, where the final 400 frames of TE modulation encapsulate the R_2^* sensitivity. The proposed method applies a sliding-window similar to previous MRF studies[134], combining a fixed number of consecutive interleaves to generate higher quality images. The length of this window is decreased over the final 400 imaging frames to create a novel, nonuniform SW, trading potential image quality for higher R_2^* sensitivity. This is visually demonstrated in Figure 5.2C. For this work, nonuniform SW refers to a window width W = 6 for the initial 600 frames, and W = 3 for the final 400 frames. This is compared to two different uniform window lengths, W = 3, and W = 6. These window lengths were chosen to demonstrate nonuniform SW's ability to provide a compromise between the high acceleration of long window length, and the R_2^* sensitivity of short window length.

5.3.3 Dictionary Design + Parameter Estimation

The dictionary is based on the extended phase graphing (EPG) framework[85] simulating SSFP sequences without concern for the off-resonance component which would be present in a balanced sequence. Repetition frames were included at the beginning

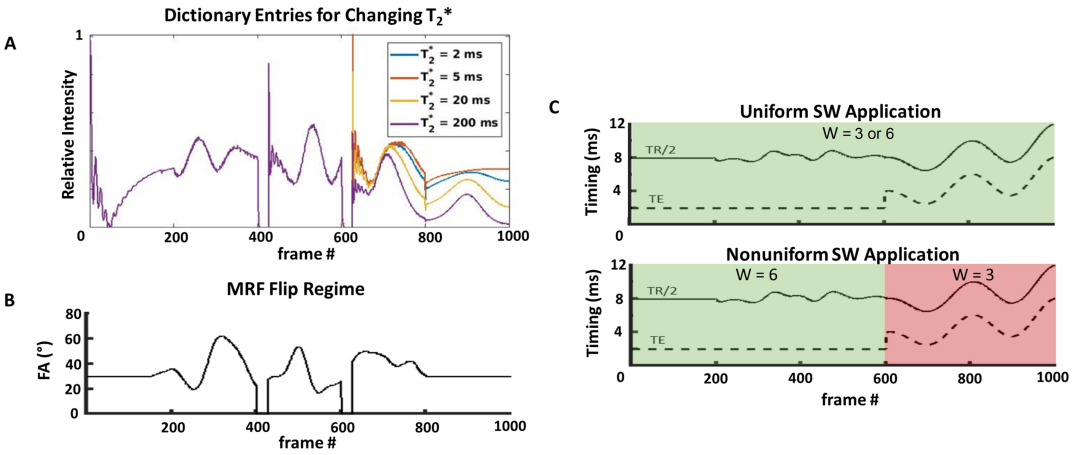

Figure 5.2: A Dictionary entries for fingerprints with different R_2^* values. R_2^* sensitivity is confined to the final 400 frames of the MRF sequence. B Flip angle used for each imaging frame of MRF. C Uniform and nonuniform SW application. Uniform SW application is required to allow for sufficient undersampling of R_2^* MRF to reach preclinically accepted scan times, but impedes R_2^* accuracy at long window length. In nonuniform SW, the final 400 frames (red) are subject to a shorter sliding window length of 3, preserving R_2^* sensitivity while still allowing for higher acceleration factors.

of dictionary simulation to create a steady-state dictionary response, to account for the short delay between individual interleaf acquisition [113]. R_2^* decay is simulated by scaling signal according to the echo time at each imaging frame by exp(-TE/T_2^*). The dictionary entries range in value from T1 = 10 - 4000 ms, T_2 = 5 - 1000 ms, and T_2^* = 1 - 250 ms, all with an increment of 5% per step. Illogical entries were removed, such as entries where $T_1 < T_2$.

After dictionary generation of ∼600,000 entries taking roughly 15 mins, a sliding window is applied to all entries. For uniform SW, W = 3, or W =6 was applied to all 1000 frames. For nonuniform SW, W = 6 was used for the first 600 entries in a fingerprint and W = 3 for the final 400 imaging frames. Since the dictionaries are sparse, they can be subject to singular value decomposition (SVD) without negatively impacting matching capability, as is regularly implemented to reduce the size of MRF dictionaries[137]. With a rank of 25, SVD compresses the dictionary to 2.5% of its original size. Sliding window and SVD dictionary processing take approximately 1 hour. Reconstruction and matching were performed in MATLAB (The MathWorks; Natick, MA), on a virtual machine with 200 GB memory and 24 CPUs running on a

Linux enterprise cluster. R_1, R_2, and R_2^* maps are generated using a traditional MRF pipeline[10], matching the maximum dot product between a voxel and the dictionary.

5.3.4 Phantom Evaluations

All experiments were performed on a 3T preclinical system (Agilent, Santa Clara, CA), with a quadrature RF coil. Phantoms consisting of 8% gelatin and cytotoxic lymphocytes (CTLs) labelled with a range of ProHance (Gadoteridol; Bracco Imaging) and/or Molday ION Rhodamine B SPIO (BioPal Inc., Worchester, Massachusetts, USA) were prepared in 5 mm NMR tubes, with concentrations chosen to mimic the parameter range of expected future *in vivo* scans. These concentrations can be found in Table 5.1. CTL isolation was done using the same procedure as in previous R_2^* MRF literature[131]. Gold standard R_1, R_2, and R_2^* values were obtained to validate the proposed modifications to SW-MRF. R_1 values were obtained using a multi-TI inversion recovery sequence (TI = 0.05, 0.01, 0.02, 0.4, 0.8, 1.6, 3.2s, 64 x 64, 1 mm slice thickness). R_2 was generated using a CPMG sequence, with ETL = 10, echo spacing = 33 ms (64 x 64, 1 mm slice thickness). R_2^* values were obtained by measuring the linewidth of individual samples with a non-spatially resolved hard pulse and using the relation $R_2^* = 1/(\pi$ x linewidth). Averages of the centre 3 x 3 voxels of the MRF parameter maps were measured and compared to the gold standard values using Lin's concordance correlation coefficient (CCC) in order to express a quantifiable representation of the deviation from the gold standard for uniform sliding window lengths, and for the proposed nonuniform sliding window approach. Wilcoxon signed-rank tests were used to examine the distributions of the relaxation parameters computed with SW-MRF and those calculated from the gold standard measurements, with $p < 0.05$ representing a significant difference in the means of the distributions.

MRF parameter maps were used to generate dual concentration maps for both contrast agents, via an expansion to the linear relaxation model [96, 131].

$$R_1 = R_{1,0} + r_{1A}[A] + r_{1B}[B] \tag{5.1}$$

$$R_2^* = R_{2,0}^* + r_{2A}^*[A] + r_{2B}^*[B] \tag{5.2}$$

Phantom	1	2	3	4	5	6	7	8	9	10	11
Gad (mM)	0.45	0.4	0.35	0.3	0.2	0.1	0	0.2	0	0.2	0.4
cells/mL	0.125	0.25	0.5	1.25	3.75	6.25	0	1.25	1.25	7.5	7.5
T_1 (ms)	299	312	357	416	474	551	1514	523	1287	393	271
T_2 (ms)	259	270	254	212	113	78	1074	214	282	79	71
T_2^* (ms)	140	105	109	96	104	74	230	95	102	78	70

Table 5.1: Composition of the phantoms used in the study. Gold standard parameter measurements are included for each phantom. Cells are in units of x10^6/mL

where R_1/R_2^* are the reciprocal of T_1/T_2^*, $R_{1,0}/R_{2,0}^*$ are the values of R_1/R_2^* without contrast added, measured from phantom 7 using MRF. [A] and [B] are the concentrations of iron-labelled cells or ProHance, r_{1A} and r_{2A}^* are the magnetic relaxivities of the iron-labelled cells, and r_{1B} and r_{2B}^* are the magnetic relaxivities of ProHance. Calculation of these values is provided in the supplementary material of our previous publication[131]. This was performed for both a uniform window length of 6, and the proposed nonuniform window length. 3 x 3 voxel averages of the MRF-produced concentration maps were extracted, with CCC used to evaluate the performance of both uniform and nonuniform SW-MRF with respect to the known concentration values of contrast agents.

5.4 Results

5.4.1 Parameter Validation

Figure 5.3 shows the resulting relaxation rate maps for highly undersampled SW-MRF with different SW regimes, compared to known values. The images for known values were generated using the gold standard average measurements, and as such do not convey the variation within the phantoms, which on the order of 2% for R_1 and R_2 and 5% for R_2^*. Here the relaxation rates are mapped, to provide a better visualization of the dynamic range present. Visual inspection of the parameter maps for the uniform SW-MRFs show that parameter variation is not accurately captured when compared to that of the known values, specifically for R_1 and R_2 for the shorter uniform window length, and R_2 and R_2^* for a longer uniform window length. Conversely, nonuniform SW-MRF demonstrates parameter changes between phantoms much closer to that seen in the gold standard. Overall, a sliding window length of 6 leads to a less noisy

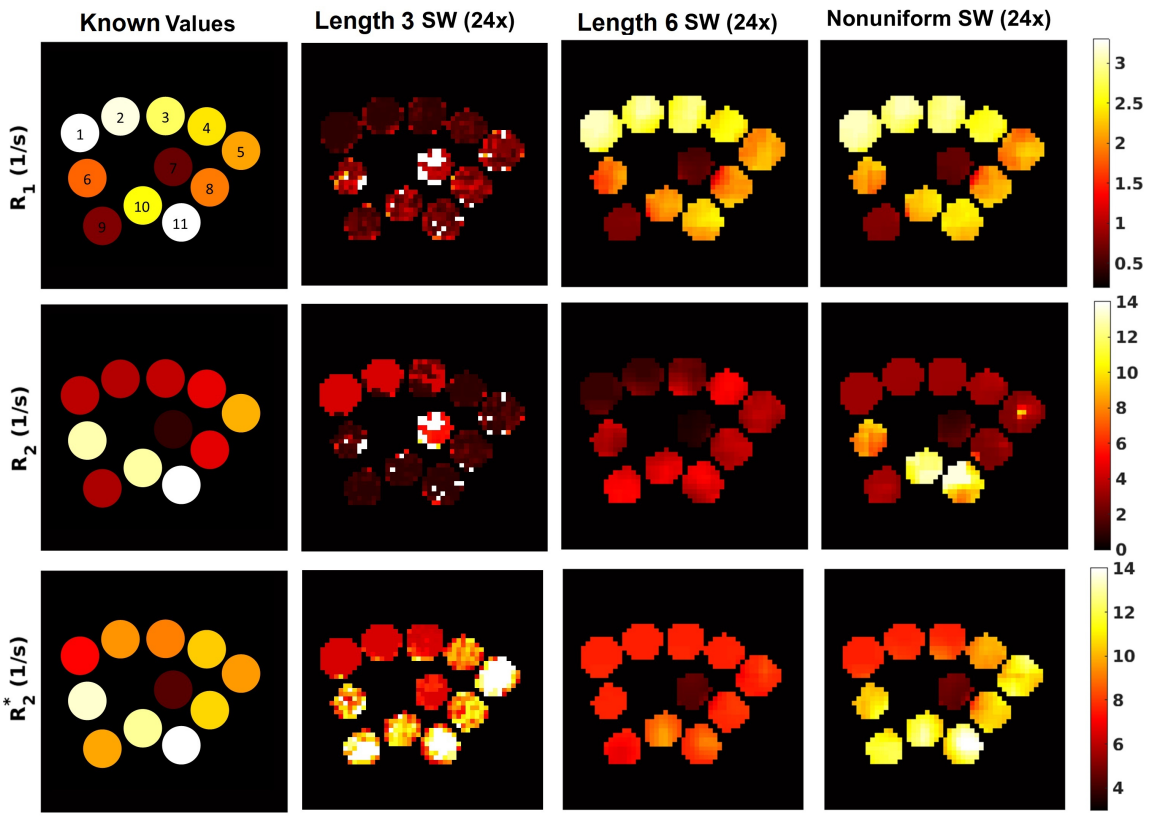

Figure 5.3: 3 Comparison between known parameter values (far left column), 24x undersampled uniform SW for a window length of either 3, and 6 (middle columns) and 24x undersampled nonuniform SW (far right column) MRF. Phantom numbers refer to Table 5.1 for the composition and gold standard parameter values of each phantom.

parameter map but hinders R_2^* sensitivity.

Figure 5.4 shows the comparison between the gold standard parameter values of each phantom to the 3 x 3 voxel average of the uniform and nonuniform SW-MRF. For R_1, SW = 3 fails to capture the correct values, but both the SW = 6 and nonuniform SW perform well, with almost every phantom matching the gold standard R_1 values. The one exception is phantom 11, which contains the highest concentration of both contrast agents, and therefore the highest R_1 value. For R_2 and R_2^*, the SW = 6 fails to capture the full dynamic range required for accurately mapping the phantoms with higher concentrations, in both cases underestimating the phantoms with R_2/R_2^* values of 10 s^{-1}. SW = 3 has similar difficulties quantifying R_2, but outperforms a longer SW length for evaluating R_2^*, despite producing parameter maps with more noise.

2a

CCC	R_1	R_2	R_2^*
SW = 3	-0.1115	-0.2181	0.6669
SW = 6	0.8801	0.2723	0.3482
Nonuniform SW	0.8803	0.8837	0.8776

2b

Wilcoxon Signed Rank Test	R_1	R2	R_2^*
SW = 3	0.0047	0.0322	0.6301
SW = 6	0.2402	0.5195	0.0049
Nonuniform SW	0.7002	0.7646	0.8311

2c

Lin's CCC	Gad Conc	Cell Conc
SW = 6	0.902	0.4666
Nonuniform SW	0.8874	0.8226

Table 5.2: 2a Lin's CCC values for Figure 5.4. b Wilcoxon signed rank test results between the gold standard parameter values, and uniform/nonuniform phantom data in Figure 5.4, where p<0.05 represents a significant difference in the distributions. c CCC values for the agent concentration data in Figure 5.6B

Nonuniform SW outperforms both uniform sliding window lengths for both R_2 and R_2^*. Table 2.a shows the CCC values associated with Figure 5.4 which align with these findings. Table 5.2.b shows the Wilcoxon signed rank test results between the uniform and nonuniform SW results from Figure 5.4, where nonuniform SW parameters are shown to not significantly differ from the gold standard, unlike SW = 6 R_2^* and SW = 3 R_1/R_2, where $p < 0.05$.

5.4.2 Concentration Validation

Figure 5.5A contains the results for concentration maps produced by MRF. Both SW = 6 and nonuniform SW-MRF perform Gd concentration mapping well, with results visually resembling the known concentration values. This is supported in Figure 5.5B, where the inner 3 x 3 voxels of each phantom are compared to the known values of concentration, and are both found to have strong concordance correlation coefficients of 0.902 and 0.8874 for uniform and nonuniform SW-MRF respectively. SPIO-labelled cell concentrations are also mapped in Figure 5A, and display a visible difference between the produced maps for both SW = 6 and nonuniform SW-MRF. Similar to R_2^* parameter mapping, uniform SW-MRF fails to accurately estimate the higher

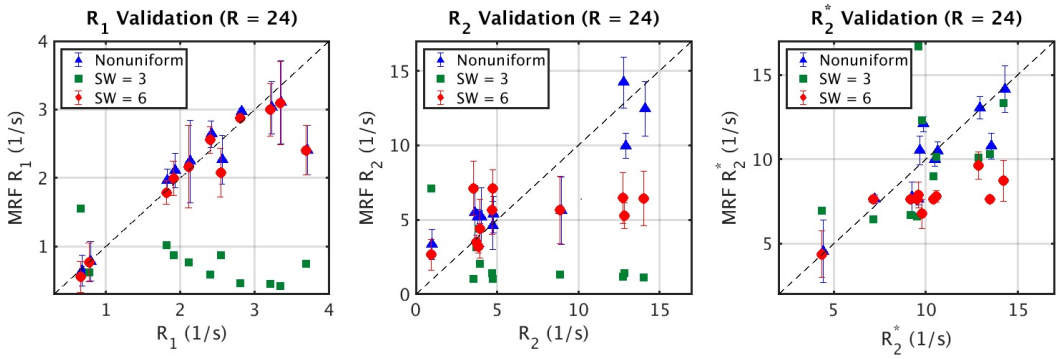

Figure 5.4: Comparison of the gold standard values for each phantom, compared with the average over a 3x3 voxel ROI taken from the nonuniform SW-MRF (triangle), uniform SW =6 MRF (circle), and uniform SW = 3 MRF (square). Note that the SW = 3 error bars were very large due to the increased noise, and were removed for clarity.

values of cell concentration, while nonuniform SW-MRF more closely represents the known values. Figure 5.5B shows that uniform SW-MRF fails to characterise phantoms above 2 million cells/mL, demonstrating the effect of inaccurate R_2^* mapping on cell concentration estimations. Nonuniform SW-MRF, while showing a tendency to slightly overestimate cells in the 2 - 4 million cells/mL range, provides a much more robust scaling into the higher values of cell concentrations. CCC values for SPIO labelled cells support these findings, with values of 0.4666 and 0.8311 for uniform and nonuniform SW-MRF respectively.

5.5 Discussion

In this study, we have demonstrated why care must be taken in the application of sliding window reconstruction to MRF, and shown that introducing a nonuniform sliding window length in the R_2^* sensitive regions of an MRF sequence can enable dual contrast quantification within an acceptable *in vivo* timeframe on single channel preclinical systems.

The parameter validation results demonstrate that the nonuniform SW-MRF modifications improve the results for all parameter maps, combining the R_1 and R_2 accuracy of larger sliding window lengths, and the R_2^* sensitivity of shorter window lengths. This is visually apparent from the parameter maps, where SW = 6 clearly

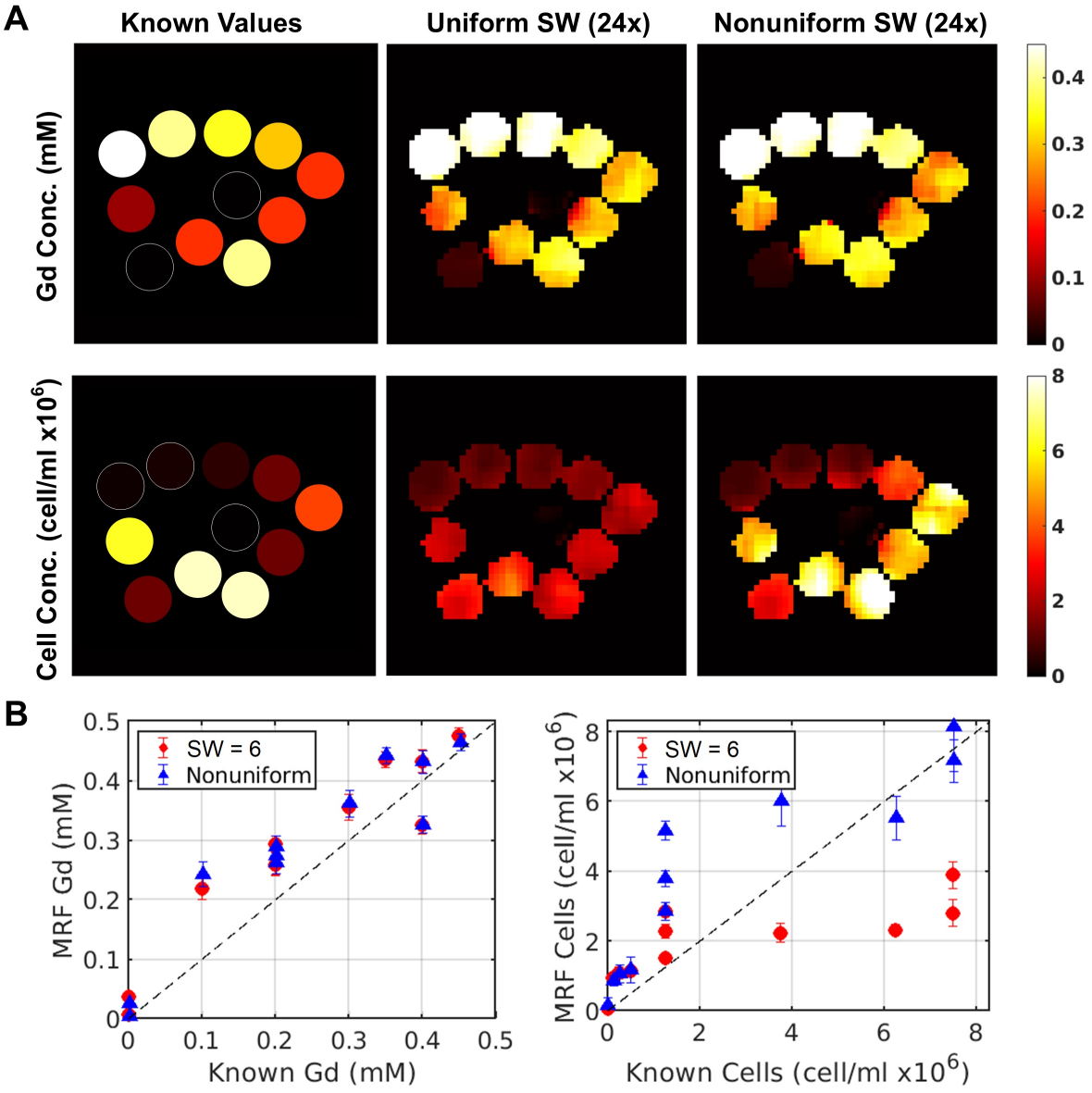

Figure 5.5: A, Dual concentration maps generated using SW-MRF. B, Comparison of the known values for each phantom, compared with the average over a 3 x 3 voxel ROI taken from SW = 6 MRF (circle) and nonuniform SW-MRF (triangle). SW = 3 concentration mapping is not included, as concentration maps were unable to be generated from the data.

lacks R_2 and R_2^* accuracy when compared to the known values, but offers improved robustness to the undersampling noise seen with SW = 3, with nonuniform MRF providing a balance between. For SW = 3, the shorter window length is unable to overcome the high undersampling factor noise, but is still able to provide R_2^* sensitivity, most likely due to the prominence of signal decay based on R_2^* dephasing. Conversely, SW = 6 underestimates either R_2, R_2^*, or both, suggesting that longer window length uniform SW-MRF cannot accurately capture R_2 and R_2^* dynamics, most likely due to the window length 'smearing' the R_2^* signal effects over more imaging frames. As higher R_2^* are typically present in studies involving iron-loaded cells, this highlights the need for optimisations such as the one proposed in this work.

The non-iterative nature of a SW acceleration approach means that no prior information is required for application, and that post processing time is barely affected. This study shows that SW-MRF can enable a 24x increase in acquisition speed with minimal effect on data fidelity, while also leaving R_2^* sensitivity intact. The scan time of fully sampled MRF data using our current protocol is around 28 minutes without SW. This may be accelerated via 4x undersampling to 400 seconds without compromising parameter map quality for either uniform or nonuniform MRF, but in this work we have demonstrated that nonuniform SW-MRF can further reduce this value to 80 seconds per slice.

CCC values for uniform and nonuniform SW-MRF can be found in Table 5.2.a. For every parameter, the nonuniform SW-MRF was found to consistently outperform both SW = 6 and SW = 3 MRF, with R_2 and R_2^* showing increases from 0.2723 to 0.8837 and from 0.3482 to 0.8776 respectively when compared to SW = 6, and all values increasing when comparing nonuniform SW MRF to SW = 3. The only CCC which was not dramatically increased is SW = 6 and nonuniform R_1 parameter maps, which is due to SW = 6 already performing well for R_1 parameter measurement. We suspect that R_1 sensitivity is maintained for longer window lengths due to the effects occurring over a longer time-scale than R_2 or R_2^*, lessening the effect of combining imaging frames. Overall, these results demonstrate nonuniform SW-MRF's ability to strike a balance between the two uniform regimes. Wilcoxon signed rank test results support this conclusion, showing that while SW = 6 R_2^* and SW = 3 R_1/R_2 averages differ significantly from the gold standard results, nonuniform SW does not.

While a previous study on SW-MRF[94] showed that uniform SW enables accelerating MRF with accurate R_1 and R_2 measurements, this study highlights important cases in which additional care may be required. Firstly, due to the way all parameters are dependent on each other in the generated dictionary and its contained fingerprints, inaccuracies in one parameter permeate into all others. It is likely that the errors seen in this study for R_2 for the uniform SW = 6 MRF should be taken not as a demonstration of how poorly uniform MRF performs for these parameters, but rather how the presence of R_2^* contrast damages uniform SW's ability to accurately accelerate MRF in general. An example of this can be seen with phantoms 7 and 11 in Figure 5.3. Phantom 7 contains no SPIO labelled cells, whereas phantom 11 contains the highest concentration, leading to a much higher R_2^*. Here we see that uniform SW cannot accurately measure R_2^* in phantom 11, leading to underestimates in R_2, but has no problem measuring the R_2 without the presence of a R_2^* contrast agent. Nonuniform SW can more accurately measure R_2^* in phantom 11, and as a result, R_2 measurements are restored. Secondly, this study focuses on utilization of highly undersampled MRF on a single channel preclinical system, as well as imaging in the presence of iron. Thus, SNR is limited, which most likely accounts for SW = 3 MRF being unable to provide accurate R_1 and R_2 parameter maps.

Concentration mapping data shows the clearest support for nonuniform over uniform SW-MRF, with SW = 6 MRF failing to capture the range of cell concentrations within the phantoms. Indeed, if not for the strong r_1 relaxivity of the gadolinium agent, uniform SW-MRF would have most likely struggled to quantify both agents in the presence of R_2^* . A different agent such as manganese would be less reliant on R_1 mapping for concentration calculations and would likely be more challenging to quantify alongside SPIO. Nonuniform SW-MRF, however, was able to provide accurate dual contrast parameter maps even at 24x undersampling. SW = 3 MRF concentration mapping performed so poorly due to noise that we were unable to produce concentration maps of any value.

While nonuniform dual contrast SW-MRF does have a tendency to overestimate concentration values within the range of 2 – 6 million cells/mL, it still greatly outperforms SW = 6 uniform MRF over the entire range of cell concentrations mapped,

having nearly double the CCC value. One source of error may be the phantoms themselves, in which accurate concentration values are difficult to ascertain, with iron cell loading varying anywhere from 3-5 pg/cell even within homogeneous cohorts. There may also be non-homogeneous distributions of cells within phantoms despite efforts to homogenize them. Therefore, there is inherent error in the x-axis of Figure 5.5B which cannot be quantified. For this reason, the individual points are less valuable than the trend showing that measurement of cell concentration is applicable over a large range, with a well-defined minimum level of detection. B1 mapping corrections were not applied to any of the MRF sequences performed, which has been previously shown to directly impact the quantification errors in parameter mapping[91]. We suspect that adding B1 mapping corrections to the MRF workflow will therefore lead to increased accuracy for future SPIO labelling studies. Similarly, the EPG model used for this work does not employ a slice selective EPG (ssEPG) dictionary, which would allow for greater accuracy in modelling both slice-excitation and imperfect spoiling gradients[138]. However, we expect the lack of ssEPG and and B1 corrections to affect both nonuniform and uniform SW MRF equally, and therefore would not affect the comparison between the two. Another potential source of error is using a variation in TR to drive the non-steady state of the MRF sequence. Future optimisations for nonuniform SW MRF could include minimizing the TR variation to provide a minimum amount of incorrect phase accrual, as well as employing an ssEPG and B1 mapping to improve quantification accuracy.

For this study, emphasis was placed on cell concentrations in the <1 million cells/mL range, to provide greater characterisation of the minimum cell concentrations detectable, but future studies may benefit from further probing the $2-6$ million cells/mL region. While slightly overestimated, this study demonstrated detection of cell concentrations as low as 125,000 cells/mL, which is lower than cell densities seen in some previous *in vivo* studies[38].

It is important to note that for the most accurate parameter maps, MRF images would be required both prior to and after the introduction of contrast agents. While the intended use for dual contrast SW-MRF involves *in vivo* applications, which would allow for such data to be collected, for *in vitro* data we must rely on a simulacrum of pre-contrast data in the form of a phantom with zero contrast. As such, we see

variation within each phantom, particularly in phantoms 6 and 11, but this is not something we expect to be a factor in future *in vivo* studies.

In this study we used a fixed ratio of 2 for the sliding window length between the R_2^* sensitive (W=3) and non-R_2^* sensitive (W=6) areas of the MRF sequence. This value was empirically chosen in an attempt to compromise between preliminary SW = 3 and SW = 6 results, in the hope of restoring R_2^* sensitivity. While it is beyond the scope of the current study, further investigation into the effect of window ratio on parameter accuracy could further optimise nonuniform SW-MRF.

5.6 Conclusions

In this study, the sliding window reconstruction strategy for MRF has been expanded to include a novel nonuniform window length. While the existing SW methodology provided a means to improve the SNR and reduce undersampling artifacts in MRF data, this has proven insufficient for use on single channel preclinical systems, compromising parameter accuracy. By lowering the window length during the R_2^* sensitive areas of the MRF sequence, it has been demonstrated the nonuniform SW-MRF increases the accuracy of all parameters in the presence of R_2^* contrast *in vitro*, leading to more accurate concentration maps for contrast agents. This acceleration optimisation is critical for any preclinical application of MRF which hopes to use SW as an acceleration technique to measure samples with a R_2^* contrast, such as time-sensitive *in vivo* experiment in which iron is used to label cells of interest.

Chapter 6

In vivo Dual Quantification of Contrast Agents using MR Fingerprinting

6.1 Introduction

In Chapter 4, MRF has been shown to meet the requirements to overcome the single contrast agent limitation for MRI studies by utilizing highly customizable parameter variation to include T_2^* sensitivity. This sequence was extended upon in Chapter 5, where MRF's robustness to undersampling was utilized to greatly accelerate imaging times without compromising its dual contrast agent mapping potential, by employing nonuniform sliding window reconstruction. The next step is to demonstrate that SW-MRF can produce dual contrast agent parameter maps *in vivo*, a critical tool for optimizing preclinical studies where multi-slice imaging is required on a cohort of specimen over several days. In this chapter, we build on the developments previously presented in this thesis in an attempt to demonstrate dual contrast MRF *in vivo*.

In vivo validation of a sequence which provides quantification is an important step, and for quantification of contrast agent concentration mapping, also a difficult one. Validation of agent concentration requires accurate positional information on quantities of metals which fall far below detection limits of many non-MRI methodologies. One technique which can circumvent this issue is immunohistochemistry(IHC), which allows for accurate positional mapping, but requires appending agents with florescence tags. While IHC samples required for full dual contrast validation are collected during Chapter 6, the results of an IHC study were not made available prior to the completion of this thesis.

However, with the appropriate techniques, we can still gain insight into the predicted deposition profiles of two contrast agents measured simultaneously with MRF. While the deposition of macrophages around glioblastoma is not well defined, and indeed this is exactly why development of such a technique is critical, we do know some

of what *shouldn't* be visualised in a macrophage concentration map. Namely, central tumour regions should be free of contrast agents due to necrosis, and deposition is likely to be clustered rather than spread throughout the brain region. Analysis of concentration maps of contrast agents can therefore assist in our understanding of immune cell population behaviours within the brain, as well as demonstrate the feasibility of dual contrast MRF sequence in *in vivo* studies.

6.2 Experimental Design

A study was designed to demonstrate SW-MRF for *in vivo* application using a glioblastoma model. This was chosen because concentration mapping requires datasets taken both prior to and 24 hours after injection of an iron contrast agent, and rigid coregistration is far more accurate in a mouse brain than the flank.

In vivo experiments were performed using eight 6-week-old female C57BL/6 mice implanted with a glioma-261 cell line. Mice were anaesthetized using isoflurane, and stereotactic surgery is performed, drilling 0.1 mm into the skull without disrupting the dura. A needle is then mechanically lowered to a depth of 2.3 mm through the opening, where the cells are slowly injected. All experiments involving mice were carried out in accordance with ethics protocols approved by the University Committee on Laboratory Animals at Dalhousie University, Halifax, N.S., Canada.

Mice were separated into 2 groups, 6 in group 1, and 2 in group 2. The purpose of group 2 was to be frozen for later immunohistochemistry (IHC) to allow for further validation via localization profiles of the contrast agent deposition at a later date.

All mice were imaged using a T_2-weighted FSE sequence (TE = 60 ms, TR = 200 ms, FOV = 20 x 20 mm, 16 echoes, 16, slices, 7.5 ms echo spacing, 96 x 96, 20 mins) and T_2^* MRF (16 slices, FOV = 20 x 20 mm, 96 x 96, 20 mins) at 28 days post surgery. After the first set of scans, each mouse received an iron injection of 200ul of SPIO Rhodamine B (68 μL SPIO, 132 μL saline. 6.8 mg/kg)(Biopal) and both FSE and MRF imaging was repeated 24 hours later. 20 minutes prior to the MRF scans, group 1 received an injection of MultiHance (40 μL MultiHance, 150 μL saline, 1 g/kg)(Bracco), and group 2 received an injection of Glowing Galbumin - Fluorescein (100 μL Galbumin, 100 μL saline, 125 mg/kg)(Biopal) to coincide with future IHC preparation. This timeframe was chosen as gadolinium clears within a few

minutes from the bloodstream, and so the only gadolinium contrast agent remaining will be caused by leaky vasculature present near tumour. Two mice did not receive a gadolinium and iron agent respectively, acting as single agent controls. Full details of the contrast agents received by mice can be seen in Table 6.1. Following completion of scans, mice were terminated. Group 1 brains were isolated and digested using a combination of mechanical and biological dissociation, include lysis of the red blood cells. Once brains were completely digested, any remaining tissues was digested in nitric acid for 48-72 hours at 37 °C. Samples were then sent for ICP-MS processing. Group 2 mice brains were bathed in a sucrose:OCT solution, flash frozen in liquid nitrogen, and stored long term in a -80 °C freezer for future IHC analysis.

Mouse ID	Iron Agent	Gadolinium Agent
G1A_1	SPIO Rhodamine B	N/A
G1A_2	SPIO Rhodamine B	MultiHance
G1A_3	SPIO Rhodamine B	MultiHance
G1A_4	SPIO Rhodamine B	MultiHance
G1B_1	N/A	MultiHance
G1B_2	SPIO Rhodamine B	MultiHance
G2_1	SPIO Rhodamine B	Fluorescein
G2_2	SPIO Rhodamine B	Fluorescein

Table 6.1: Mice used for the *in vivo* experiment as well as which contrast agents they received. G1 and G2 differ by which type of gadolinium agent they received, with G2 receiving a gadolinium agent tagged with fluorescence for a future localization study using IHC and fluorescent microscopy. G1A_1 and G1B_1 did not receive a gadolinium and iron agent respectively, acting as single agent controls. The only difference between G1A and G1B was the scan day, as the imaging facility is limited by the throughput of mice per day.

6.2.1 Pulse Sequence Design

In this study, the MRF sequence is based on a non-balanced steady state free precession (SSFP) sequence, similar to previous T_2^* implementations[131]. T_1 sensitivity is improved by inclusion of an adiabatic inversion pulse at the beginning of the sequence. Non-steady state evolution of the MRF signal is created with variation in TR, TE, and flip angle (FA). In this implementation, 3 distinct sections of the MRF regime

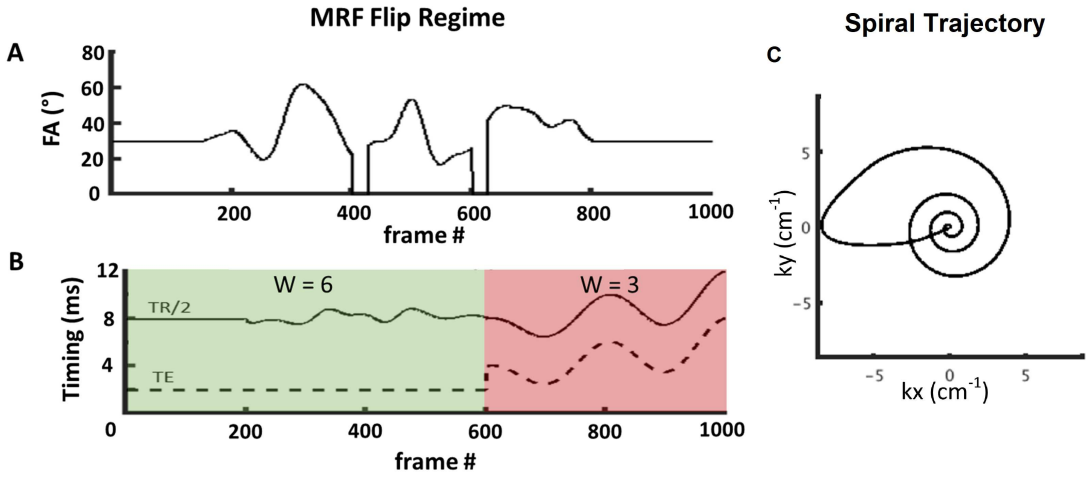

Figure 6.1: A) MRF *in vivo* sequence configuration B) TR and TE for each imaging frame, and visualization of the sliding window prescription used. The final 400 frames (red) are subject to a shorter sliding window length of 3, preserving T_2^* sensitivity while still allowing for higher acceleration factors. C) Variable density spiral for one interleaf.

are created. In the first, lasting 200 imaging frames, TR, TE, and FA are held constant to simulate traditional steady state. The second segment follows a traditional MRF sequence perturbation, with Perlin noise varied TR (between 16 and 20 ms) and FA (between 20 and 60°), and a constant TE of 2 ms. The final section contains sinusoidal TE variation, while FA is held stationary. In this final section, TR is also varied, but this is to allow for longer TE variation only. These sequence parameters are identical to those used in the previous chapter.

A variable density spiral was used during acquisition, which fully sampled in the centre of k-space within 8 interleaves, and the outer region fully within 64 interleaves. Dephasing of at least 2 pi radians is achieved using a 3 ms crusher gradient between each set of 1000 imaging frames, followed by a 0.5 s delay to relax the spins into thermal equilibrium. Each imaging frame had an undersampling factor of 16x, collecting 4 interleaves. Each interleaf samples 923 points with a dwell time of 5 us, and are rotated by the golden angle between each imaging frame, as well as between each 1000 image frame set. The maximum slew rate and gradient strength are set to 200 T/m/s and 91 mT/m respectively, corresponding to 66% of the hardware maximum. Total imaging time per slice is approximately 1 minute.

6.2.2 Dictionary Design and Parameter Estimation

The dictionary used was based on extended phase graphing, allowing for simulation of with SSFP sequence. Dictionary entries began with repetition frames to create a steady-state dictionary response, improving T_1 matching accuracy and accounting for the short delay between individual interleaf acquisition. The dictionary entries ranged in value from T_1= 10-4000 ms, T_2= 5-1000 ms, and T_2^* = 1-250 ms, all with an increment of 5% per step, with Illogical entries removed, such as entries where $T_1 < T_2$. T_2^* decay was simulated by scaling signal according to TE at each imaging frame by exp(-TE/T_2^*). Nonuniform sliding window was applied to MRF data prior to dictionary matching, the first 600 frames to a window length of 6, and the final 400 frames a window length of 3. This was added to improve image quality without compromising T_2^* sensitivity as seen in the previous chapter. Both the resulting data and the dictionary were subject to a rank-25 singular value decomposition (SVD), greatly accelerating match times while having practically no impact on results with an appropriately chosen rank value[16]. The resulting SVD dictionary were decreased in size by 97.5%. Reconstruction and matching were performed in MATLAB (The MathWorks; Natick, MA), on a virtual machine with 200 GB memory and 24 CPUs running on a Linux enterprise cluster. T_1, T_2, and T_2^* maps were generated using a traditional MRF pipeline, matching the maximum dot product between a voxel and the dictionary.

6.2.3 Concentration Maps

Prior to generating concentration maps, FSE anatomical images are used to best align the pre and post image axial slices, then an iterative image coregistration algorithm automatically aligns each slice. This algorithm is provided within the MATLAB (The MathWorks Inc) imaging toolbox, and for this implementation only utilized translational and rotational coregistration. MRF parameter maps are then used to generate dual concentration maps for both contrast agents, via an expansion to the linear relaxation model

$$R_1 = R_{1,0} + r_{1A}[A] + r_{1B}[B] \tag{6.1}$$

$$R_2^* = R_{2,0}^* + r_{2A}^*[A] + r_{2B}^*[B] \tag{6.2}$$

where R_1,R_2^* are the reciprocal of T_1,T_2^*, $R_{1,0}$,$R_{2,0}^*$ are the values of R_1,R_2^* from the pre-contrast images. [A] and [B] are the concentrations of iron-labelled cells or MultiHance, r_{1A} and r_{2A}^* are the magnetic relaxivities of the SPIO Rhodamine B, and r_{1B} and r_{2B}^* are the magnetic relaxivities of MultiHance. Relaxivity values for MultiHance were taken from literature values at 3T in human blood plasma [139]. SPIO Rhodamine B values were derived from our assays performed on iron labelled T cells, assuming a cell load of 3pg/cell. Following this, masking is applied to the concentration maps to remove spurious data outside the brain. These maps were then threshholded to the same values for all maps. These values were chosen by visual inspection of the concentration maps.

Total values for both SPIO Rhodamine B labelled macrophages and Gadolinium were calculated for each mouse brain. To assess agent deposition, the total number of clusters were calculated for each agent in each mouse. A cluster was defined as a group of voxels of a given contrast agent which are directly bordering each other in 3 dimensions. For this implementation, a voxel was said to be bordering the 26 surrounding voxels in 3D. This can be visualized by imagining a 3 x 3 Rubik's cube, where all individual pieces would be considered to be bordering a voxel in the centre of the cube. The average size of clusters (in voxels) for each agent within each mouse was also calculated.

6.3 Results + Discussion

6.3.1 Parameter Maps

Figure 6.2 demonstrates an example of the ΔR_1 and ΔR_2^* parameter maps generated by the MRF pipeline. Colour axes have been fixed to the same values for the sake of comparison. Change in parameter was chosen to be shown here, as this is the specific form of R_1 and R_2^* that is used for dual contrast concentration quantification in Equation 6.1.

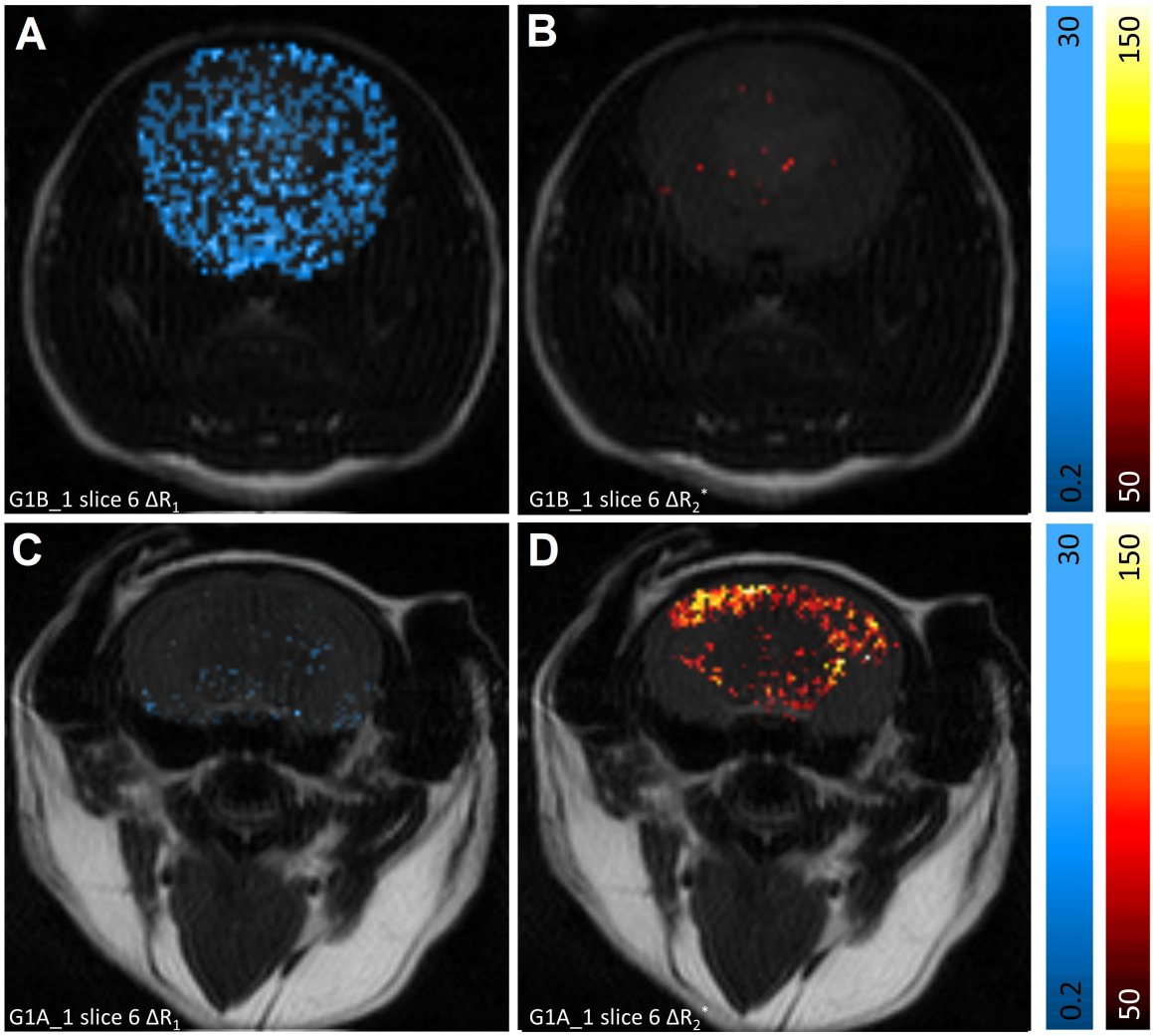

Figure 6.2: Relaxation rate maps for mice which received only 1 contrast agent. A, B) ΔR_1 and ΔR_2^* parameter maps (1/s) for the mouse which received an injection of only MultiHance. C, D) ΔR_1 and ΔR_2^* parameter maps (1/s) for the mouse which received only SPIO Rhodamine B.

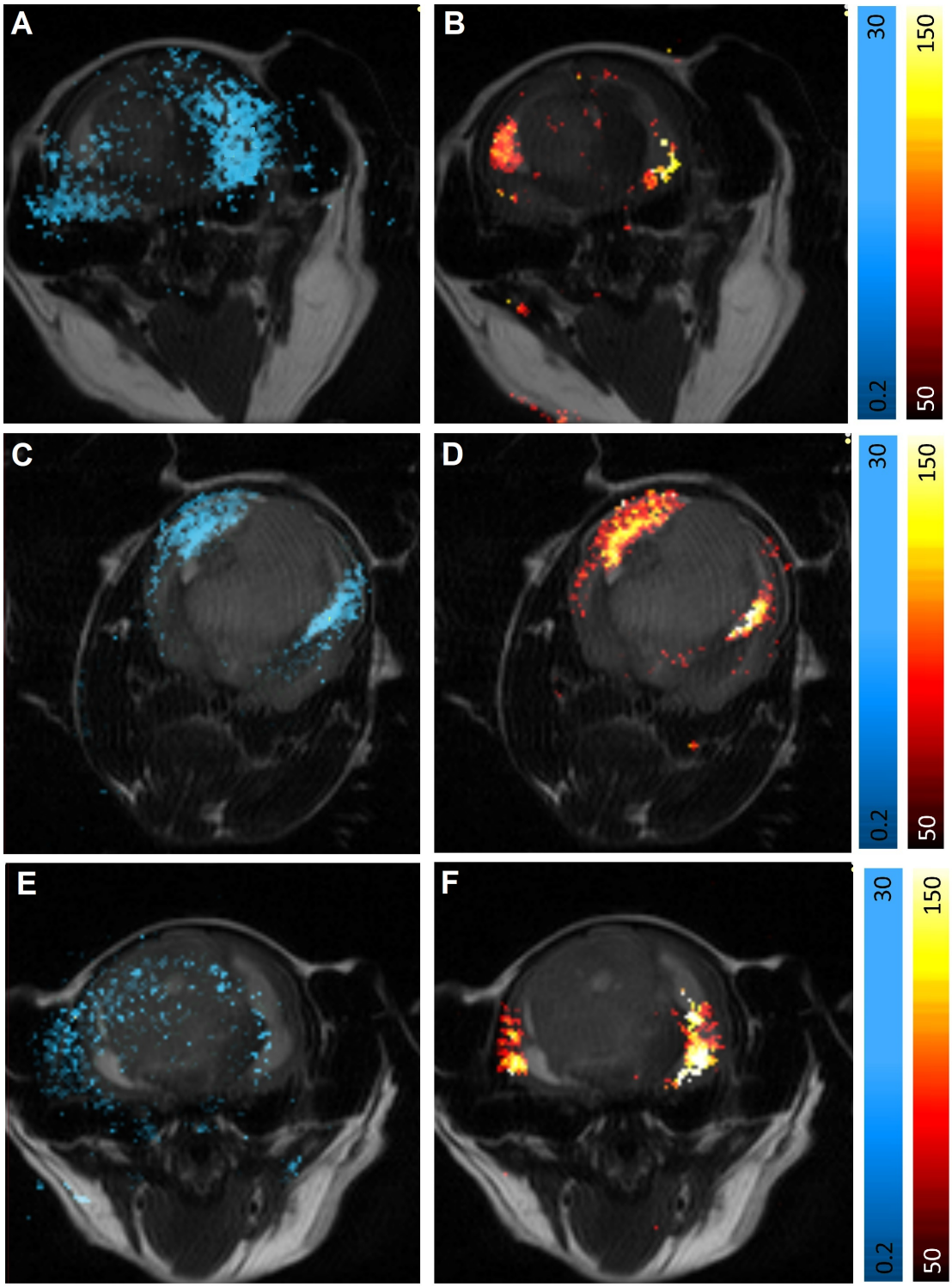

Figure 6.3: Relaxation rate maps for 3 mice which received both agents. A, C, E) ΔR_1 parameter maps (1/s). B,D,F) ΔR_2^* parameter maps (1/s).

The mice shown in Figure 6.2 show the single agent control mice. In both cases, as expected we see an increase in the predominant relaxation map for the administered contrast agent, ΔR_1 for MultiHance, and ΔR_2^* for SPIO Rhodamine B. Visually, the increase in ΔR_2^* in the SPIO Rhodamine B only mouse surrounds the expected tumour region. This is not the case for ΔR_1 in the MultiHance mouse, where values increase in almost every region of the mouse brain. Figure 6.3 shows the ΔR_1 and ΔR_2^* parameter maps for 3 dual contrast mice. Here we see most of the same features as with single agent mice. However, one notable difference is that while ΔR_1 values are in some cases spread throughout the entire brain, we also see high value changes in the locations where ΔR_2^* increases. This demonstrates why dual contrast mapping is so difficult: both contrast agents affect both parameter maps. In this case, we see the SPIO agent greatly contributing to the ΔR_1 maps.

6.3.2 Concentration Maps

Figure 6.4 and 6.5 show axial slices of dual concentration parameter maps for five different mice. All axes have been fixed to the same values to allow for better comparison. Figure 6.4 shows mice which only received MultiHance, or only received SPIO Rhodamine B, where Figure 6.5 shows mice which received both SPIO Rhodamine B and MultiHance injections.

For the single agent maps, when comparing Figure 6.2 to Figure 6.4, we see that areas which have high ΔR_2^* directly align with areas MRF predicts the SPIO is located, as SPIO has a high r_2^* when compared to MultiHance, and so predictably is responsible for the majority of ΔR_2^*. Conversely, we see that an increase in ΔR_1 does not directly coincide with an increase in predicted MultiHance, as the r_1 values for both MultiHance and SPIO Rhodamine B are much more similar.

Visually, the deposition of SPIO agent in all mice is biologically appropriate; the tumours centralized in the brains are free of SPIO in their necrotic core, while the exterior region macrophages will phagocytose the agent, creating clustered regions of SPIO. In Figure 6.5, especially aggressive tumours (red circles) have most likely resulted in the macrophages spilling into the enlarged ventricles (arrows) around the tumours. The exception is Figure 6.4 A/B, in which no SPIO was administered. The concentration map Figure 6.4 B aligns with this expectation. Table 6.2 contains the

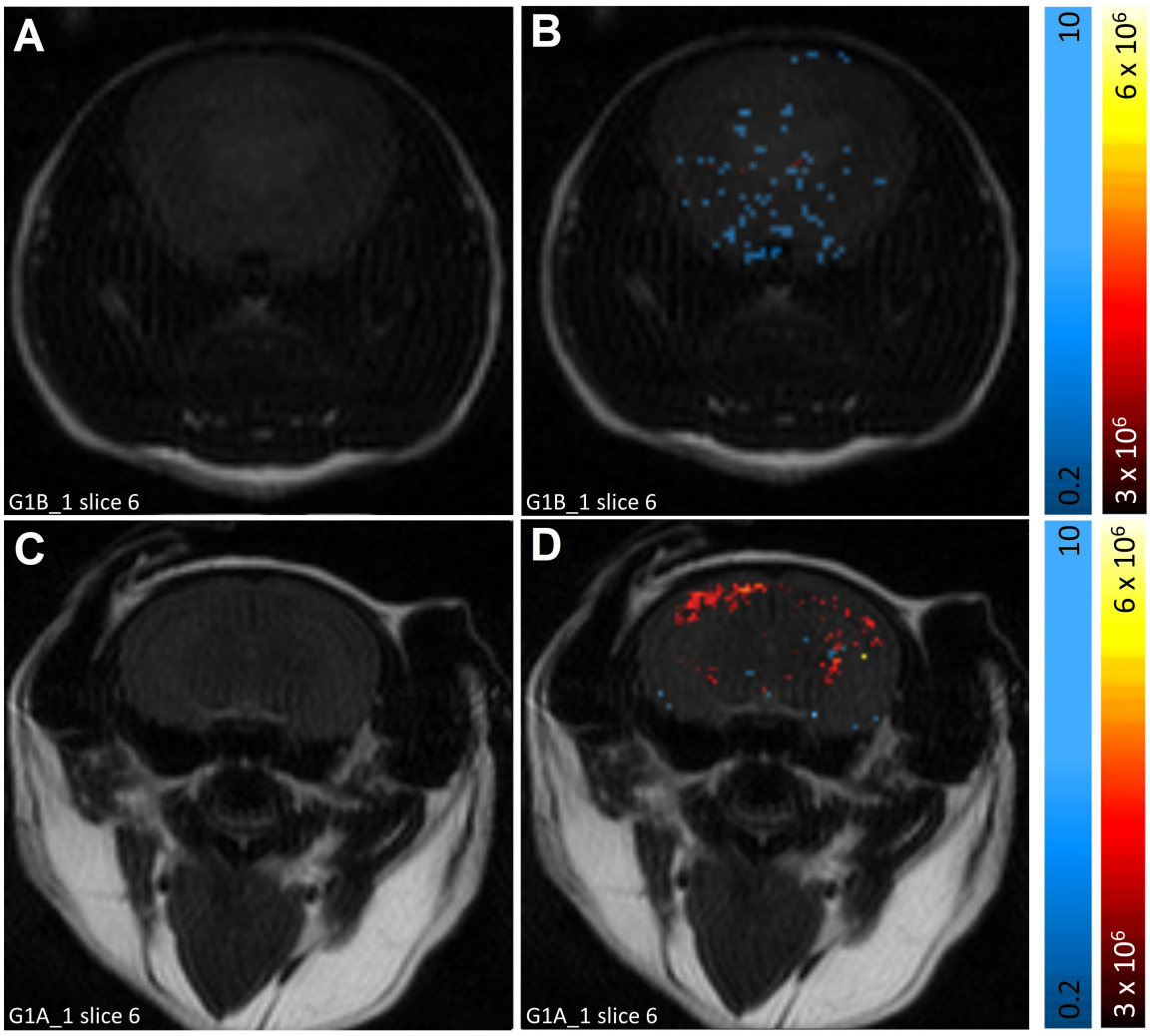

Figure 6.4:
Dual contrast concentration maps for mice which received only 1 contrast agent. A) FSE anatomical axial slice of mouse which received an injection of only MultiHance. B) The same anatomical FSE image, with MRF concentration maps of SPIO Rhodamine B (red)(cells/ml) and MultiHance (blue)(mM) overlaid. C) FSE anatomical axial slice of mouse which received an injection of only SPIO Rhodamine B. D) The same anatomical FSE image, with MRF concentration maps of SPIO Rhodamine B (red)(cells/ml) and MultiHance (blue)(mM) overlaid.

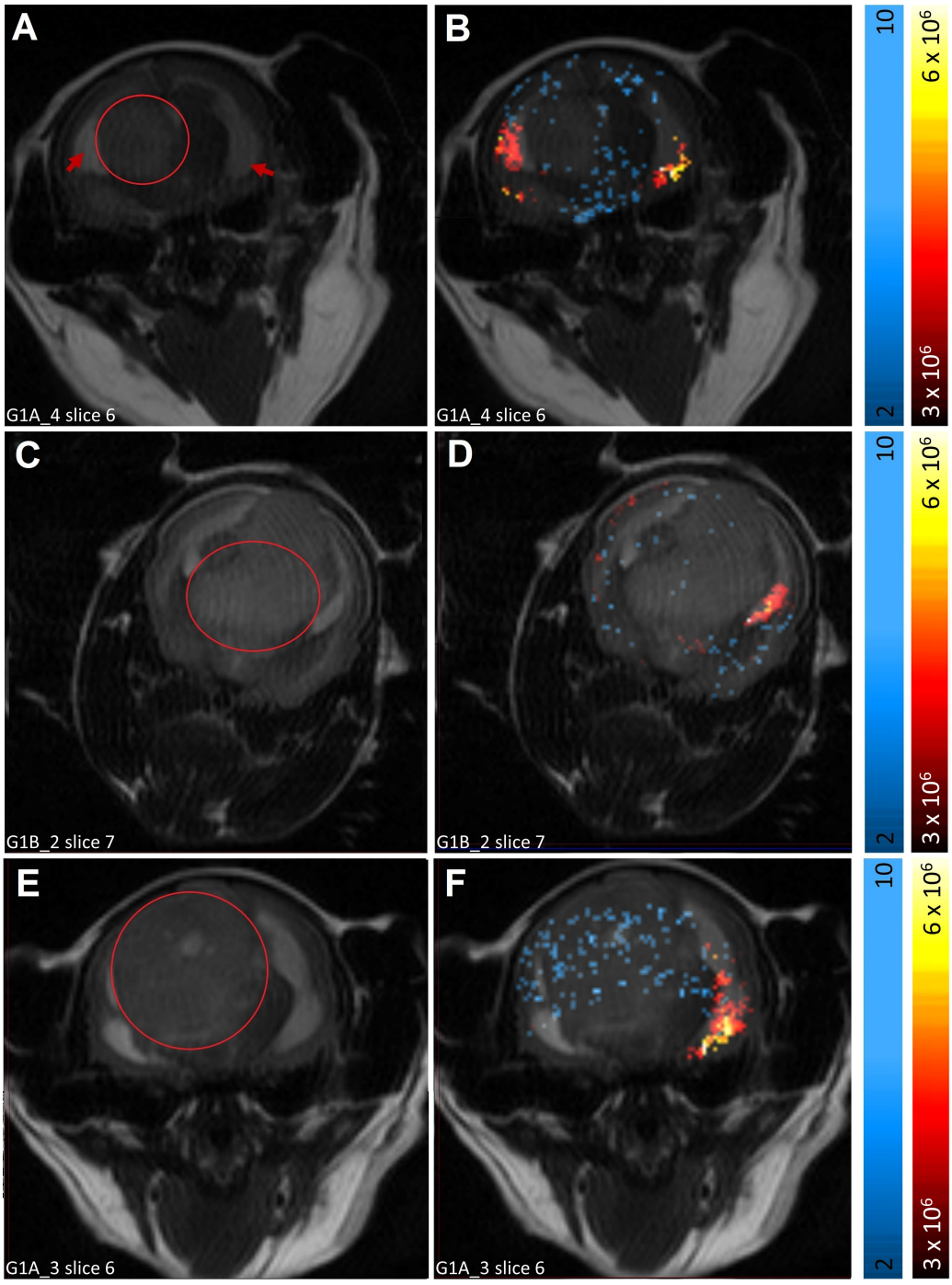

Figure 6.5:
Dual contrast concentration maps for 3 mice which received both agents. A,C,E) FSE anatomical axial slice of mouse implanted with glioblastoma cells, which received injections of both MultiHance and SPIO Rhodamine B. Tumour region is outlined with a red circle, and ventricles highlighted with arrows. B,D,F) The same anatomical FSE image, with MRF concentration maps of SPIO Rhodamine B (red)(cells/ml) and MultiHance (blue)(mM) overlaid.

	Iron			Gadolinium		
	Total Cells	Clusters	Size (vx)	Gad (mM)	Clusters	Size (vx)
G1A_1	2,180,900	9	7.2442	1.09	138	1.6594
G1A_2	1,233,300	19	4.9067	4.21	135	1.9286
G1A_3	1,110,000	14	8.0732	2.90	51	1.1111
G1A_4	1,248,000	17	6.8654	1.15	167	2.5903
G1B_1	65,190	11	1.3125	1.44	154	2.757
G1B_2	2,291,900	18	15.5111	3.58	221	2.5578
G2_1	DECEASED					
G2_2	4,120,700	23	25.9524	1.59	183	4.2727

Table 6.2: Results for the total agent amounts and clustering data for all mice. This includes the number of clusters, as well as their average size for each contrast agent. G2_1 did not survive until the second set of scans, and so no maps were produced.

total amount of each contrast agent in each mouse, as well as deposition statistics. G2_2 mouse results are not included, as the mouse died prior to receiving post injection scans, and so no concentration maps could be generated. Here we see results that align with our interpretation of the visual inspection, with SPIO Rhodamine B labelled cell counts for the entire brain predicted to be in the 1 - 4 million/mL range for all mice, which the exception of G1B_1, which received no SPIO Rhodamine B.

Unfortunately, the same cannot be said for the predicted MultiHance mapping. Firstly, while the mouse without a gadolinium injection shows the lowest amount of gadolinium, the amount predicted by MRF is still 1.09 mM, similar to mice that did receive Gadolinium in injections, such as G1A_1 and G1B_1 with estimated totals of 1.15 and 1.44 respectively. More importantly, we would expect to see gadolinium cluster in a way similar to the SPIO contrast agent, congregating around the periphery of the tumour. What is instead seen is an almost random spread throughout the brain, indicative that the signal is spurious in nature. When examining the cluster statistics gathered in Table 6.2, we find that on average SPIO Rhodamine B maps are clustered into 9.5x less groups than gadolinium, with clusters containing an average of over 4x more voxels. Gadolinium deposition statistics describe a much more diffuse gadolinium than expected, suggesting erroneous mapping.

One way to probe if relaxivity values have a strong effect on the resulting parameter maps is by measuring the effect of applying a multiplication factor to a single relaxivity value.

6.3.3 Concentration Maps with Varied Relaxivity Values

Figure 6.5 show the concentration maps for the single agent administered mice. The maps were generated by scaling a relaxivity term in Equation 6.1 by either 0.5x, 1x, or 2x to demonstrate the effect of having an inaccurate relaxivity value on the resulting concentration maps. For the MultiHance only mouse shown in Figure 6.5 A-C, r_1 for SPIO value was scaled, and for the SPIO Rhodamine B only mouse shown in Figure 6.5 A-C, r_2^* for MultiHance was scaled.

In figure Figure 6.5 D-F, we see that altering r_2^* for MultiHance has no significant effect on the resulting parameter maps. While the value of r_2^* for MultiHance is known, this supports that small changes within the r_2^* of MultiHance when ingested by macrophages in the brain will not alter SPIO mapping. This is expected, as previously stated, the r_2^* of MultiHance is much less than the expected r_2^* value of SPIO.

Conversely, in Figure 6.5 A-C we see that scaling SPIO's value of r_1 has a profound effect on the resulting concentration maps of MultiHance. When r_1 for SPIO is scaled 0.5x, the predicted amount of gadolinium greatly increases throughout all areas of the brain. This is unfortunate, as the relaxivity values of SPIO almost certainly vary greatly depending on the amount of SPIO loading per cell. This study was performed assuming an average cell loading of 3 pg/cell, based on previous *in vitro* studies with iron labelled macrophages. The exact relaxivity values of SPIO Rhodamine B when ingested by cells may vary greatly by the amount of agent injected, and the time since injection. Figure 6.5 highlights the potential downsides of the expansion to the linear relaxation model for dual contrast mapping; when the r_1 values of the two agents are not highly distinct, r_1 values must be well defined to not generate errors in the resulting concentration maps.

The r_2^* of SPIO and r_1 of MultiHance are not shown here, but the concentration map response to scaling these relaxivity values behaves as expected: both linearly scale the numerical values of relevant contrast agent, without affecting the overall map. Therefore, these two values are associated less with intra-concentration map errors seen in the MultiHance mapping, but with the value for the total amount of each contrast agent available in the brain. While this as an important value for the implementation of this tool in future work, a linear scaling factor does not undermine

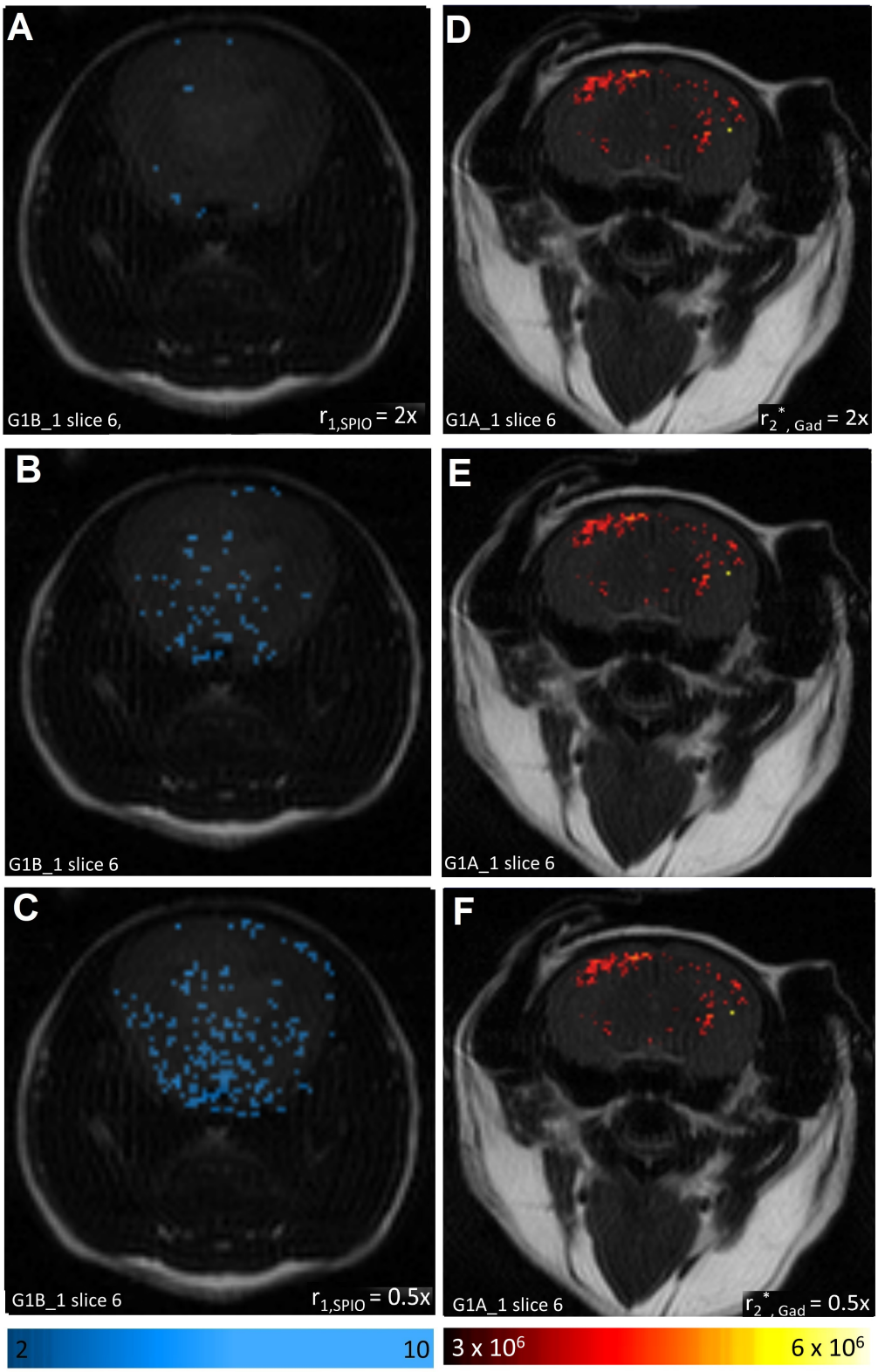

Figure 6.6: A,B,C) MultiHance concentration maps for mouse G1B_1 which received only MultiHance (mM), with a modified r_1 value for SPIO Rhodamine B. D,E,F) SPIO Rhodamine B concentration maps for mouse G1A_1 which received only SPIO Rhodamine B (cells/ml), with a modified r_2^* value for MultiHance.

the biological relevancy of these SPIO maps.

Unfortunately, acquiring accurate relaxivity values of cells labelled *in vivo* with SPIO is a challenging task. The relaxivity values used within this study come from iron-loaded T cells, and we know that macrophages take up iron at a different rate. Combined with more complex biological processes *in vivo*, mean that the r_1/r_2^* values were a first approximation only. To obtain a value for r_1/r_2^*, a measure of both the total number of macrophages, and the total amount of iron in a mouse brain would need to be measured. While acquiring a total number of macrophages could be achieved with a macrophage isolation kit, the method used in our lab relies on non-specific binding to everything except macrophages, which are then removed with a magnet. This becomes impossible when the macrophages are loaded with SPIO, as the magnet also removes the macrophages. While testing this method, the amount of macrophages successfully isolated was x10-100 smaller than the expected yield. Older methods such as a percoll gradient followed by a fluorescence tagging and sorting of cells are an option, but this can take a long time to complete, and requires that the sample is free of surface markers. We are currently going through this process in the lab, and should have more accurate r_1/r_2^* values soon.

Once the iron labelled macrophages could successfully be isolated, the issue is finding a technique sensitive enough to detect metals in such small quantities. A prototype study was performed using the isolated macrophages from 6 mice, which were digested in nitric acid and sent for both ICP-OES and ICP-MS testing, and both were found to not meet the sensitivity requirements to detects such small amounts of SPIO. This will be repeated once the macrophage isolation is optimized.

Nonetheless, assuming the successful acquisition of the total number of macrophages and iron in a mouse brain, the next step would be to create an *in vitro* phantom set with varying concentrations of SPIO loaded macrophages which had the same cell loading as an intravenous injection of SPIO Rhodamine B delivered 24 hours prior to scanning. This would allow for an accurate characterization of the relaxivity values, but given the array of complications which have arisen during the process of attempting to validate these concentration maps, acquisition of the relaxivity values for SPIO Rhodamine B loaded macrophages now lies firmly outside of the scope of this thesis.

6.4 Conclusions

The data in this chapter presents a strong case for the following: R_2^* sensitized MRF, accelerated by non-uniform SW, can generate concentration maps of SPIO labelled cells , in which the distributions shown make biological sense. Deposition data showed that gadolinium, while expected to be similar in distribution to SPIO labelled cells, were spread into over 9x more clusters which were on average 4x smaller, indicative that gadolinium mapping may not yet be functioning correctly.

While there are some limitations with the method in its current iteration, these have been shown to not interfere with the robustness of the SPIO concentration maps. It has been demonstrated that potentially spurious gadolinium concentration mapping may be linked to inaccurate r_1 value of SPIO, which can be built on by future studies to acquire more accurate relaxivity values.

Chapter 7

Conclusions

7.1 Summary

MR cellular imaging is a crucial tool for enabling the non-invasive tracking of immune cells, but is greatly limited with the currently available techniques. MR contrast agents can be used to track specific molecular species *in vivo*, yet conventional MR techniques may only image a single contrast agent at a time. With an ever growing variety of available contrast agents, allowing for multi-contrast agent quantification in MR cellular imaging would greatly improve the efficacy of preclinical studies. One example of a field which would greatly benefit from simultaneous quantification of multiple contrast agents is in development of immunotherapies, where disease models are complex, and more information could greatly decrease study times, reduce animal sample sizes, and optimize treatment regimes.

MRF is a novel MRI methodology which allows for simultaneous parameter map generation within a single scan, a prerequisite for multi-contrast imaging. MRF is adaptable and highly robust to undersampling, making it a promising candidate to enable multi-contrast cellular imaging. However, for use in preclinical cell tracking studies, MRF would have to be modified in a number of ways. Firstly, traditional MRF does not include sensitivity to T_2^*, a critical parameter for visualizing the most ubiquitous cell tracking compound, iron. This is due to MRF being originally based around bSSFP, a sequence which intentionally avoids T_2^* sensitivity by perfectly aligning defocused and refocused signals. Secondly, conventional methods of acceleration that have been applied to MRF are not applicable in a preclinical setting. These include parallel imaging, where a multichannel coil is required for the iterative optimization, or machine learning algorithms, where large datasets are required to train to models. For MRF to reach its full potential in preclinical *in vivo* cell tracking studies an acceleration solution with these constraints in mind must be realised.

Therefore, the goal of this thesis was as follows: To develop and apply an implementation of MRF which included sufficient T_2^* mapping to quantify SPIO labelled cells and a gadolinium contrast agent *in vivo*, in 3D, within a preclinically acceptable scan time of approximately 20 mins. This was split in to three distinct steps.

The first step was to develop T_2^* sensitive MRF on our preclinical system and to demonstrate dual quantification with iron. While inclusion of T_2^* in an MRF was not new, this often involved adaptations which our system was not capable of. After initial implementation of standard T_1 and T_2 MRF using a bFFSP sequence and Bloch equation dictionary generation, it became clear that adding T_2^* to a bSSFP would be difficult, as the dictionary included an off-resonance dimension which greatly scaled up dictionary size and processing time.

Instead, bSSFP was modified to produce an SSFP sequence, which removes the necessity for an off resonance dimension, but requires the more complicated EPG-based dictionary to be implemented. This sequence allowed for the addition of T_2^* sensitivity, by moving the acquisition window away from the centre of repetition time and scaling the dictionary by $exp(-TE/T_2^*)$. To improve k-space coverage, a variable density spiral k-space trajectory was designed allowing for fully sampling the centre of k-space within 8 interleaves, while fully sampling the outer k-space in 64 interleaves. The initial implementation of this spiral interleaf was rotated by 7.5 degrees per imaging frame, but this was later optimized by rotating by the golden angle to allow for better k-space coverage at very high undersampling factors. The resulting sequence was approximately 28 minutes in length to provide a single slice MRF.

To test the undersampling capacity and dual contrast mapping capabilities, phantoms mixed with varying concentrations of Gd or iron labelled cells were created and scanned, and results were retrospectively undersampled by up to 16x. Results showed that T_1, T_2 and T_2^* maps generated by the MRF sequence were in agreement with gold standard values, and that undersampling by 8x did not increase the NRMSE to more than 0.05, but rapidly increased with further undersampling. MRF parameter maps were used to generate dual contrast maps, which strongly agreed with the known values, with CCC values > 0.95.

After validating the dual contrast capabilities of the sequence, a pilot *in vivo*

study was performed to test the data quality with heavy undersampling. A C57BL/6 mouse was injected with gadolinium 20 minutes prior to scanning and was imaged using MRF. Results showed that 128 x 128 x 8 parameter maps of a mouse brain were still visible at 8x undersampling, but produced concentration maps would only match fully sampled results up to 4x undersampling. This meant that with the currently implemented MRF sequence, a full 128 x 128 x 16 brain scan of a mouse would take 112 minutes, far too slow for *in vivo* use.

The second step was to take the already existing MRF sequence and accelerate it. Through utilizing a sliding window (SW) approach, experiments showed that adjusting the length of a sliding window with this implementation of T_2^* MRF would change the sensitivity/accuracy of individual parameters. When a 24x undersampled MRF dataset was reconstructed using a window length of 3, T_1 and T_2 accuracy was diminished, but T_2^* mapping would remain accurate. However, when increasing the window length the reverse would occur, where T_2^* sensitivity was damaged but T_1 would be mapped accurately.

This was solved by adapting traditional SW, as to use the higher accuracy of a longer window without damaging the T_2^* sensitivity of the sequence. To this end, a nonuniform sliding window was developed. Noting that the sequence T_2^* sensitivity was provided by the final 400 imaging frames of the MRF sequence, a lower sliding window length of 3 was applied to these 400 entries, while the rest of the sequence was subject to a sliding window length of 6.

To validate this nonuniform sliding window MRF, phantoms again mixed with varying concentrations of Gd or iron labelled cells were created and scanned and reconstructed with a window length of 3, 6, or the nonuniform 3/6 combination. The results of the nonuniform window MRF strongly statistically correlated with the known values for the phantoms, even when undersampled 24x, and allowed for dual contrast mapping. A uniform window length did not result in a match to known values at 24x undersampling.

With this verified, an implementation of T_2^* MRF with nonuniform SW was finalized for *in vivo* testing. This version produces a 96 x 96 x 16 image at 16x undersampling in 20 minutes. Here, the resolution was lower to match the anatomical FSE that accompanies the MRF, and a lower acceleration than 24x was used to

pre-empt the degradation in quality seen in the *in vivo* pilot data when compared to *in vitro* results.

In Chapter 6, the final step was to apply nonuniform SW MRF in an *in vivo* study to demonstrate that the developed technique can provide in vivo dual concentration maps. Eight C57BL/6 mice were implanted with a glioma-261 cell line, and imaged 28 days post-surgery after receiving injections of SPIO Rhodamine B 24 hours prior, and a gadolinium during scanning. Two mice only received a single injection to act as controls.

Generated concentration maps showed that SPIO labelled cells were located around the periphery of the tumours in all mice which received iron injections, while no SPIO was mapped to the necrotic tumour core. High SPIO deposition was also seen in the enlarged ventricles, overall demonstrating SPIO mapping of biological relevance. MultiHance mapping, however, was not clustered, and was said to be most likely spurious. Parameter maps of the single agent mice were analysed, where the change in R_1 values due the the addition of MultiHance was visible, suggesting that errors in the concentration mapping is due to relaxivity values.

To verify this, relaxivity values used in the linear relaxation model. While a MultiHance's r_2^* was found to have no significant effect on resulting SPIO concentration maps, the r_1 value for SPIO Rhodamine B was shown to greatly effect MultiHance parameter maps. The steps necessary for acquiring an accurate r_1 value for SPIO Rhodamine B are discussed as future work for this project.

Despite difficulties currently quantifying MultiHance, these *in vivo* experiments demonstrated that MRF produced SPIO concentration maps that make biological sense, and are robust to errors in relaxivity values.

7.2 Future Directions

This project has focused on a singular objective: the quantification of two contrast agents at the same time, *in vivo*, in an appropriate biological time-frame of 20 mins. This was accomplished in 3 steps: Development of a T_2^* sensitive MRF sequence, acceleration of this sequence while preserving sensitivity, and demonstration of *in vivo* application. As with all long term research projects, many opportunities for further development presented themselves, but were not within the scope of the Ph.D. This

section addresses some ways in which this project could be built upon.

7.2.1 Dictionary Model Complexity

MRF's entire principle is matching a signal to a model, and so the results can only ever be as good as the model is realistic. In the last few years, several new implementation methods for MRF dictionaries have been introduced which promise to improve the accuracy of dictionary matches. Examples include adding a B_1 dimension to the dictionary, or modelling diffusion for each iteration of the imaging frame. There now exists an entire field of study for MRF dictionary optimization, yet MRF is still new enough that dictionary architecture is not standardized. As a result, every innovation must be both adjusted for use with the individual implementation of MRF, and then tested to ensure the validity of results. Dictionary generation is by far the most time consuming aspect of MRF, and is often only performed a handful of times during the initialization of an MRF protocol, and so iterative additions to improve the dictionary model are time prohibitive, as well as tremendously computationally expensive.

This effect is compounded with every additional feature added to the dictionary. For example, originally the acceleration process of MRF implemented in this work included B_1 sensitivity within the dictionary, but was disabled due to increasing dictionary generation time from 20 to 200 hours. Likewise, the simulation code for diffusion exists within the dictionary generation script, but has never actually been enabled due to time constraints. Nonetheless, a dedicated study of additional dictionary complexity would be an asset to the research performed in this thesis.

7.2.2 Sequence Sensitivity Optimization

The sequence used in this project is one solution, but MRFs flexibility means that several other sequence parameter patterns exist which would work equally well. It stands to reason that there also exist configurations more sensitive to the range of T_2^* values present during imaging of iron labelled cells. MRF literature contains more novel applications of MRF sequences than can possibly be demonstrated within a single Ph.D. Therefore an interesting addition to the work performed in this thesis would be exploration of novel sequence applications, both those contained within more recent literature from the development of this implementation of MRF, and

further work on optimization of the novel T_2^* sensitive TE ramping demonstrated in Chapter 4. This could include new parameter variations to further probe T_2^* sensitivity, shortening the sequence length to allow for less undersampling and higher data quality, or inclusion of the recently popular 'static TR' MRF sequences emerging over the last year.

7.2.3 Post Processing Additions

Currently, use of MRF to quantify contrast agents simultaneously is limited to the brain of a mouse. This is not a limitation caused by anything inherent in the MRF architecture, but a restriction of the post-processing pipeline of co-registration of images taken 24 hours apart. Currently, human input is required for z-axis alignment, then a rigid co-registration algorithm aligns the axial slices of an FSE image set, finally applying the needed transformations to the MRF data. This works well because mouse skulls are rigid and show as positive contrast on an FSE image.

Attempts were made to both perform a mouse flank co-registration with rigid registration, and to develop a deformable co-registration algorithm, but the former performed poorly, and the latter could not be achieved within a reasonable time-frame without derailing the project. The next logical step for this would be to incorporate a deformable registration to allow for dual cell tracking in other areas of a mouse such as the flank.

During generation of concentration maps in Chapter 6, threshholding as applied via visual inspection. While this is a necessary step to providing visually readable concentration maps, this technically functions as a binary classifier for locations which do or do not contain contrast agent. As such, it may be prudent in include ROC analysis in future implementations of this threshholding. Another option is to include a more sophisticated threshholding procedure, such as using the clustering data used in Chapter 6 analysis to define minimum clusters of agent required to show visually.

7.2.4 Further Biological Demonstration

To fully validate MRF as a viable tool for *in vivo* cell tracking studies with two contrast agents, a series of further biological experiments are required; more accurate and invasive techniques can demonstrate that MRF concentration maps in a mouse

brain are approximately the same as known values. For a thorough validation, it is necessary to confirm both the total amount of each contrast agent, and its position within a mouse brain.

To obtain the total amount of each contrast agent, Inductively Coupled Plasma Mass Spectrometry (ICP-MS) would be an appropriate technique. ICP-MS is an analytical technique for measuring trace elements. While other techniques for this purpose exist, ICP-MS boasts many advantages, such as a lower detection limit, higher sample throughput, larger analytical range, and lower sample volume than older methods such as flame photometry, inductively coupled plasma atomic emission spectroscopy, or cold vapour/hydride generation atomic absorption. Most importantly, ICP-MS allows for multiple element traces to be measured in a single analysis, critical for measuring both iron and gadolinium concentration in cell populations harvested from the brain. By measuring the total contrast agent concentration of the brain in macrophages, and counting the number of macrophages present, the iron load per macrophage *in vivo* estimation used for this work could be validated. In the event that its value differs significantly from the assumed value, new relaxivity values for the cells may need to be calculated. It will be important that prior to ICP-MS analysis, the cell isolations performed do not utilize methods which may be compromised by the iron content within the cells, such as methods which rely on a magnet to isolate macrophages.

To demonstrate cell and iron localization, a good candidate is IHC. IHC is a method of visualizing the presence of specific cell populations via attachment of an antibody conjugated to a fluorophore. When combined with contrast agents which are also appended with fluorophores, IHC offers preparation to validate both datasets using fluorescence microscopy, where both the location of of macrophages and contrast agent can be visualised. This is the reason that two mice were set aside and frozen for future biopsy.

7.3 Conclusions

The work in this thesis presents a strong case for the following: MRF can sufficiently map T_2^* to provide concentration maps for SPIO labelled cells *in vivo*, in 3D, within a preclinically acceptable scan time of approximately 20 mins.

This was done by adapting traditional MRF to be sensitive to T_2^* with TE moderation, and a nonuniform SW utilizing higher accuracy of a longer window without damaging the T_2^* sensitivity of the sequence. A lower sliding window length of 3 was applied to the 400 final entries of the sequence, with the rest utilizing a sliding window length of 6. Concentration maps of SPIO labelled cells a glioblastoma model within a mouse brain were imaged, which showed biologically relevant distributions. These were shown to be robust to several sources of error.

While there are some limitations with MultiHance mapping in MRFs current iteration, MultiHance concentration mapping errors were shown to be linked to inaccurate r_1 value of SPIO, which can be built on by future studies to acquire more accurate relaxivity values.

There exist many applications for MRF which has been optimized for *in vivo* studies on preclinical systems. The first is an extension of what has already been demonstrated in this work; dual contrast imaging has the potential to aid in the study of blood-brain barrier permeability, and could also extend to tracking multiple biomarkers associated with neurological diseases. This could provide information which we currently do not have access to, such as the positional behaviour of macrophages around a tumour site.

Our lab currently uses MRF in a number of studies. For example, MRF generated contrast agent maps are used as progenitors for radiomics features, which may help to predict survival outcomes for glioblastoma immunology studies. MRF is also being used to monitor drug delivery and distribution, tracking the biodistribution of immune cell populations (and potentially therapeutic agents) tagged with a contrast agent, to optimise treatment of various cancers.

Despite its focus in this work, the value of dual contrast imaging isn't limited to the brain. MRFs dual contrast agent mapping can aid in the characterisation of tumours at many locations, providing information about tumour vasculature, angiogenesis, and metabolic activity simultaneously.

There are many other applications of dual contrast MRF which lay far outside this work. These include the use of MRF in functional imaging studies of cardiovascular systems, or using two contrast agents targeted to different neurotransmitter systems

to map neurotransmitter dynamics in the brain. Overall, dual contrast MRF accelerated for preclinical system use is a versatile and powerful tool which could lead to many interesting and exciting developments.

Bibliography

[1] Luisa Ottobrini, Cristina Martelli, Daria Lucia Trabattoni, Mario Clerici, and Giovanni Lucignani. In vivo imaging of immune cell trafficking in cancer. *European Journal of Nuclear Medicine and Molecular Imaging*, 38(5):949–968, May 2011. Publisher: Springer Berlin Heidelberg.

[2] Moritz F. Kircher, Sanjiv S. Gambhir, and Jan Grimm. Noninvasive cell-tracking methods. *Nature Reviews. Clinical Oncology*, 8(11):677–688, September 2011.

[3] Rahul A. Sheth and Umar Mahmood. Optical molecular imaging and its emerging role in colorectal cancer. *American Journal of Physiology - Gastrointestinal and Liver Physiology*, 299(4):G807–G820, October 2010.

[4] Hideo Saji. In Vivo Molecular Imaging. *Biol. Pharm. Bull.*, 40(10):11, 2017.

[5] Min Wu and Jian Shu. Multimodal Molecular Imaging: Current Status and Future Directions, 2018. ISSN: 1555-4309 Library Catalog: www.hindawi.com Pages: e1382183 Publisher: Hindawi Volume: 2018.

[6] Dongkyu Kim, Yong Yeon Jeong, and Sangyong Jon. A Drug-Loaded Aptamer-Gold Nanoparticle Bioconjugate for Combined CT Imaging and Therapy of Prostate Cancer. *ACS Nano*, 4(7):3689–3696, July 2010. Publisher: American Chemical Society.

[7] Tarik F. Massoud and Sanjiv S. Gambhir. Molecular imaging in living subjects: seeing fundamental biological processes in a new light. *Genes & Development*, 17(5):545–580, March 2003.

[8] Habib Zaidi and Rameshwar Prasad. Advances in multimodality molecular imaging. *Journal of Medical Physics / Association of Medical Physicists of India*, 34(3):122–128, 2009.

[9] Charles Glaus, Raffaella Rossin, Michael J. Welch, and Gang Bao. In Vivo Evaluation of ^{64} Cu-Labeled Magnetic Nanoparticles as a Dual-Modality PET/MR Imaging Agent. *Bioconjugate Chemistry*, 21(4):715–722, April 2010.

[10] Toshiro Kitagawa, Hisanori Kosuge, Masaki Uchida, Yasunori Iida, Ronald L. Dalman, Trevor Douglas, and Michael V. McConnell. RGD targeting of human ferritin iron-oxide nanoparticles enhances in vivo molecular MRI of experimental aortic aneurysms. *Journal of Cardiovascular Magnetic Resonance*, 14(1):M9, February 2012.

[11] Tinghui Li, Susan Murphy, Boris Kiselev, Kanwarpal S. Bakshi, Jianyuan Zhang, Amnah Eltahir, Yafen Zhang, Ying Chen, Jie Zhu, Richey M. Davis, Louis A. Madsen, John R. Morris, Daniel R. Karolyi, Stephen M. LaConte, Zhi Sheng, and Harry C. Dorn. A New Interleukin-13 Amino-Coated Gadolinium Metallofullerene Nanoparticle for Targeted MRI Detection of Glioblastoma Tumor Cells. *Journal of the American Chemical Society*, 137(24):7881–7888, June 2015.

[12] Zhuxian Zhou, Mohammed Qutaish, Zheng Han, Rebecca M. Schur, Yiqiao Liu, David L. Wilson, and Zheng-Rong Lu. MRI detection of breast cancer micrometastases with a fibronectin-targeting contrast agent. *Nature Communications*, 6:7984, August 2015.

[13] Erik M. Shapiro, Stanko Skrtic, Kathryn Sharer, Jonathan M. Hill, Cynthia E. Dunbar, and Alan P. Koretsky. MRI detection of single particles for cellular imaging. *Proceedings of the National Academy of Sciences*, 101(30):10901–10906, July 2004. Publisher: National Academy of Sciences Section: Biological Sciences.

[14] Christoper M. Long and Jeff WM Bulte. In vivo tracking of cellular therapeutics using magnetic resonance imaging. *Expert Opinion on Biological Therapy*, 9(3):293–306, March 2009. Publisher: Taylor & Francis _eprint: https://doi.org/10.1517/14712590802715723.

[15] Moriel H Vandsburger, Marina Radoul, Batya Cohen, and Michal Neeman. MRI Reporter Genes: Application to Imaging of Cell Survival, Proliferation, Migration, and Differentiation. *NMR in biomedicine*, 26(7):872–884, July 2013.

[16] Rex A. Moats, Scott E. Fraser, and Thomas J. Meade. A "Smart" Magnetic Resonance Imaging Agent That Reports on Specific Enzymatic Activity. *Angewandte Chemie International Edition in English*, 36(7):726–728, 1997. _eprint: https://onlinelibrary.wiley.com/doi/pdf/10.1002/anie.199707261.

[17] Bryan C. Fuchs, Huifang Wang, Yan Yang, Lan Wei, Miloslav Polasek, Daniel T. Schühle, Gregory Y. Lauwers, Ashfaq Parkar, Anthony J. Sinskey, Kenneth K. Tanabe, and Peter Caravan. Molecular MRI of collagen to diagnose and stage liver fibrosis. *Journal of Hepatology*, 59(5):992–998, November 2013.

[18] Peter Caravan, Yan Yang, Roshini Zachariah, Anthony Schmitt, Mari Mino-Kenudson, Howard H. Chen, David E. Sosnovik, Guangping Dai, Bryan C. Fuchs, and Michael Lanuti. Molecular magnetic resonance imaging of pulmonary fibrosis in mice. *American Journal of Respiratory Cell and Molecular Biology*, 49(6):1120–1126, December 2013.

[19] Miloslav Polasek, Yan Yang, Daniel T. Schühle, Mohammad A. Yaseen, Young R. Kim, Yu Sub Sung, Alexander R. Guimaraes, and Peter Caravan. Molecular MR imaging of fibrosis in a mouse model of pancreatic cancer. *Scientific Reports*, 7(1):8114, August 2017. Number: 1 Publisher: Nature Publishing Group.

[20] Adam J. Shuhendler, Deju Ye, Kimberly D. Brewer, Magdalena Bazalova-Carter, Kyung-Hyun Lee, Paul Kempen, K. Dane Wittrup, Edward E. Graves, Brian Rutt, and Jianghong Rao. Molecular Magnetic Resonance Imaging of Tumor Response to Therapy. *Scientific Reports*, 5:14759, October 2015.

[21] Anant S. Krishnan, Andre A. Neves, Maaike M. de Backer, De-En Hu, Bazbek Davletov, Mikko I. Kettunen, and Kevin M. Brindle. Detection of cell death in tumors by using MR imaging and a gadolinium-based targeted contrast agent. *Radiology*, 246(3):854–862, March 2008.

[22] Julien Santelli, Séverine Lechevallier, Houda Baaziz, Marine Vincent, Cyril Martinez, Robert Mauricot, Angelo Parini, Marc Verelst, and Daniel Cussac. Multimodal gadolinium oxysulfide nanoparticles: a versatile contrast agent for mesenchymal stem cell labeling. *Nanoscale*, 10(35):16775–16786, September 2018. Publisher: The Royal Society of Chemistry.

[23] Winda Ariyani, Toshiharu Iwasaki, Wataru Miyazaki, Erdene Khongorzul, Takahito Nakajima, Satomi Kameo, Hiroshi Koyama, Yoshito Tsushima, and Noriyuki Koibuchi. Effects of Gadolinium-Based Contrast Agents on Thyroid Hormone Receptor Action and Thyroid Hormone-Induced Cerebellar Purkinje Cell Morphogenesis. *Frontiers in Endocrinology*, 7, 2016. Publisher: Frontiers.

[24] Jamal Guenoun, Alessandro Ruggiero, Gabriela Doeswijk, Roel C. Janssens, Gerben A. Koning, Gyula Kotek, Gabriel P. Krestin, and Monique R. Bernsen. In vivo quantitative assessment of cell viability of gadolinium or iron-labeled cells using MRI and bioluminescence imaging. *Contrast Media & Molecular Imaging*, 8(2):165–174, 2013. _eprint: https://onlinelibrary.wiley.com/doi/pdf/10.1002/cmmi.1513.

[25] Chen Chen, Chang Qiang Wu, Tian Wu Chen, Meng Yue Tang, and Xiao Ming Zhang. Molecular Imaging with MRI: Potential Application in Pancreatic Cancer, October 2015. ISSN: 2314-6133 Library Catalog: www.hindawi.com Pages: e624074 Publisher: Hindawi Volume: 2015.

[26] Ali Barandov, Benjamin B. Bartelle, Beatriz A. Gonzalez, William L. White, Stephen J. Lippard, and Alan Jasanoff. Membrane-Permeable Mn(III) Complexes for Molecular Magnetic Resonance Imaging of Intracellular Targets. *Journal of the American Chemical Society*, 138(17):5483–5486, May 2016. Publisher: American Chemical Society.

[27] Kelly Kimberly A., Allport Jennifer R., Tsourkas Andrew, Shinde-Patil Vivek R., Josephson Lee, and Weissleder Ralph. Detection of Vascular Adhesion Molecule-1 Expression Using a Novel Multimodal Nanoparticle. *Circulation Research*, 96(3):327–336, February 2005. Publisher: American Heart Association.

[28] Eyk A. Schellenberger, David Sosnovik, Ralph Weissleder, and Lee Josephson. Magneto/Optical Annexin V, a Multimodal Protein. *Bioconjugate Chemistry*, 15(5):1062–1067, September 2004. Publisher: American Chemical Society.

[29] Myriam N. Bouchlaka, Kai D. Ludwig, Jeremy W. Gordon, Matthew P. Kutz, Bryan P. Bednarz, Sean B. Fain, and Christian M. Capitini. (19)F-MRI for monitoring human NK cells in vivo. *Oncoimmunology*, 5(5):e1143996, May 2016.

[30] John V. Frangioni and Roger J. Hajjar. In vivo tracking of stem cells for clinical trials in cardiovascular disease. *Circulation*, 110(21):3378–3383, November 2004.

[31] Pippa Storey, Ruth P. Lim, Hersh Chandarana, Andrew B. Rosenkrantz, Daniel Kim, David R. Stoffel, and Vivian S. Lee. MRI assessment of hepatic iron clearance rates after USPIO administration in healthy adults. *Investigative Radiology*, 47(12):717–724, December 2012.

[32] Monique R. Bernsen, Amber D. Moelker, Piotr A. Wielopolski, Sandra T. van Tiel, and Gabriel P. Krestin. Labelling of mammalian cells for visualisation by MRI. *European Radiology*, 20(2):255–274, February 2010.

[33] Enzo Terreno, Simonetta Geninatti Crich, Simona Belfiore, Luigi Biancone, Claudia Cabella, Giovanna Esposito, Andrea D. Manazza, and Silvio Aime. Effect of the intracellular localization of a Gd-based imaging probe on the relaxation enhancement of water protons. *Magnetic Resonance in Medicine*, 55(3):491–497, 2006. _eprint: https://onlinelibrary.wiley.com/doi/pdf/10.1002/mrm.20793.

[34] Sushanta Kumar Mishra, Subash Khushu, Ajay K. Singh, and Gurudutta Gangenahalli. Homing and Tracking of Iron Oxide Labelled Mesenchymal Stem Cells After Infusion in Traumatic Brain Injury Mice: a Longitudinal In Vivo MRI Study. *Stem Cell Reviews and Reports*, 14(6):888–900, December 2018.

[35] Michel Modo, Diana Cash, Karen Mellodew, Steven C. R. Williams, Scott E. Fraser, Thomas J. Meade, Jack Price, and Helen Hodges. Tracking transplanted stem cell migration using bifunctional, contrast agent-enhanced, magnetic resonance imaging. *NeuroImage*, 17(2):803–811, October 2002.

[36] Greetje Vande Velde, Janaki Raman Rangarajan, Ruth Vreys, Caroline Guglielmetti, Tom Dresselaers, Marleen Verhoye, Annemie Van der Linden, Zeger Debyser, Veerle Baekelandt, Frederik Maes, and Uwe Himmelreich. Quantitative evaluation of MRI-based tracking of ferritin-labeled endogenous neural stem cell progeny in rodent brain. *NeuroImage*, 62(1):367–380, August 2012.

[37] Ethel J. Ngen, Lee Wang, Yoshinori Kato, Balaji Krishnamachary, Wenlian Zhu, Nishant Gandhi, Barbara Smith, Michael Armour, John Wong, Kathleen Gabrielson, and Dmitri Artemov. Imaging transplanted stem cells in real time using an MRI dual-contrast method. *Scientific Reports*, 5(1):13628, November 2015.

[38] Marie-Laurence Tremblay, Christa Davis, Chris V. Bowen, Olivia Stanley, Cathryn Parsons, Genevieve Weir, Mohan Karkada, Marianne M. Stanford, and Kimberly D. Brewer. Using MRI cell tracking to monitor immune cell recruitment in response to a peptide-based cancer vaccine. *Magnetic Resonance in Medicine*, 80(1):304–316, 2018.

[39] Richardson MA, Ramirez T, Russell NC, and Moye LA. Coley toxins immunotherapy: a retrospective review. *Alternative Therapies in Health & Medicine*, 5(3):42–47, May 1999. Place: Eagan, Minnesota Publisher: Inno-Visions Professional Media.

[40] Philip J. Bergman. Cancer Immunotherapies. *The Veterinary Clinics of North America. Small Animal Practice*, 49(5):881–902, September 2019.

[41] Tomoyuki Yamaguchi and Shimon Sakaguchi. Regulatory T cells in immune surveillance and treatment of cancer. *Seminars in Cancer Biology*, 16(2):115–123, April 2006.

[42] Michael A. Morse, Paul J. Mosca, Timothy M. Clay, and H. Kim Lyerly. Dendritic cell maturation in active immunotherapy strategies. *Expert Opinion on Biological Therapy*, 2(1):35–43, January 2002. Publisher: Taylor & Francis _eprint: https://doi.org/10.1517/14712598.2.1.35.

[43] Daniel Zagury and Robert C Gallo. Anti-cytokine Ab immune therapy: present status and perspectives. *Drug Discovery Today*, 9(2):72–81, January 2004.

[44] Mohan Karkada, Genevieve M. Weir, Tara Quinton, Leeladhar Sammatur, Lisa D. MacDonald, Alecia Grant, Robert Liwski, Ridas Juskevicius, Gomathinayagam Sinnathamby, Ramila Philip, and Marc Mansour. A Novel Breast/Ovarian Cancer Peptide Vaccine Platform That Promotes Specific Type-1 but not Treg/Tr1-type Responses:. *Journal of Immunotherapy*, 33(3):250–261, April 2010.

[45] S. Sawada, G. Suzuki, Y. Kawase, and F. Takaku. Novel immunosuppressive agent, FK506. In vitro effects on the cloned T cell activation. *The Journal of Immunology*, 139(6):1797–1803, September 1987. Publisher: American Association of Immunologists.

[46] Andy J. Minn, Yibin Kang, Inna Serganova, Gaorav P. Gupta, Dilip D. Giri, Mikhail Doubrovin, Vladimir Ponomarev, William L. Gerald, Ronald Blasberg, and Joan Massagué. Distinct organ-specific metastatic potential of individual breast cancer cells and primary tumors. *The Journal of Clinical Investigation*, 115(1):44–55, January 2005.

[47] Dirk Baumjohann, Andreas Hess, Lubos Budinsky, Kay Brune, Gerold Schuler, and Manfred B. Lutz. In vivo magnetic resonance imaging of dendritic cell migration into the draining lymph nodes of mice. *European Journal of Immunology*, 36(9):2544–2555, 2006. _eprint: https://onlinelibrary.wiley.com/doi/pdf/10.1002/eji.200535742.

[48] Anand Rotte and Madhuri Bhandaru. Challenges of Immunotherapy. In Anand Rotte and Madhuri Bhandaru, editors, *Immunotherapy of Melanoma*, pages 419–434. Springer International Publishing, Cham, 2016.

[49] W. Joost Lesterhuis, John B. A. G. Haanen, and Cornelis J. A. Punt. Cancer immunotherapy–revisited. *Nature Reviews. Drug Discovery*, 10(8):591–600, August 2011.

[50] Katie M. Parkins, Amanda M. Hamilton, Ashley V. Makela, Yuanxin Chen, Paula J. Foster, and John A. Ronald. A multimodality imaging model to track viable breast cancer cells from single arrest to metastasis in the mouse brain. *Scientific Reports (Nature Publisher Group); London*, 6:35889, October 2016. Num Pages: 9 Place: London, United States, London Publisher: Nature Publishing Group.

[51] Katie M. Parkins, Amanda M. Hamilton, Veronica P. Dubois, Suzanne M. Wong, Paula J. Foster, and John A. Ronald. Cellular MRI Reveals Altered Brain Arrest of Genetically Engineered Metastatic Breast Cancer Cells. *Contrast Media & Molecular Imaging*, 2019:6501231, 2019.

[52] Atsushi Tanaka and Shimon Sakaguchi. Regulatory T cells in cancer immunotherapy. *Cell Research*, 27(1):109–118, January 2017. Number: 1 Publisher: Nature Publishing Group.

[53] Asim M. Akhtar, Jurgen E. Schneider, Stephanie J. Chapman, Andrew Jefferson, Janet E. Digby, Kulveer Mankia, Ye Chen, Martina A. McAteer, Kathryn J. Wood, and Robin P. Choudhury. In Vivo Quantification of Vcam-1 Expression in Renal Ischemia Reperfusion Injury Using Non-Invasive Magnetic Resonance Molecular Imaging. *PLOS ONE*, 5(9):e12800, September 2010. Publisher: Public Library of Science.

[54] Gregory A. Dekaban, Jonatan Snir, Bradly Shrum, Sonali de Chickera, Christy Willert, Mia Merrill, Elias A. Said, Rafick-Pierre Sekaly, Paula J. Foster, and Peta J. O'Connell. Semiquantitation of Mouse Dendritic Cell Migration In Vivo Using Cellular MRI. *Journal of Immunotherapy*, 32(3):240–251, April 2009.

[55] Govind B. Chavhan, Paul S. Babyn, Bhavin G. Jankharia, Hai-Ling M. Cheng, and Manohar M. Shroff. Steady-State MR Imaging Sequences: Physics, Classification, and Clinical Applications. *RadioGraphics*, 28(4):1147–1160, July 2008. Publisher: Radiological Society of North America.

[56] Danielle V. Bower, Johannes K. Richter, Hendrik von Tengg-Kobligk, Johannes T. Heverhagen, and Val M. Runge. Gadolinium-Based MRI Contrast Agents Induce Mitochondrial Toxicity and Cell Death in Human Neurons, and Toxicity Increases With Reduced Kinetic Stability of the Agent. *Investigative Radiology*, 54(8):453–463, 2019.

[57] Javier Abello, Tuyen Duong Thanh Nguyen, Ramesh Marasini, Santosh Aryal, and Mark Louis Weiss. Biodistribution of gadolinium- and near infrared-labeled human umbilical cord mesenchymal stromal cell-derived exosomes in tumor bearing mice. *Theranostics*, 9(8):2325–2345, April 2019.

[58] Rohan Dharmakumar, Ioannis Koktzoglou, and Debiao Li. Generating positive contrast from off-resonant spins with steady-state free precession magnetic resonance imaging: theory and proof-of-principle experiments. *Physics in Medicine and Biology*, 51(17):4201–4215, September 2006.

[59] S. Patil, D. Jirák, F. Saudek, M. Hájek, and K. Scheffler. Positive contrast visualization of SPIO-labeled pancreatic islets using echo-dephased steady-state free precession. *European Radiology*, 21(1):214–220, January 2011.

[60] Hannes Dahnke, Wei Liu, Daniel Herzka, Joseph A. Frank, and Tobias Schaeffter. Susceptibility gradient mapping (SGM): A new postprocessing method for positive contrast generation applied to superparamagnetic iron oxide particle (SPIO)-labeled cells. *Magnetic Resonance in Medicine*, 60(3):595–603, 2008. _eprint: https://onlinelibrary.wiley.com/doi/pdf/10.1002/mrm.21478.

[61] Vindegaard N, Muñoz-Briones C, El Ali Hh, Kristensen Lk, Rasmussen Rs, Johansen Ff, and Hasseldam H. T-cells and Macrophages Peak Weeks After Experimental Stroke: Spatial and Temporal Characteristics, October 2017. ISSN: 1440-1789 Issue: 5 Library Catalog: pubmed-ncbi-nlm-nih-gov.ezproxy.library.dal.ca Publisher: Neuropathology Volume: 37.

[62] Corby Fink, Michael Smith, Jeffrey M. Gaudet, Ashley Makela, Paula J. Foster, and Gregory A. Dekaban. Fluorine-19 Cellular MRI Detection of In Vivo Dendritic Cell Migration and Subsequent Induction of Tumor Antigen-Specific Immunotherapeutic Response. *Molecular Imaging and Biology*, 22(3):549–561, June 2020.

[63] Sayuan Liang, Karim Louchami, Bryan Holvoet, Rein Verbeke, Christophe M. Deroose, Bella Manshian, Stefaan J. Soenen, Ine Lentacker, and Uwe Himmelreich. Tri-modal In vivo Imaging of Pancreatic Islets Transplanted Subcutaneously in Mice. *Molecular Imaging and Biology*, 20(6):940–951, 2018.

[64] Dorit Granot, Yoseph Addadi, Vyacheslav Kalchenko, Alon Harmelin, Leoni A. Kunz-Schughart, and Michal Neeman. In vivo imaging of the systemic recruitment of fibroblasts to the angiogenic rim of ovarian carcinoma tumors. *Cancer Research*, 67(19):9180–9189, October 2007.

[65] Kai Li, Dan Ding, Chandrasekharan Prashant, Wei Qin, Chang-Tong Yang, Ben Zhong Tang, and Bin Liu. Gadolinium-Functionalized Aggregation-Induced Emission Dots as Dual-Modality Probes for Cancer Metastasis Study. *Advanced Healthcare Materials*, 2(12):1600–1605, 2013. _eprint: https://onlinelibrary.wiley.com/doi/pdf/10.1002/adhm.201300135.

[66] Zoe O'Brien-Moran, Chris Van Bowen, James Allen Rioux, and Kimberly Dawn Brewer. Cell density quantification with TurboSPI: R2* mapping with compensation for off-resonance fat modulation. *Magnetic Resonance Materials in Physics, Biology and Medicine*, December 2019.

[67] Kimberly D. Brewer, Ryan Spitler, Kayla R. Lee, Andrea C. Chan, Joyce C. Barrozo, Abdul Wakeel, Chandler S. Foote, Steven Machtaler, James Rioux, Juergen K. Willmann, Papia Chakraborty, Bradley W. Rice, Christopher H. Contag, Caleb B. Bell, and Brian K. Rutt. Characterization of Magneto-Endosymbionts as MRI Cell Labeling and Tracking Agents. *Molecular Imaging and Biology*, 20(1):65–73, 2018.

[68] Wei Liu and Joseph A. Frank. Detection and quantification of magnetically labeled cells by cellular MRI. *European Journal of Radiology*, 70(2):258–264, May 2009.

[69] Nikhil Rammohan, Keith W. MacRenaris, Laura K. Moore, Giacomo Parigi, Daniel J. Mastarone, Lisa M. Manus, Laura M. Lilley, Adam T. Preslar, Emily A. Waters, Abigail Filicko, Claudio Luchinat, Dean Ho, and Thomas J. Meade. Nanodiamond-Gadolinium(III) Aggregates for Tracking Cancer Growth In Vivo at High Field. *Nano Letters*, 16(12):7551–7564, 2016.

[70] Dmitriy A. Yablonskiy and E. Mark Haacke. An MRI method for measuring T2 in the presence of static and RF magnetic field Inhomogeneities. *Magnetic Resonance in Medicine*, 37(6):872–876, 1997. _eprint: https://onlinelibrary.wiley.com/doi/pdf/10.1002/mrm.1910370611.

[71] Luning Wang, William M. Potter, and Qun Zhao. In vivo quantification of SPIO nanoparticles for cell labeling based on MR phase gradient images. *Contrast Media & Molecular Imaging*, 10(1):43–50, 2015. _eprint: https://onlinelibrary.wiley.com/doi/pdf/10.1002/cmmi.1601.

[72] Rebecca Kuhlpeter, Hannes Dahnke, Lars Matuszewski, Thorsten Persigehl, Angelika von Wallbrunn, Thomas Allkemper, Walter L. Heindel, Tobias Schaeffter, and Christoph Bremer. R2 and R2* Mapping for Sensing Cell-bound Superparamagnetic Nanoparticles: In Vitro and Murine in Vivo Testing. *Radiology*, 245(2):449–457, November 2007. Publisher: Radiological Society of North America.

[73] Peter Schmitt, Mark A. Griswold, Peter M. Jakob, Markus Kotas, Vikas Gulani, Michael Flentje, and Axel Haase. Inversion recovery TrueFISP: quantification of T(1), T(2), and spin density. *Magnetic Resonance in Medicine*, 51(4):661–667, April 2004.

[74] Philipp Ehses, Nicole Seiberlich, Dan Ma, Felix A. Breuer, Peter M. Jakob, Mark A. Griswold, and Vikas Gulani. IR TrueFISP with a golden-ratio-based radial readout: fast quantification of T1, T2, and proton density. *Magnetic Resonance in Medicine*, 69(1):71–81, January 2013.

[75] J. B. M. Warntjes, O. Dahlqvist, and P. Lundberg. Novel method for rapid, simultaneous T1, T2*, and proton density quantification. *Magnetic Resonance in Medicine*, 57(3):528–537, March 2007.

[76] L.N. Tanenbaum, A.J. Tsiouris, A.N. Johnson, T.P. Naidich, M.C. DeLano, E.R. Melhem, P. Quarterman, S.X. Parameswaran, A. Shankaranarayanan, M. Goyen, and A.S. Field. Synthetic MRI for Clinical Neuroimaging: Results of the Magnetic Resonance Image Compilation (MAGiC) Prospective, Multicenter, Multireader Trial. *American Journal of Neuroradiology*, 38(6):1103–1110, June 2017.

[77] Cheng-Chieh Cheng, Frank Preiswerk, W. Scott Hoge, Tai-Hsin Kuo, and Bruno Madore. Multipathway multi-echo (MPME) imaging: all main MR parameters mapped based on a single 3D scan. *Magnetic Resonance in Medicine*, 81(3):1699–1713, 2019.

[78] Riccardo Metere, Tobias Kober, Harald E. Möller, and Andreas Schäfer. Simultaneous Quantitative MRI Mapping of T1, T2* and Magnetic Susceptibility with Multi-Echo MP2RAGE. *PloS One*, 12(1):e0169265, 2017.

[79] Rahel Heule, Carl Ganter, and Oliver Bieri. Triple echo steady-state (TESS) relaxometry. *Magnetic Resonance in Medicine*, 71(1):230–237, 2014. _eprint: https://onlinelibrary.wiley.com/doi/pdf/10.1002/mrm.24659.

[80] Ulrike Blume, Timothy Lockie, Christian Stehning, Stephen Sinclair, Sergio Uribe, Reza Razavi, and Tobias Schaeffter. Interleaved T1 and T2 relaxation time mapping for cardiac applications. *Journal of Magnetic Resonance Imaging*, 29(2):480–487, 2009. _eprint: https://onlinelibrary.wiley.com/doi/pdf/10.1002/jmri.21652.

[81] Mehmet Akçakaya, Sebastian Weingärtner, Tamer A. Basha, Sébastien Roujol, Steven Bellm, and Reza Nezafat. Joint myocardial T1 and T2 mapping using a combination of saturation recovery and T2 -preparation. *Magnetic Resonance in Medicine*, 76(3):888–896, 2016.

[82] Dan Ma, Vikas Gulani, Nicole Seiberlich, Kecheng Liu, Jeffrey L. Sunshine, Jeffrey L. Duerk, and Mark A. Griswold. Magnetic resonance fingerprinting. *Nature; London*, 495(7440):187–92, March 2013.

[83] Christiaan C. Stolk and Alessandro Sbrizzi. Understanding the combined effect of k-space undersampling and transient states excitation in MR Fingerprinting reconstructions. *IEEE transactions on medical imaging*, February 2019.

[84] null Bo Zhao, Justin P. Haldar, Kawin Setsompop, and Lawrence L. Wald. Optimal experiment design for magnetic resonance fingerprinting. *Conference proceedings: ... Annual International Conference of the IEEE Engineering in Medicine and Biology Society. IEEE Engineering in Medicine and Biology Society. Annual Conference*, 2016:453–456, 2016.

[85] Matthias Weigel. Extended phase graphs: Dephasing, RF pulses, and echoes - pure and simple. *Journal of Magnetic Resonance Imaging*, 41(2):266–295, 2015.

[86] Bhairav Bipin Mehta, Simone Coppo, Debra Frances McGivney, Jesse Ian Hamilton, Yong Chen, Yun Jiang, Dan Ma, Nicole Seiberlich, Vikas Gulani, and Mark Alan Griswold. Magnetic resonance fingerprinting: a technical review. *Magnetic Resonance in Medicine*, 81(1):25–46, 2019. _eprint: https://onlinelibrary.wiley.com/doi/pdf/10.1002/mrm.27403.

[87] Yun Jiang, Dan Ma, Nicole Seiberlich, Vikas Gulani, and Mark A. Griswold. MR fingerprinting using fast imaging with steady state precession (FISP) with spiral readout. *Magnetic Resonance in Medicine*, 74(6):1621–1631, 2015.

[88] Stephen F. Cauley, Kawin Setsompop, Dan Ma, Yun Jiang, Huihui Ye, Elfar Adalsteinsson, Mark A. Griswold, and Lawrence L. Wald. Fast group matching for MR fingerprinting reconstruction. *Magnetic Resonance in Medicine*, 74(2):523–528, August 2015.

[89] Gregor Körzdörfer, Josef Pfeuffer, Thomas Kluge, Matthias Gebhardt, Bernhard Hensel, Craig H. Meyer, and Mathias Nittka. Effect of spiral undersampling patterns on FISP MRF parameter maps. *Magnetic Resonance Imaging*, 62:174–180, October 2019.

[90] Christian E. Anderson, Charlie Y. Wang, Yuning Gu, Rebecca Darrah, Mark A. Griswold, Xin Yu, and Chris A. Flask. Regularly incremented phase encoding - MR fingerprinting (RIPE-MRF) for enhanced motion artifact suppression in preclinical cartesian MR fingerprinting. *Magnetic Resonance in Medicine*, 79(4):2176–2182, 2018.

[91] Dan Ma, Yun Jiang, Yong Chen, Debra McGivney, Bhairav Mehta, Vikas Gulani, and Mark Griswold. Fast 3D magnetic resonance fingerprinting for a whole-brain coverage. *Magnetic Resonance in Medicine*, 79(4):2190–2197, 2018.

[92] Congyu Liao, Berkin Bilgic, Mary Kate Manhard, Bo Zhao, Xiaozhi Cao, Jianhui Zhong, Lawrence L. Wald, and Kawin Setsompop. 3D MR fingerprinting with accelerated stack-of-spirals and hybrid sliding-window and GRAPPA reconstruction. *NeuroImage*, 162:13–22, November 2017.

[93] Yong Chen, Zhenghan Fang, Sheng-Che Hung, Wei-Tang Chang, Dinggang Shen, and Weili Lin. High-resolution 3D MR Fingerprinting using parallel imaging and deep learning. *NeuroImage*, 206:116329, February 2020.

[94] Xiaozhi Cao, Huihui Ye, Congyu Liao, Qing Li, Hongjian He, and Jianhui Zhong. Fast 3D brain MR fingerprinting based on multi-axis spiral projection trajectory. *Magnetic Resonance in Medicine*, 82(1):289–301, 2019.

[95] Yun Jiang. Fast 3D MR Fingerprinting with Pseudorandom Cartesian Sampling. In *Fast 3D MR Fingerprinting with Pseudorandom Cartesian Sampling*, ISMRM 2019, May 2019.

[96] Christian E. Anderson, Shannon B. Donnola, Yun Jiang, Joshua Batesole, Rebecca Darrah, Mitchell L. Drumm, Susann M. Brady-Kalnay, Nicole F. Steinmetz, Xin Yu, Mark A. Griswold, and Chris A. Flask. Dual Contrast - Magnetic Resonance Fingerprinting (DC-MRF): A Platform for Simultaneous Quantification of Multiple MRI Contrast Agents. *Scientific Reports*, 7, August 2017.

[97] Cory R. Wyatt, Travis B. Smith, Manoj K. Sammi, William D. Rooney, and Alexander R. Guimaraes. Multi-parametric T2* magnetic resonance fingerprinting using variable echo times. *NMR in Biomedicine*, 31(9):e3951, 2018.

[98] Taehwa Hong, Dongyeob Han, and Dong-Hyun Kim. Simultaneous estimation of PD, T1, T2, T2*, and deltaB0 using magnetic resonance fingerprinting with background gradient compensation. *Magnetic Resonance in Medicine*, 81(4):2614–2623, 2019.

[99] Charlie Yi Wang, Simone Coppo, Bhairav Bipin Mehta, Nicole Seiberlich, Xin Yu, and Mark Alan Griswold. Magnetic resonance fingerprinting with quadratic RF phase for measurement of T2* simultaneously with df, T1, and T2. *Magnetic Resonance in Medicine*, 81(3):1849–1862, 2019.

[100] P. Zeeman. The Effect of Magnetisation on the Nature of Light Emitted by a Substance. *Nature*, 55(1424):347–347, February 1897. Number: 1424 Publisher: Nature Publishing Group.

[101] Walter Fox Smith. *Waves and Oscillations: A Prelude to Quantum Mechanics*. Oxford University Press, New York, illustrated edition edition, May 2010.

[102] Lawrence P. McIntosh. CPMG. In Gordon C. K. Roberts, editor, *Encyclopedia of Biophysics*, pages 386–386. Springer, Berlin, Heidelberg, 2013.

[103] F. Bloch. Nuclear Induction. *Physical Review*, 70(7-8):460–474, October 1946. Publisher: American Physical Society.

[104] Valérie C. Pierre, Matthew J. Allen, and Peter Caravan. Contrast agents for MRI: 30+ years and where are we going? *Journal of biological inorganic chemistry : JBIC : a publication of the Society of Biological Inorganic Chemistry*, 19(2):127–131, February 2014.

[105] P. Caravan, J. J. Ellison, T. J. McMurry, and R. B. Lauffer. Gadolinium(III) Chelates as MRI Contrast Agents: Structure, Dynamics, and Applications. *Chemical Reviews*, 99(9):2293–2352, September 1999.

[106] Jacques Lux and A. Dean Sherry. Advances in gadolinium-based MRI contrast agent designs for monitoring biological processes in vivo. *Current Opinion in Chemical Biology*, 45:121–130, 2018.

[107] Marie-France Bellin and Aart J. Van Der Molen. Extracellular gadolinium-based contrast media: an overview. *European Journal of Radiology*, 66(2):160–167, May 2008.

[108] Anna Falk Delgado, Danielle Van Westen, Markus Nilsson, Linda Knutsson, Pia C. Sundgren, Elna-Marie Larsson, and Alberto Falk Delgado. Diagnostic value of alternative techniques to gadolinium-based contrast agents in MR neuroimaging—a comprehensive overview. *Insights into Imaging*, 10(1):84, August 2019.

[109] Jeff W. M. Bulte and Dara L. Kraitchman. Iron oxide MR contrast agents for molecular and cellular imaging. *NMR in Biomedicine*, 17(7):484–499, 2004. _eprint: https://onlinelibrary.wiley.com/doi/pdf/10.1002/nbm.924.

[110] Joseph A. Frank, Brad R. Miller, Ali S. Arbab, Holly A. Zywicke, E. Kay Jordan, Bobbi K. Lewis, L. Henry Bryant, and Jeff W. M. Bulte. Clinically Applicable Labeling of Mammalian and Stem Cells by Combining Superparamagnetic Iron Oxides and Transfection Agents. *Radiology*, 228(2):480–487, August 2003. Publisher: Radiological Society of North America.

[111] Michel Modo, Mathias Hoehn, and Jeff W. M. Bulte. Cellular MR Imaging:. *Molecular Imaging*, July 2005. Publisher: SAGE PublicationsSage CA: Los Angeles, CA.

[112] Ray Freeman and H. D. W Hill. Phase and intensity anomalies in fourier transform NMR. *Journal of Magnetic Resonance (1969)*, 4(3):366–383, June 1971.

[113] Thomas Amthor, Mariya Doneva, Peter Koken, Karsten Sommer, Jakob Meineke, and Peter Börnert. Magnetic Resonance Fingerprinting with short relaxation intervals. *Magnetic Resonance Imaging*, 41:22–28, September 2017.

[114] Ken Perlin. An Image Synthesizer. In *Proceedings of the 12th Annual Conference on Computer Graphics and Interactive Techniques*, SIGGRAPH '85, pages 287–296, New York, NY, USA, 1985. ACM.

[115] K. Sommer, T. Amthor, M. Doneva, P. Koken, J. Meineke, and P. Börnert. Towards predicting the encoding capability of MR fingerprinting sequences. *Magnetic Resonance Imaging*, 41:7–14, September 2017.

[116] Lawrence I-Kuei Lin. A Concordance Correlation Coefficient to Evaluate Reproducibility. *Biometrics*, 45(1):255–268, 1989. Publisher: [Wiley, International Biometric Society].

[117] Parvinder Sujlana, Jan Skrok, and Laura M. Fayad. Review of dynamic contrast-enhanced MRI: Technical aspects and applications in the musculoskeletal system. *Journal of Magnetic Resonance Imaging*, 47(4):875–890, 2018.

[118] M. L. Wood and P. A. Hardy. Proton relaxation enhancement. *Journal of magnetic resonance imaging: JMRI*, 3(1):149–156, February 1993.

[119] Marites P. Melancon, Wei Lu, Qian Huang, Prakash Thapa, Dapeng Zhou, Chaan Ng, and Chun Li. Targeted Imaging of Tumor-Associated M2 Macrophages Using a Macromolecular Contrast Agent PG-Gd-NIR813. *Biomaterials*, 31(25):6567–6573, September 2010.

[120] Runze Yang, Susobhan Sarkar, V Wee Yong, and Jeff F Dunn. In Vivo MR Imaging of Tumor-Associated Macrophages: The Next Frontier in Cancer Imaging. *Magnetic Resonance Insights*, 11, April 2018.

[121] Tatiana Abakumova, Maxim Abakumov, Sergey Shein, Pavel Chelushkin, Dmitry Bychkov, Vladimir Mukhin, Gaukhar Yusubalieva, Nadezhda Grinenko, Alexander Kabanov, Natalia Nukolova, and Vladimir Chekhonin. Connexin 43-targeted T1 contrast agent for MRI diagnosis of glioma. *Contrast Media & Molecular Imaging*, 11(1):15–23, February 2016.

[122] James A. Rioux, Kimberly D. Brewer, Steven D. Beyea, and Chris V. Bowen. Quantification of superparamagnetic iron oxide with large dynamic range using TurboSPI. *Journal of Magnetic Resonance (San Diego, Calif.: 1997)*, 216:152–160, March 2012.

[123] Martin Rohrer, Hans Bauer, Jan Mintorovitch, Martin Requardt, and Hanns-Joachim Weinmann. Comparison of Magnetic Properties of MRI Contrast Media Solutions at Different Magnetic Field Strengths:. *Investigative Radiology*, 40(11):715–724, November 2005.

[124] Yuning Gu, Charlie Y. Wang, Christian E. Anderson, Yuchi Liu, He Hu, Mette L. Johansen, Dan Ma, Yun Jiang, Ciro Ramos-Estebanez, Susann Brady-Kalnay, Mark A. Griswold, Chris A. Flask, and Xin Yu. Fast magnetic resonance fingerprinting for dynamic contrast-enhanced studies in mice. *Magnetic Resonance in Medicine*, 80(6):2681–2690, 2018.

[125] Christian E. Anderson, Charlie Y. Wang, Yuning Gu, Rebecca Darrah, Mark A. Griswold, Xin Yu, and Chris A. Flask. Regularly incremented phase encoding - MR fingerprinting (RIPE-MRF) for enhanced motion artifact suppression in preclinical cartesian MR fingerprinting. *Magnetic Resonance in Medicine*, 79(4):2176–2182, 2018.

[126] Ying Gao, Yong Chen, Dan Ma, Yun Jiang, Kelsey A. Herrmann, Jason A. Vincent, Katherine M. Dell, Mitchell L. Drumm, Susann M. Brady-Kalnay, Mark A. Griswold, Chris A. Flask, and Lan Lu. Preclinical MR fingerprinting (MRF) at 7 T: effective quantitative imaging for rodent disease models. *NMR in biomedicine*, 28(3):384–394, March 2015.

[127] Gerben M. van Buul, Gyula Kotek, Piotr A. Wielopolski, Eric Farrell, P. Koen Bos, Harrie Weinans, Anja U. Grohnert, Holger Jahr, Jan A. N. Verhaar, Gabriel P. Krestin, Gerjo J. V. M. van Osch, and Monique R. Bernsen. Clinically translatable cell tracking and quantification by MRI in cartilage repair using superparamagnetic iron oxides. *PloS One*, 6(2):e17001, February 2011.

[128] James A. Rioux, Steven D. Beyea, and Chris V. Bowen. 3D single point imaging with compressed sensing provides high temporal resolution R 2* mapping for in vivo preclinical applications. *Magma (New York, N.Y.)*, 30(1):41–55, February 2017.

[129] Marie-Laurence Tremblay, Zoe O'Brien-Moran, James A. Rioux, Andrea Nuschke, Christa Davis, W. Martin Kast, Genevieve Weir, Marianne Stanford, and Kimberly D. Brewer. Quantitative MRI cell tracking of immune cell recruitment to tumors and draining lymph nodes in response to anti-PD-1 and a DPX-based immunotherapy. *Oncoimmunology*, 9(1):1851539, November 2020.

[130] Joan Estelrich, María Jesús Sánchez-Martín, and Maria Antònia Busquets. Nanoparticles in magnetic resonance imaging: from simple to dual contrast agents. *International Journal of Nanomedicine*, 10:1727–1741, 2015.

[131] Anna Marriott, C. Bowen, J. Rioux, and K. Brewer. Simultaneous quantification of SPIO and gadolinium contrast agents using MR fingerprinting. *Magnetic resonance imaging*, 2021.

[132] Shekhar S. Chandra, Marlon Bran Lorenzana, Xinwen Liu, Siyu Liu, Steffen Bollmann, and Stuart Crozier. Deep learning in magnetic resonance image reconstruction. *Journal of Medical Imaging and Radiation Oncology*, 65(5):564–577, August 2021.

[133] Ouri Cohen, Bo Zhu, and Matthew S. Rosen. MR fingerprinting Deep RecOnstruction NEtwork (DRONE). *Magnetic Resonance in Medicine*, 80(3):885–894, 2018. _eprint: https://onlinelibrary.wiley.com/doi/pdf/10.1002/mrm.27198.

[134] Xiaozhi Cao, Congyu Liao, Zhixing Wang, Ying Chen, Huihui Ye, Hongjian He, and Jianhui Zhong. Robust sliding-window reconstruction for Accelerating the acquisition of MR fingerprinting. *Magnetic Resonance in Medicine*, 78(4):1579–1588, October 2017.

[135] J. A. d'Arcy, D. J. Collins, I. J. Rowland, A. R. Padhani, and M. O. Leach. Applications of sliding window reconstruction with cartesian sampling for dynamic contrast enhanced MRI. *NMR in Biomedicine*, 15(2):174–183, 2002. _eprint: https://analyticalsciencejournals.onlinelibrary.wiley.com/doi/pdf/10.1002/nbm.755.

[136] Zhongbiao Xu, Huihui Ye, Mengye Lyu, Hongjian He, Jianhui Zhong, Yingjie Mei, Zhifeng Chen, Ed X. Wu, Wufan Chen, Qianjin Feng, and Yanqiu Feng. Rigid motion correction for magnetic resonance fingerprinting with sliding-window reconstruction and image registration. *Magnetic Resonance Imaging*, 57:303–312, April 2019.

[137] Debra F. McGivney, Eric Pierre, Dan Ma, Yun Jiang, Haris Saybasili, Vikas Gulani, and Mark A. Griswold. SVD Compression for Magnetic Resonance Fingerprinting in the Time Domain. *IEEE transactions on medical imaging*, 33(12):2311–2322, December 2014.

[138] Jamal Guenoun, Alessandro Ruggiero, Gabriela Doeswijk, Roel C. Janssens, Gerben A. Koning, Gyula Kotek, Gabriel P. Krestin, and Monique R. Bernsen. In vivo quantitative assessment of cell viability of gadolinium or iron-labeled cells using MRI and bioluminescence imaging. *Contrast Media & Molecular Imaging*, 8(2):165–174, 2013. _eprint: https://onlinelibrary.wiley.com/doi/pdf/10.1002/cmmi.1513.

[139] J??rg Pintaske, Petros Martirosian, Hansj??rg Graf, Gunter Erb, Klaus-Peter Lodemann, Claus D. Claussen, and Fritz Schick. Relaxivity of Gadopentetate Dimeglumine (Magnevist), Gadobutrol (Gadovist), and Gadobenate Dimeglumine (MultiHance) in Human Blood Plasma at 0.2, 1.5, and 3 Tesla:. *Investigative Radiology*, 41(3):213–221, March 2006.